UNIVERSITÀ DEGLI STUDI DI PALERMO

DIPARTIMENTO DI ENERGIA, INGEGNERIA DELL'INFORMAZIONE E MODELLI MATEMATICI

DOTTORATO DI RICERCA IN ENERGIA E TECNOLOGIE DELL'INFORMAZIONE

INVERTER-BASED DISTRIBUTED GENERATORS, MODELING AND CONTROL

SETTORE SCIENTIFICO DISCIPLINARE ING-IND/33 – SISTEMI ELETTRICI PER L'ENERGIA

TESI DI
HAKAM SHEHADEH

COORDINATORE DEL DOTTORATO
PROF. MAURIZIO CELLURA

TUTOR
PROF. SALVATORE FAVUZZA

XXX CICLO ANNO ACCADEMICO 2016-2017

Dedicated to…

***My parents**, SULEIMAN SHEHADEH and SAHAR AL-MUHTASEB*

***My wife**, AMAL ABU-SHARKH*

***My kids**, OMAR, SAHAR and JUMAN*

ACKNOWLEDGMENTS

I would like to express my sincere gratitude to my adviser ***Prof. Salvatore Favuzza*** *for his assistance, direction and guidance throughout the years of this work at UNIVERSITÀ DEGLI STUDI DI PALERMO. His valuable and beneficial encouragements was the origin of this work.*

I wish also to express my deep gratitude to ***Prof. Eleonora Riva Sanseverino*** *for her assistance, interests, suggestions, helpful discussions and kind support for this work. I would like also to thank* ***Dr. Valeria Boscaino*** *for her technical and theoretical support.*

Special thanks goes to ***Dr. Jamal Siam*** *and* ***Dr. Muhammad Abu-Khaizaran*** *from Birzeit University, Palestine, for their precious help and support.*

I would like to express my deepest respect to all my family members, my parents and my wife, for their support and love; especially my beloved wife Mrs. Amal Abu-Sharkh for her understanding and sacrifices during my study. Without her, my energy and motivation would be vanished.

Special thanks to the European Union ***Erasmus Mundus***, ***HERMES*** *program for providing me this valuable scholarship to carry out this research and to achieve my goals. Special thank goes to the ERASMUS MUNDUS staff at the University of Palermo, Palermo, Italy; especially Mr.* ***Vincenzo Fumetta***, *Mr.* ***Antonino Serafini***, *Ms.* ***Paola Turchetta*** *and Ms.* ***Margherita Bruno*** *for their help and support during my study and stay in Italy.*

Hakam Shehadeh

December, 2017

TABLE OF CONTENTS

LIST OF FIGURES

LIST OF TABLES

LIST OF ABBREVIATIONS

ABBREVIATIONS	Meaning
AC	Alternating Current
DC	Direct Current
VSI	Voltage Source Inverter
SPWM	Sinusoidal Pulse Width Modulation
DG	Distributed Generator
DER	Distributed Energy Resources
IGBT	Insulated-Gate Bipolar Transistor
PF	Power Factor
PM	Phase Margin
PLL	Phase-Locked Loop
ESG	Electrostatic Synchronous Generator
OPF	Optimal Power Flow
LV	Low Voltage
MV	Medium Voltage
HV	High Voltage

LIST OF SYMBOLS

SYMBOL	Description	UNIT
f_{sw}	The switching frequency	[Hz]
f_{LCF}	The filter cut-off frequency	[Hz]
f_x	The cross-over frequency	[Hz]
L_f	The filter Inductance	[H]
C_f	The filter Capacitance	[F]
r_L	Equivalent series resistance of L_f	[Ω]
ω_{nL}	The no-load angular frequency	[rad/sec]
ω_{ref}	The reference angular frequency	[rad/sec]
V_{nL}	The no-load voltage	[V]
V_{ref}	The reference voltage	[V]
P	Active power	[W]
Q	Reactive Power	[VAR]
S	Apparent Power	[VA]
θ_r	The rotor position angle	[rad]
ω_r	The rotor angular velocity	[rad/sec]
ΔV	The voltage difference across the capacitor plates	[V]
d	The distance between the capacitor plates	[m]
E	The Electric field	[V/m]

Q_d	The *d*-axis stator electric charge	[*C*]
Q_q	The *q*-axis stator electric charge	[*C*]
Q_f	The field electric charge	[*C*]
ε_o	The permittivity of free space	[*F/m*]
A	The cross sectional area of the capacitor plates	[m^2]
v_d	The *d*-axis voltage	[*V*]
v_q	The *q*-axis voltage	[*V*]
V_f	The field voltage	[*V*]
V_{fq}	The *d*-axis field voltage	[*V*]
V_{fq}	The *q*-axis field voltage	[*V*]
i_d	The *d*-axis stator current	[*A*]
i_q	The *q*-axis stator current	[*A*]
I_f	The field current	[*A*]
C_d	The *d*-axis stator capacitance	[*F*]
C_q	The *q*-axis stator capacitance	[*F*]
C_{Md}	The *d*-axis mutual capacitance between the rotor and stator	[*F*]
C_{Mq}	The *q*-axis mutual capacitance between the rotor and stator	[*F*]
T_e	The developed torque	[*N.m*]
r_s	The stator resistance of ESG	[Ω]

r_f	The field resistance of ESG	[Ω]
m_p	The slope of *P vs. f* droop curve	[*Hz/W*]
n_Q	The slope of *Q vs. V* droop curve	[*V/VAR*]

ABSTRACT

In the last few years, electrical power generation is moving from a centralized generation towards distributed generation including on-site Renewable Energy Sources (RESs). In order to overcome RES related issues, as intermittent and fluctuating power, storage elements are included in the on-site generation system. The interaction between distributed generator (DG) units including RES, storage and front-end power converters should be carefully modeled in order to analyze the power system stability. An accurate modeling of DGs is required.

In this thesis, a new modeling approach has been proposed for the inverter-based DGs based on the concept of electrostatic synchronous machines. Detailed mathematical expressions have been provided to model the inverter-based DGs. The equivalence between the proposed model and the conventional small-signal model of inverter-based DGs has been clearly stated based on the duality concept. According to the proposed model, each inverter can be replaced by its equivalent electrostatic machine model and the analysis of the whole microgrid can be performed. A performance comparison between the proposed model and the small-signal model of the VSIs has been carried out. Time domain simulation results showed a perfect matching between the two models and thus, validate the proposed modeling approach. As a result, the analysis of large and small-signal stability of microgrids with multi inverter-based DG can be performed by exploiting the swing equation of virtual electrostatic synchronous generators.

A modified nonlinear droop control method for three-phase VSI DGs working on islanded LV microgrid has been proposed. The nonlinear droop regulation is based on off-line minimum distribution losses Optimal Power Flow with a new plug-and-play

implementation technique, which has been established by constructing a lookup table for the optimized *P vs. f* droop slope of the VSI DG with the highest power capacity.

A comparison between the conventional droop and the proposed nonlinear droop regulation has been carried out. Time domain simulation results showed the advantages of the nonlinear droop regulation method in terms of the distribution line power losses mitigation as well as enhancing the transient response of the system variables.

Keywords: *Distributed Generators, Voltage Source Inverters, Electrostatic Synchronous Machines, Microgrids, Islanded microgrids, nonlinear droop control, minimum losses operation, Optimal Power Flow.*

Chapter 1 INTRODUCTION

1.1 Research background

The demands for reducing the impact of traditional electric utilities on the environment and the need of on-site power generation has opened the doors for exploiting renewable energy sources and Distributed Generators (DGs) in order to meet the growth of electric power demands and emphasize the quality, reliability and stability of power systems. This has introduced the term DGs and Microgrid (MG). According to the U.S. Department of Energy Microgrid Exchange Group, Microgrid is defined as "A group of interconnected loads and distributed energy resources within clearly defined electrical boundaries that acts as a single controllable entity with respect to the grid. A microgrid can connect and disconnect from the grid to enable it to operate in both grid-connected or island mode." [1].

In general, there are many different sources for traditional distributed power generation like coal, oil, fuel cell, natural gas … etc. As mentioned before, the increasing demand for electrical energy will have a negative impact on the environment and will cause depletion of the traditional energy sources. Moreover, the expansion of the electric network to meet the growth of energy demand, especially for those loads which are far away from the main electric utilities is expensive and will increase the transmission and distribution losses. A plausible solution for this problem that is widely used now a days can be obtained by adopting Micrgrids with DERs (such as wind power, solar thermal, solar PV) located near the loads [2]–[5].

Microgrids with DERs have many advantages such as reducing the cost of the electrical energy, increasing the system reliability and power quality, providing local voltage support [1]–[10]. However, implementing DERs and DGs into microgrids have

many technical issues and challenging problems [11]. Some of these technical issues that should be taken into consideration during the design and implementation of DGs in microgrids are synchronization, restoration, protection, operating mode (On-grid and Islanded mode), and power management, quality and control.

In general, Microgrids are flexible electrical distribution networks that can be operated in on-grid or islanded mode including various forms of renewable energy sources. DGs are connected to the grid by means of power electronic switches and are controlled by smart control systems. The basic microgrid architecture is shown in Fig. 1.1 [4], [5]. Microgrid with renewable energy sources appears to be a practical solution to provide electrical power at local level.

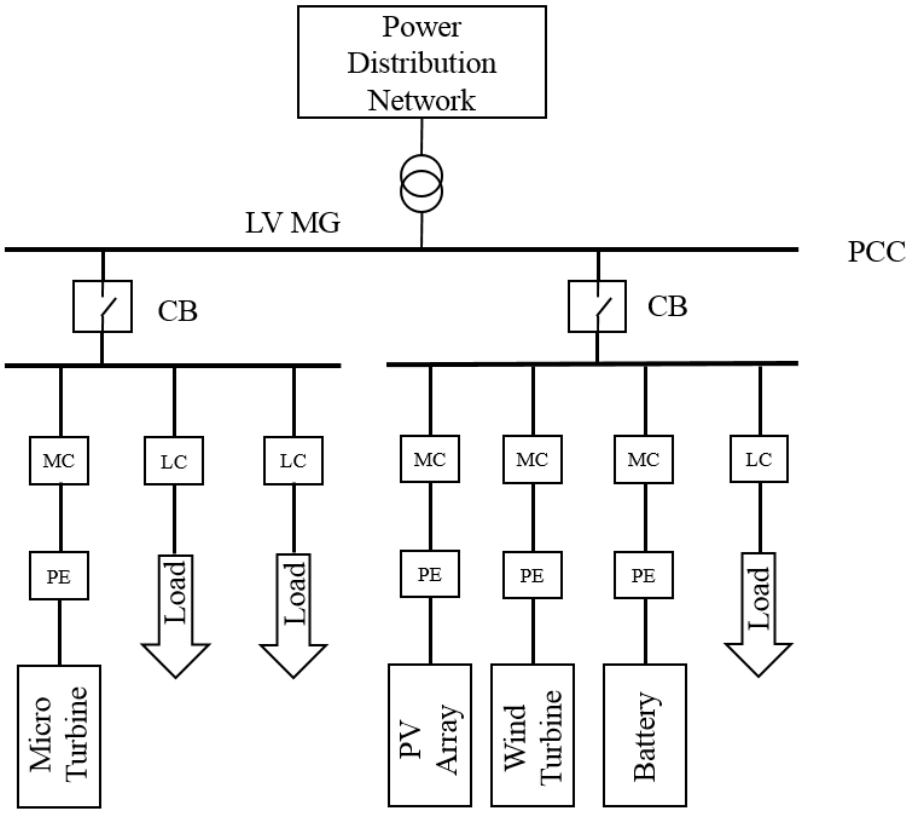

PCC: Point of Common Coupling
MC: Microsource Controller
LC:Load Controller
PE: Power Electronics
CB: Circuit Breaker

Fig. 1.1: Basic scheme of a Microgrid [4], [5].

The DG units which form a microgrid should follow the international regulations in order to meet the requirements and standards. Different classifications and standards for DGs interconnection are listed in [7] and [8]. The performance and control of DGs in a microgrid system depends on the electrical features of the microgrid. The main parameter that should be taken into account during the design and implementation of DGs controllers is the transmission line ratio, *R/X*. The transmission and distribution lines have different resistance and reactance values depending on the operating voltage level. Starting from low-, medium- and high-voltage line, the typical line parameters are listed in Table 1.1 [8]. The droop controlled inverters will act differently according to *R/X* ratio.

Table 1.1: Typical line parameter for different Microgrids [8].

Type of Line	**R (Ω/km)**	**X (Ω/km)**	**R/X**
Low-Voltage	0.642	0.083	7.7
Medium-Voltage	0.161	0.190	0.85
High-Voltage	0.06	0.191	0.31

On the other hand, the increased usage of these kind of distributed generators without a robust control strategy will negatively affect the stability of the microgrid. Thus, a hierarchical control structure ranging from zero to three control levels can be implemented. These control levels have been summarized in [12], [13] and are listed as follow:

- **Level 0** (Inner control loops): The inner control loops works on the regulation of the output voltage and current of each module to maintain the stability of system.
- **Level 1** (Primary control): The most popular control method used in this level is the Droop Control and it is acting at the scale of milliseconds. The aim of droop control is tuning the output voltage and frequency of the inverter while operating in on-grid or islanded mode in microgrids, this will allow DGs to share average

and reactive power demanded by the load without the need for a complex communication system between multi-inverters microgrid systems.

- **Level 2** (Secondary control): This level is implemented to ensure that the electrical parameters of DGs in MGs are within the boundaries and acting at the scale of seconds.
- **Level 3** (Tertiary control): This level concerns about the coordination of microgrids in on-grid operating mode and controls the power flow between the MG and the grid network. This level is acting on the scale of tens of minutes or hours.

The unpredictability and fluctuation of DERs is one of the challenging problems appears in microgrids and when the microgrid is operated in islanded mode, the voltage and frequency became the main electrical parameters to be controlled in order to achieve an optimal power sharing between the DGs [14]–[16]. Such power sharing could be carried out at different regulation levels, starting from the tertiary control level to the secondary and primary control levels (the latter is also called droop regulation).

1.2 Literature Review

Nowadays, there is an increased use of Inverter-Based DGs. This work focuses on the modeling of inverter-based DGs and their control techniques. The main purpose of modeling the inverter-based DGs operating in a microgrid is studying the performance of this kid of DGs in terms of enhancing the transient stability and keeping the voltage and frequency variation within the boundary limits.

The frequency and voltage stability is defined as the ability to maintain these quantities at acceptable range after an occurrence of disturbance [17]–[21]. In other words; the frequency and voltage should remain bounded by a percentage of nominal value. The

challenge question is: how fast the system will respond to this sudden change of frequency and voltage and keep them within the nominal values?

Moreover; it should be noticed that if the Microgrid characteristics is changed, then the dynamics of the system will change accordingly. Most of the researches in the field of microgrid dynamics, stability and control are based on different case studies with different characteristics, scenarios, assumptions and simplifications.

Recently, lots of research efforts are being exerted in modeling the inverter-based DGs in order to analyze their dynamics and their effect on the power grid or microgrids. The goal of all these different models is to investigate the stability of the power systems.

In [22], a small signal model of multiple inverters has been established in order to determine the small-signal stability and predicting the dynamic response of the microgrid. The model is based on nonlinear equations and then linearized around a steady state operating points. The average value modeling technique is used in [23], this model of the voltage source inverter (VSI) consists of three dependent-voltage sources for each phase and they are being controlled by the modulation index. The aim of this modeling approach is covering the control behavior of the inverters to be used in protection studies. Different small-signal modeling approaches of inverters, filters, Phase-locked loop, line parameters are founded in [24]–[29].

On the other hand, in [30]–[35], a control scheme has been developed based on synchronous generator theory in order to force the inverter to operate as a synchronous generator (Synchronverters). This has the advantage of covering the dynamics of the inverter-based DGs and thus investigate the stability of the power system by using the same methodology and theory of the traditional synchronous generators. The key point of the approach is that the controller of the VSI DG should be modelled according to the SG theory so yet it does not include an equivalent model of the VSI itself.

A Virtual Synchronous Generator (VSG) control is an alternative approach to study the stability of inverter-based DGs by forcing the inverter to behave like a synchronous generator [36]–[42]. The inverter is properly controlled to mimic a synchronous generator, thus supporting the power system stability. This can be achieved by using the consolidated theory and algorithms already implemented for synchronous generators to analyze the power system stability. The swing equation of conventional synchronous generators is exploited to be used in VSG by introducing a virtual inertia from energy storage.

In [36], an adaptive inertia is introduced in a VSG control scheme to improve dynamic performances in terms of enhancing the frequency tracking and damping frequency oscillations. In [37] a damping oscillation scheme based on VSG is implemented for distributed generators. Differences between the VSG and the Droop control schemes are analyzed in [42]. Small signal models under both control schemes are developed and compared to investigate effects on the stability analysis and on the dynamic response under load disturbances.

The main difference between the VSG and Synchronverters is that the VSG depends on tracking the voltage and current of the grid at the PCC and the swing equation of traditional synchronous generators is used in VSG by introducing a virtual inertia to the inverter [31].

A time-varying transformer concept as an equivalent model of power inverters is found in [43]. The model consists of time-varying transformers, voltage and current sources, inductors, capacitors and resistors. The problem is that this modeling approach is complicated to be used in stability analysis or even in the analysis of power flow of a microgrid.

In [44], [45], an equivalent model of an inverter-based DG has been established based on the Electrostatic Synchronous Generator concept. This model concerns with the

dynamics of the dc link and the disturbance of the RESs. A sharp separation between the DC and AC side of the DG is achieved thus simplifying the analysis of the interaction between DGs. The model parameters depend on the value of the modulation index which is preset assuming a steady state operation of the inverter. In this way, the inverter model will operate as plug-and-play system. The advantage of this modeling approach is the possibility of studying the small and large signal stability of microgrids composed of inverter-based DGs by exploiting the swing equation of electrostatic synchronous generators as done in [46].

The main concern about the equivalent model of three-phase VSI based on electrostatic synchronous machine concept derived in [44], [45] is that the duality exists between electrostatic and electromagnetic machines as stated in the field theory. Thus, the equivalent model of VSI should be reconstructed based on the duality concept. The mutual capacitance between the virtual rotor and stator circuits in the model derived in [44], [45] has been modeled in series and hence the separation between the field voltage and the stator voltage is impossible.

Droop control method is the most popular method that is used to ensure exact power sharing and stability of voltage and frequency in microgrids. In the literature, *linear* (conventional), *nonlinear* and *dynamic* droop control methods have been studied and analyzed. Recent studies about droop control of inverter-based DGs in microgrid systems focused on improving the stability of microgrids [47]–[51].

A scheme for controlling parallel connected inverters based on linear droop control in a stand-alone AC supply system is presented in [50], the system doesn't need communication of control signals between the inverters since the variables were measured locally.

In [51], the influence of a sudden load change on the voltage and frequency oscillations has been studied. A direct current vector control with the conventional droop control has been implemented in order to improve the voltage and frequency stability.

Conventional droop control is considered as a primary controller with main functionality of ensuring power sharing among DGs by regulating the voltage and frequency of each DGs in which are called grid forming units [52]–[60].

In [53], a new control method of parallel inverters operating in an islanded grid or connected to an infinite power bus is described. Based on the linear droop regulation, *R/X* ratio has been considered during the design of the droop regulation. Frequency and voltage control are achieved without any communication between inverters.

In [52], the fluctuation of RES has been considered during the design of the droop control. As the output power of RES varies; output powers of the inverters remain balanced. Thus, a power offset has been added to the active power of the DGs as a compensating technique without the need of communication means between DGs.

While conventional droop control is simply constructed by constant droop coefficients, in [61], [62], a nonlinear droop control where the frequency and voltage droop relations are changed as a function of the optimized output power for power sharing among DGs is fully described. This provides an indirect optimization among different DGs in the network and finds a solution to minimize operating costs. The nonlinear droop control is also mentioned in the reference materials [63]–[66].

It is possible to use the no-load voltage and no-load frequency as dynamic signals to regulate the output power of each DG unit, this method is considered as an expansion of the linear droop control and it is well known as Dynamic droop control. In [67], [68], an improved droop control method with automatic master to correct the voltage regulation is presented.

The dynamic droop control is also used in [69] to regulate the active power flow to reduce the fuel cost of DGs. The proposed method uses a communication infrastructure between DGs in order to achieve the objectives of the optimization process. A cost optimization based on a dynamic power sharing method is mentioned in [70], where a linear unit commitment strategy based on a frequency droop scheme is solved to determine the amount of power that each generator should put into the power bus. However, results are just concentrated on the power sharing issue, without considering frequency conditions.

1.3 Thesis motivation and objectives

The main objective of this thesis is devoted to solve some problems regarding the modeling of Inverter-Based Distributed Generators using the concept of Electrostatic Synchronous Machines. Such a model is helpful in stability analysis of microgrids. The thesis focuses in Islanded operation of microgrids with inverter-based DGs. A simplified inner control loop architecture is used for the inverters by adopting voltage control loop only.

The need for minimizing the distribution losses in LV microgrids is a significant issue to meet the increasing power demand. The application of nonlinear Droop control of DGs in terms of minimizing the power losses in distribution lines in LV islanded microgrid has been studied.

More specifically, the main objective of this thesis can be summarized as follow:

- Design a three-phase VSI with LC low pass filter to be used as an interface between a storage system and the microgrid.
- Developing the *dq* model of the three-phase VSI with the LC filter and deriving the voltage transfer function for balanced linear loads.

- Designing a voltage controller composed of a phase-lead compensator with large phase margin to regulate the three-phase VSI output voltage and frequency. The design process depends on the *dq* components of the measured voltage obtained by transforming the *abc* quantities into *dq* reference frame using original Park Transformation.
- Implementing a test microgrid and applying the designed voltage controller to the three-phase VSI working on that microgrid under different loading conditions in MATLAB/Simulink environment.
- Explaining the basic construction of the proposed virtual three-phase Electrostatic Synchronous Generator with single and double field circuit. This type of generators is used as a foundation for the modeling approach of three-phase VSIs.
- Explaining the basic principle of operation of electrostatic synchronous generators with the help of electrostatic theory in order to derive the self- and mutual capacitance which form the core of the modeling process.
- Solving the problems founded in the literature regarding the modeling of three-phase VSI DGs using the concept of electrostatic synchronous generators by developing the *dq* model of the proposed generator and exploring the equivalence between it and the small-signal model of the three-phase VSI by exploiting the concept of duality.
- Developing a test system in MATLAB/Simulink environment to verify the proposed modeling approach and highlighting the importance of the proposed model in the field of studying the stability of microgrids.

- Designing conventional droop control loops as a primary regulation method for parallel operation of three-phase VSI DGs working on the same microgrid and without using any communication means between the DG units.
- Proposing a modified primary regulation technique based on nonlinear droop control for three-phase VSI DGs by employing off-line minimum distribution losses Optimal Power Flow with a new plug-and-play implementation technique.
- Applying the conventional and the proposed nonlinear droop regulation on LV islanded test microgrid with two three-phase VSI DGs and comparing the time domain results between the two methods in MATLAB/Simulink environment.

1.4 Thesis Outline

This thesis consists of five chapters organized as follow:

- ***Chapter 1****: Introduction*

  This chapter describes the research background, literature review, motivation, objectives and the structure of this thesis.

- ***Chapter 2****: Design and control of Three-phase Voltage Source Inverter*

  This chapter contains the design of three-phase VSI with A 2nd order LC low pass filter to be used as an interface between storage system and local loads and operating in on-grid and islanded mode. The dq model of the inverter has been derived in order to design the voltage controller. The voltage controller is a phase-lead compensator with three stages. The performance of the VSI under different loading conditions and with different operating mode has been verified using MATLAB/Simulink.

- ***Chapter 3****: Electrostatic Synchronous Machines concept*

  In this chapter introduces the fundamental of Electrostatic machines. A modified mathematical model of the three-phase VSI using the concept of three-phase electrostatic synchronous generator (ESG) is developed. The construction and operation of the three-phase ESG is described in detail. The electrostatic generator's phase coordinate model with self and mutual time-varying capacitance that depends on the rotor position are explained and derived. The ESG *dq* model is derived and the equivalence between the proposed mathematical model and the *dq* model of the VSI is discussed. Time-domain performance comparison between the proposed mathematical model and the *dq* model of the inverter has been verified in MATLAB/Simulink environment.

- ***Chapter 4****: Nonlinear droop Control of VSI DGs in LV Islanded Microgrids*

  This chapter focuses on the parallel operation of DGs in LV islanded microgrids. An improved non-linear primary regulation method with a new implementation technique is proposed for Inverter-Based distributed generators. The new primary regulation is driven by minimum losses Optimal Power Flow (OPF) for microgrids. A microgrid system is constructed as a case study and a time-domain simulation is carried out under different scenarios to verify the effectiveness of the proposed implementation technique.

- ***Chapter 5****: Conclusions and future work*

  This chapter provides a summary of the achievements of this thesis and gives some future recommendations for possible extension to this research.

Chapter 2 Design and control of Three-phase Voltage Source Inverter

The increasing demands of electrical energy, the spread of renewable energy sources and with the improvements and reliability of power electronic devises opened the door for VSIs to be widely used as DGs. In this chapter, A 20 kVA, 220/380 V, 50 Hz three-phase VSI has been designed to be used as an interface between storage system and local loads or to be connected to the electric grid. A sinusoidal Pulse-Width Modulation (SPWM) has been used with a triangular carrier signal of 6 kHz. A 2nd order LC low pass filter is then used in order to minimize the switching harmonics. The performance of the VSI has been verified using MATLAB/Simulink.

2.1 Three-phase VSI with output LC low pass filter

DC to AC converters, or simply called Inverters, and with the huge developments in Power Electronics and semiconductor devices in line with different and improved converter techniques made the inverters to play the main role in the distributed power generation systems. In general, CD/ AC converters can be categorized into two particular categories; Current Source Inverters (CSI) and Voltage Source Inverters (VSI). CSIs have an independent control of the output current and its output voltage depends on the load connected to this CSI. On the other hand, VSIs have an independent control of the output voltage [71].

In this thesis, where a microgrid system is under study, the converter used is the VSI as the output voltage of this kind of converters have to be controlled independently. The first case study to be analyzed and designed is the modeling of VSI with LC filter supplying a local three-phase load. A voltage controller has been designed in order to

regulate the output voltage of the inverter under balanced linear loads. Fig. 2.1 shows the schematic of a three phase VSI with LC filter supplying a local load.

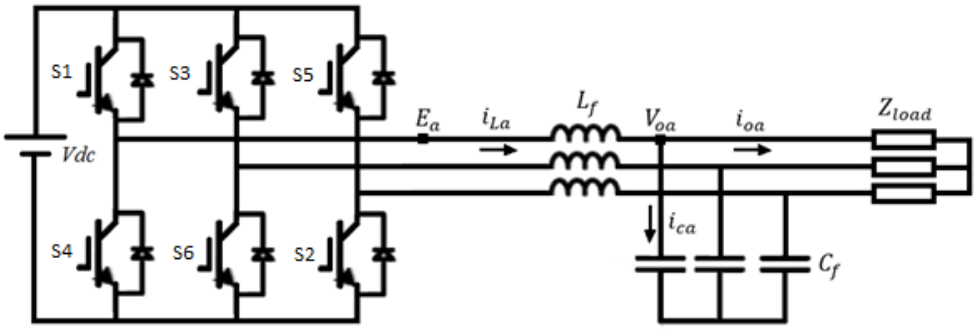

Fig. 2.1: Three-phase VSI with LC filter and linear balanced three-phase load.

2.1.1 Sinusoidal Pulse Width Modulation SPWM

The gating signals generated by SPWM are used to switch on and off the IGBTs, shown in Fig. 2.1. There are three sinusoidal reference signals V_{ra}, V_{rb} and V_{rc} shifted by 120^o from each other and with the same amplitude A_r and frequency f_r. The amplitude and the frequency of the three sinusoidal reference signals are variable and being compared with a triangular wave signal V_t which has a fixed amplitude and frequency, A_t and f_t, respectively. This will provide the gating signals for (S1, S4), (S3, S6) and (S5, S2), respectively as shown in Fig. 2.2.

The switching frequency (f_{sw}) of the inverter is chosen to be 6 kHz, the amplitude of the triangular wave signal A_t is 1 volt, so, the modulation index should be less than or equal to 1.

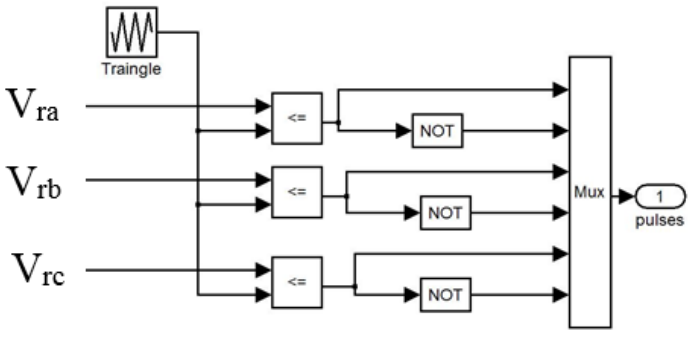

Fig. 2.2: Gating circuit of SPWM VSI.

2.1.2 The 2nd order low pass filter

Integrating VSIs in DGs without considering the harmonics injected to the grid will create severe problems in the microgrid systems. The solution to this problem is connecting a low pass filter between the VSI and the microgrid. There are different topologies for the low pass filters which are commonly used in distributed generation systems, namely, *L*-, *LC*- and *LCL*-filters [72]–[75].

The filter topology adopted in this thesis is a 2nd order LC low pass filter. As the selected switching frequency is 6 kHz; the cut-off frequency (f_{LCF}) of the LC filter is selected to be 100 Hz in such a way that the filter will be able to attenuate the low order harmonics of the output voltage of the inverter. This means that the capacitance value should be increased while decreasing the inductance value. On the other hand, increasing the switching frequency will decrease the inverter's efficiency. A trade-off design should be solved between the overall losses, cost and size [73], [75].

The values of L_f and C_f where set according to (2.1) [75].

$$f_{LCF} = \frac{1}{2\pi\sqrt{L_f C_f}} \tag{2.1}$$

If C_f = 1500 μF and f_{LCF} is 100Hz, then according to (2.1) the value of L_f is 1.6 mH. Here the inductor has an equivalent series resistance r_L of 0.5 ohm and it is much greater than the equivalent series resistance of the capacitor r_C. The latter will be ignored for the sake of simplicity.

2.1.3 Selection of the DC bus voltage magnitude

In case of using sinusoidal PWM controlled inverters, the relationship between the DC bus voltage and the output line voltage of the VSI in the linear region is [71]:

$$V_{DC} = \frac{2\sqrt{2}}{\sqrt{3}} \frac{V_{Line,rms}}{m_a} \tag{2.2}$$

The line to line voltage of the VSI is assumed to vary within ± 10% of its nominal value and the modulation index (m_a) is smaller than or equal to 1. According to this; the DC bus voltage can be calculated using (2.2).

The output line voltage of the VSI is 380 V, and in order to keep the SPWM in the liner region, the maximum output line voltage of the inverter which is equal to 418 V should be obtained when the modulation index m_a equals 0.8 and thus the DC bus voltage is equal to 853.76 V. One can chose m_a = 0.9 at the maximum line voltage and consequently the DC bus voltage will equal to 800 V. In this work, a 900V DC bus voltage is selected. The DC bus (or storage system) has been considered as a constant DC voltage source in this thesis.

2.2 Three phase VSI modeling in *dq0* coordinates for balanced linear loads

The power system needs to be transformed from *abc* coordinates into *dq0* coordinates in order to deal with DC components. These DC components will be used as inputs to the voltage controller.

Considering balanced linear loads, and from Fig. 2.1, writing the KVL equation:

$$\begin{aligned} -E_a + L_f \frac{d}{dt} i_{La} + r_L i_{La} + V_{oa} = 0 \\ -E_b + L_f \frac{d}{dt} i_{Lb} + r_L i_{Lb} + V_{ob} = 0 \\ -E_c + L_f \frac{d}{dt} i_{Lc} + r_L i_{Lc} + V_{oc} = 0 \end{aligned} \tag{2.3}$$

Rearranging the above equation and writing it in matrix form;

$$L_f \frac{d}{dt} \begin{bmatrix} i_{La} \\ i_{Lb} \\ i_{Lc} \end{bmatrix} = \begin{bmatrix} E_a \\ E_b \\ E_c \end{bmatrix} - r_L \begin{bmatrix} i_{La} \\ i_{Lb} \\ i_{Lc} \end{bmatrix} - \begin{bmatrix} V_{oa} \\ V_{ob} \\ V_{oc} \end{bmatrix} \tag{2.4}$$

dividing by L_f, then:

$$\frac{d}{dt} \begin{bmatrix} i_{La} \\ i_{Lb} \\ i_{Lc} \end{bmatrix} = \frac{1}{L_f} \begin{bmatrix} E_a \\ E_b \\ E_c \end{bmatrix} - \frac{r_L}{L_f} \begin{bmatrix} i_{La} \\ i_{Lb} \\ i_{Lc} \end{bmatrix} - \frac{1}{L_f} \begin{bmatrix} V_{oa} \\ V_{ob} \\ V_{oc} \end{bmatrix} \tag{2.5}$$

Now, writing the KCL equations and taking into account that r_C has been neglected:

$$\begin{aligned} i_{La} &= i_{ca} + i_{oa} \\ i_{Lb} &= i_{cb} + i_{ob} \\ i_{Lc} &= i_{cc} + i_{oc} \end{aligned} \tag{2.6}$$

rewriting (2.6) in terms of the output voltage of the inverter:

$$\begin{bmatrix} i_{La} \\ i_{Lb} \\ i_{Lc} \end{bmatrix} = C_f \frac{d}{dt} \begin{bmatrix} V_{oa} \\ V_{ob} \\ V_{oc} \end{bmatrix} + \frac{1}{Z_{load}} \begin{bmatrix} V_{oa} \\ V_{ob} \\ V_{oc} \end{bmatrix} \tag{2.7}$$

rearranging (2.7);

$$\frac{d}{dt} \begin{bmatrix} V_{oa} \\ V_{ob} \\ V_{oc} \end{bmatrix} = \frac{1}{C_f} \begin{bmatrix} i_{La} \\ i_{Lb} \\ i_{Lc} \end{bmatrix} - \frac{1}{C_f Z_{load}} \begin{bmatrix} V_{oa} \\ V_{ob} \\ V_{oc} \end{bmatrix} \tag{2.8}$$

In order to obtain the *dq* equivalent circuit of the VSI, *abc* to *dq* transformation is applied by using the original Parks Transformation matrix. The original Parks transformation in which the *q*-axis is leading the *d*-axis by 90° is used, as shown in Fig. 2.3.

$$X_{dq0} = \frac{2}{3} \begin{bmatrix} cos(\omega t) & cos\left(\omega t - \frac{2\pi}{3}\right) & cos\left(\omega t + \frac{2\pi}{3}\right) \\ -sin(\omega t) & -sin\left(\omega t - \frac{2\pi}{3}\right) & -sin\left(\omega t + \frac{2\pi}{3}\right) \\ 1/2 & 1/2 & 1/2 \end{bmatrix} X_{abc} \tag{2.9}$$

Since a balanced three-phase system is considered, the zero-axis component is null. By applying *abc* to *dq* reference frame transformation (2.9) on (2.5) and (2.8), (2.10) and (2.11) are obtained.

$$\begin{bmatrix} E_d \\ E_q \end{bmatrix} = \begin{bmatrix} V_{od} \\ V_{oq} \end{bmatrix} + r_L \begin{bmatrix} I_{Ld} \\ I_{Lq} \end{bmatrix} + L_f \frac{d}{dt} \begin{bmatrix} I_{Ld} \\ I_{Lq} \end{bmatrix} + \begin{bmatrix} -\omega L_f I_{Lq} \\ \omega L_f I_{Ld} \end{bmatrix} \tag{2.10}$$

$$\begin{bmatrix} I_{Ld} \\ I_{Lq} \end{bmatrix} = C_f \frac{d}{dt} \begin{bmatrix} V_{od} \\ V_{oq} \end{bmatrix} + \frac{1}{Z_{load}} \begin{bmatrix} V_{od} \\ V_{oq} \end{bmatrix} + \begin{bmatrix} -\omega C_f V_{oq} \\ \omega C_f V_{od} \end{bmatrix} \tag{2.11}$$

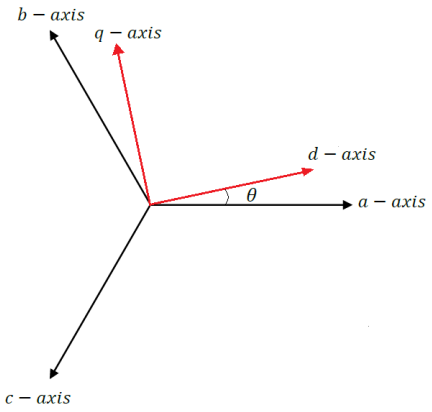

Fig. 2.3 Relationship between the *dq* and *abc* quantities.

Now, the *dq* equivalent circuit of a three phase VSI is shown in Fig. 2.4.

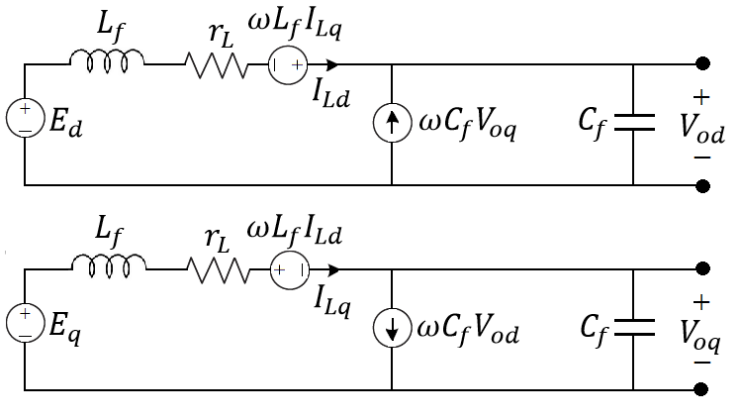

Fig. 2.4: The *dq* Equivalent circuit of three phase VSI with LC filter.

2.3 The voltage controller design

The bode diagram of the transfer function V_{od}/E_d and V_{oq}/E_q have been obtained in order to design the voltage controller. Depending on equations (2.10) and (2.11) and adding a load Z_L between the terminals V_{od} and V_{oq}, the equations of the system in *s*-domain are as follow:

$$\begin{aligned} sI_{Ld}(s) &= 1/L_f\left[\left(E_d(s) - V_{od}(s)\right) - r_L I_{Ld}(s) + \omega L_f I_{Lq}(s)\right] \\ sI_{Lq}(s) &= 1/L_f\left[\left(E_q(s) - V_{oq}(s)\right) - r_L I_{Lq}(s) - \omega L_f I_{Ld}(s)\right] \end{aligned} \tag{2.12}$$

and

$$\begin{aligned} sV_{od}(s) &= 1/C_f\left[I_{Ld}(s) - \frac{1}{Z_L}V_{od}(s) + \omega C_f V_{oq}(s)\right] \\ sV_{oq}(s) &= 1/C_f\left[I_{Lq}(s) - \frac{1}{Z_L}V_{oq}(s) + \omega C_f V_{od}(s)\right] \end{aligned} \tag{2.13}$$

The general block diagram in s-domain is obtained as shown in Fig. 2.5.

Now, if the coupling between the *d*- and *q*-axis has been neglected, the general block diagram can be reduced into a simple one, while the open-loop transfer function is:

$$G_e(s) = \frac{1/L_f C_f}{\left(s + \frac{r_L}{L_f}\right)\left(s + \frac{1}{Z_L C_f}\right)} \tag{2.14}$$

which is equivalent for both the *d*- and *q*-axis.

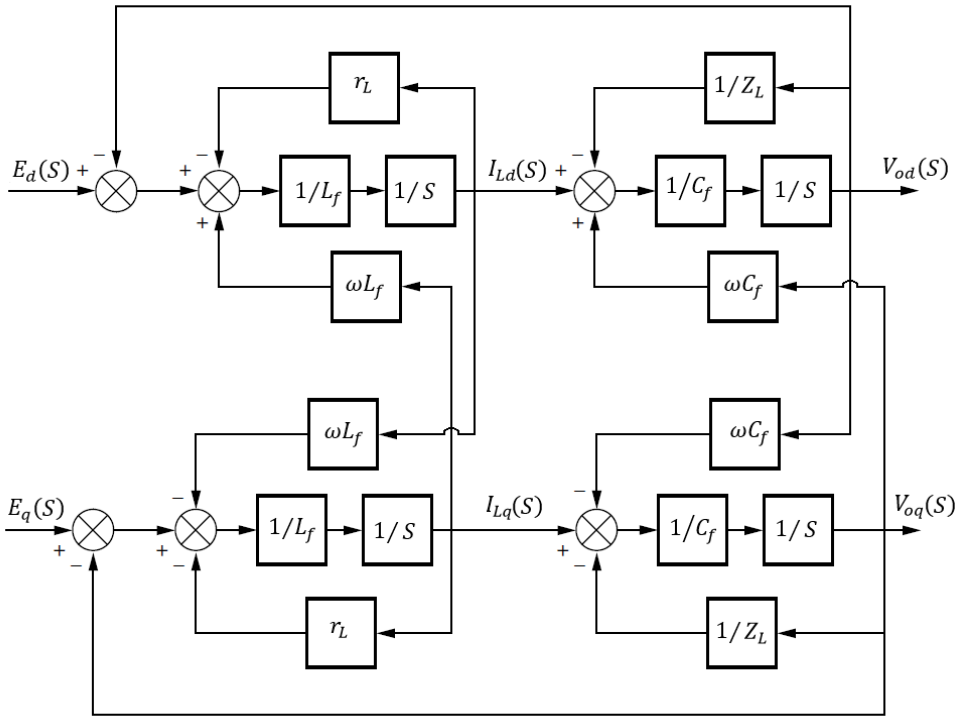

Fig. 2.5: s-Domain Block Diagram of the three-phase VSI

The reduced block diagram is shown in Fig. 2.6. In order to compensate the assumption of neglecting the coupling between the *d*- and *q*-axis, a phase-lead compensator of three stages with large phase margin has been designed.

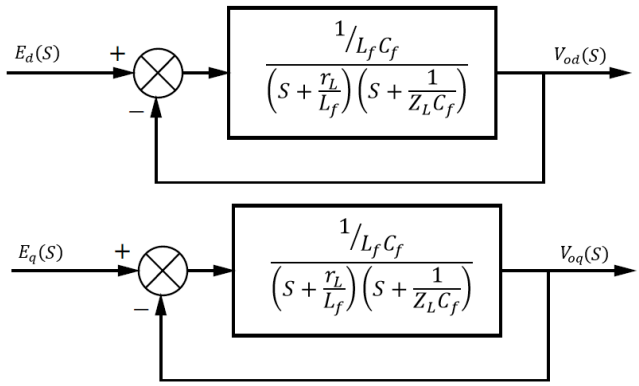

Fig. 2.6: Reduced block diagram of the three-phase VSI.

Assuming a unity power factor load, or resistive load, we can see the response of the system $V_{od}(s)/E_d(s)$ and $V_{oq}(s)/E_q(s)$ under different loading conditions. The loads has been chosen to be a very light loads, which corresponds to 10 W output power of the three-

phase VSI, a 50% loading (10 kW) and full load condition (20 kW). Table 2.1 shows the values of different loading conditions of the three-phase VSI.

Table 2.1: Loading conditions of the VSI

VSI output Power (%)	Load (Ω)
0.05%	14520
50%	14.52
100%	7.26

The bode diagram of the three loading conditions are shown in Fig. 2.7. It is clear from Fig. 2.7 that under light load the damping of the system is very large which will have oscillatory and very poor transient response. The voltage controller should be designed according the worst loading condition (light load) in order to get fast and good transient response and zero steady-state error.

Looking at the bode diagram of the light load condition in Fig. 2.8, a new cross-over frequency (f_x) will be selected to be 300 Hz, or 1885 rad/sec as shown in Fig. 2.8. At this frequency, a controller of type phase-lead compensator will be designed such that the new minimum phase margin (PM) has to be 60°. The phase at the new cross-over frequency is -169°, which means that the phase margin of the uncompensated system at f_x is 11°.

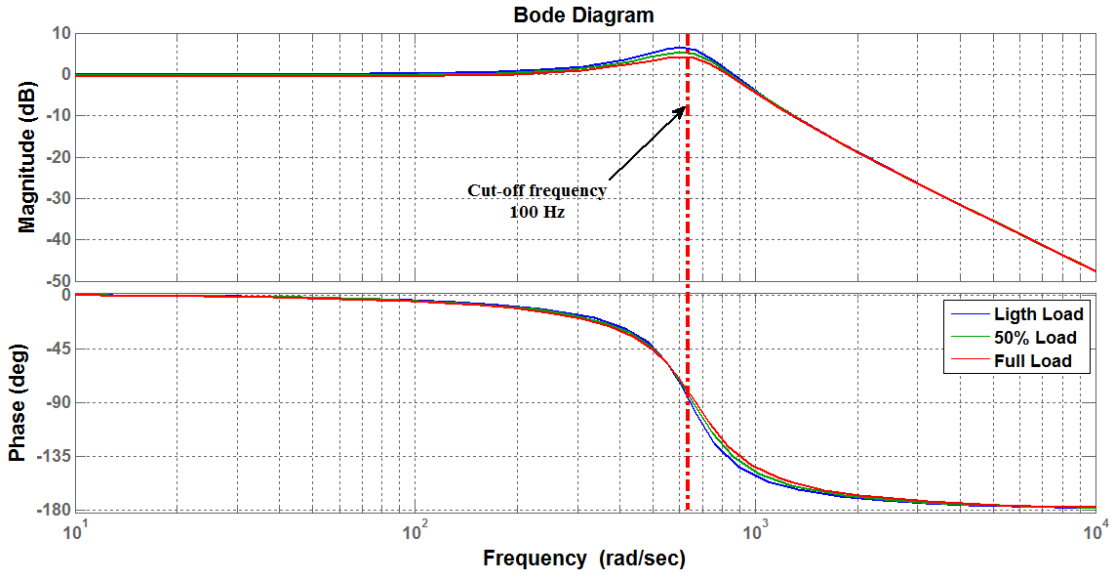

Fig. 2.7: Bode diagram of the closed-loop transfer function with different loading conditions

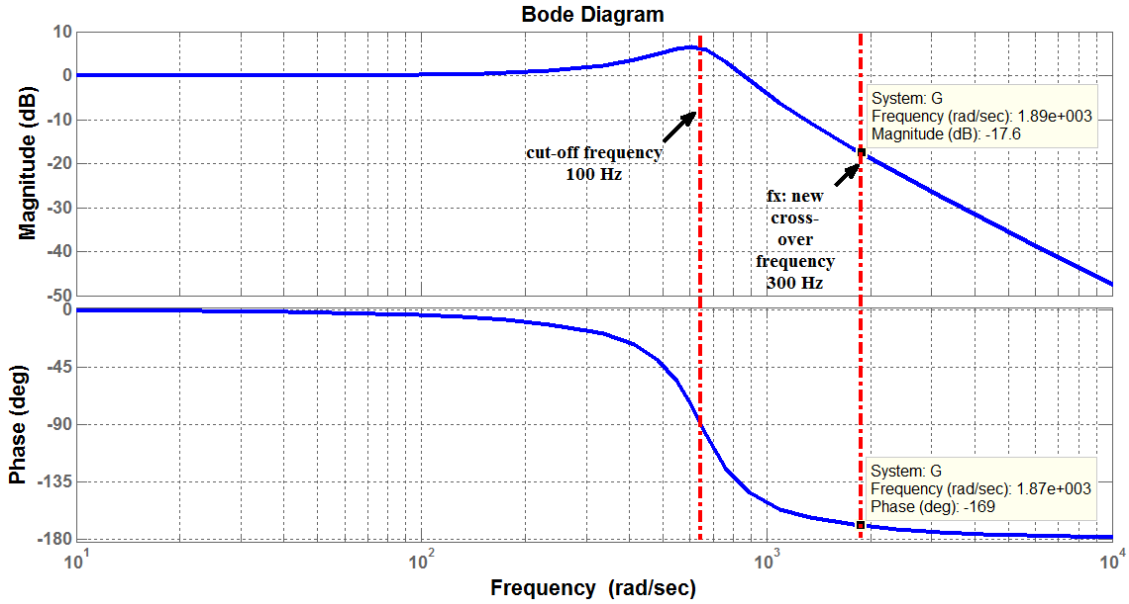

Fig. 2.8: Bode plot of the system under light load condition.

Before designing the phase-lead compensator, the system type should be increased because the system has no pole at the origin (Type 0) as seen in (2.15) which is the closed-loop transfer functions $V_{od}(s)/E_d(s)$ and $V_{oq}(s)/E_q(s)$, namely $G_e(s)$:

$$G_e(s) = \frac{416666.67\ (s + 312.5)\ (s + 0.04591)}{(s + 312.5)\ (s + 0.04591)\ (s^2\ +\ 312.5s\ +\ 4.167 * 10^5)} \qquad (2.15)$$

In order to increase the system type, an integrator ($1/s$) will be added to the phase-lead compensator and thus the steady-state error will be zero for a unit step input. The phase-lead compensator will have three stages and the final transfer function of the voltage controller is as follow:

$$G_C(s) = \left(\frac{K}{s}\right)\left(\frac{s/Z_C + 1}{s/P_C + 1}\right)^3 \qquad (2.16)$$

where K=1025, Z_C=794.6 and P_C=5034.2

Under light load condition, the bode diagram of the open-loop system $G_e(s)*G_c(s)$ is shown in Fig. 2.9. It is clear form this figure that under the new chosen cross-over frequency, the phase margin has been increased to 60.1° such that making the system dynamic less oscillatory. Moreover, under full-load, the system response keeps the phase margin as required as shown in Fig. 2.10. This means that the response speed under

different loading conditions are the same, meaning that the voltage controller has been well designed.

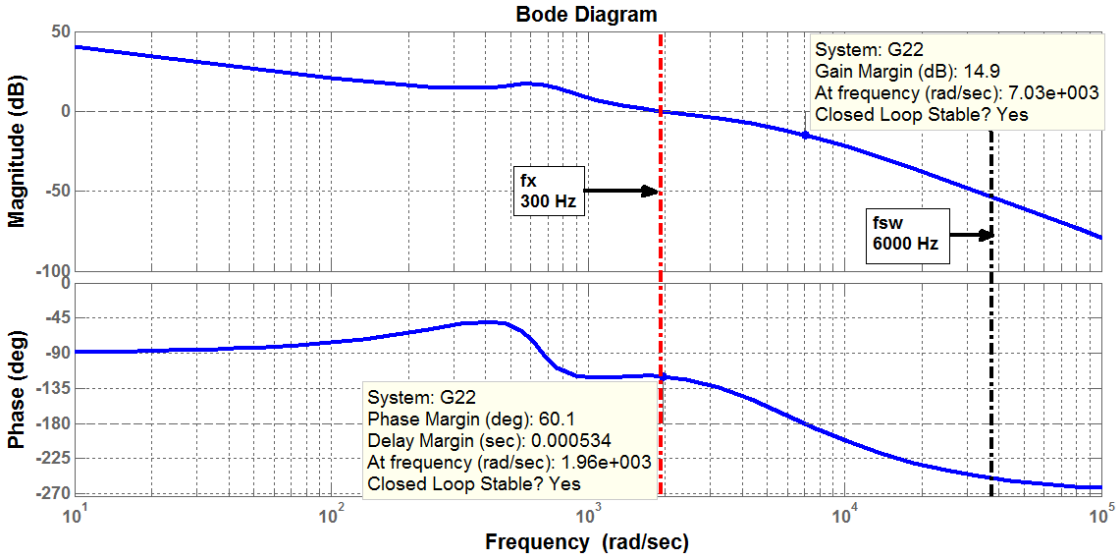

Fig. 2.9: Bode plot of the open-loop transfer function of the system under light load condition.

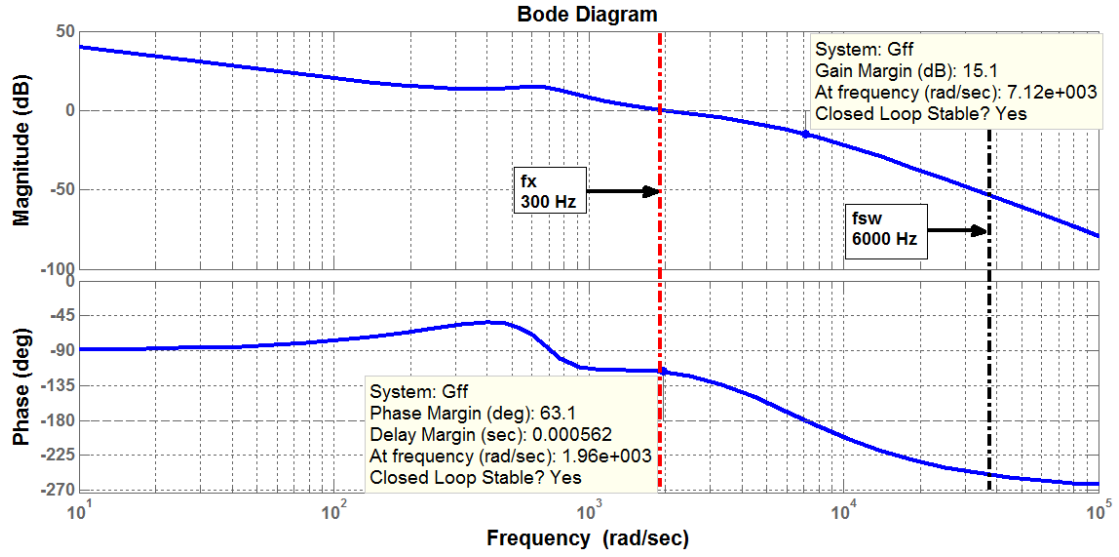

Fig. 2.10: Bode plot of the open-loop transfer function of the system under Full-load condition.

It should be noticed from Fig. 2.9 and Fig. 2.10 that the gain at switching frequency, f_{sw}, is about -50 dB, this gain is large enough to eliminate the harmonics of the output voltage of the inverter.

The next step is to design the three-phase VSI by MATLAB/Simulink and verify the response using the designed voltage controller.

2.4 Performance of the VSI under linear balanced loads in steady state

The performance of the three-phase VSI has been done by using MATLAB/Simulink. A balanced linear loads with different values has been applied. The inverter's rating is 20 kVA and it is operating at stand-alone with variable loading conditions. The output frequency of the inverter under this case is constant and equal to 50 Hz as well as the output voltage which is 311.13 V peak value, or 220 V rms. Two loading conditions has been chosen in order to check the performance of the inverter: full load condition (20 kW) and very light load (the worst condition of 10 W) in order to verify the voltage controller performance and check if the inverter will be able to regulate the output voltage. Fig. 2.11 show the schematic of the system under test.

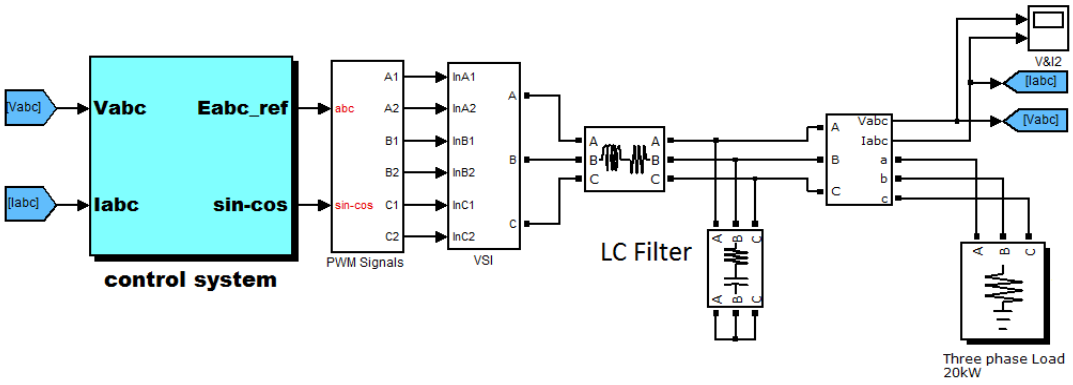

Fig. 2.11: Simulink model of three-phase VSI feeding local load.

The output current and voltage of inverter (after the LC filter) are measured and being sent to the control system block shown in Fig. 2.11. The control system has three blocks as shown in Fig. 2.12 .

The first block in the control system block is the Voltage reference generator. The input of the voltage reference generator are the operating frequency and the output voltage required for the VSI. This block uses a phase-looked loop in order to detect the frequency and the phase angle of the grid voltage when the VSI is being connected to the grid as will be shown later. At this time, the input voltage and frequency of the phase-locked loop

(PLL) block are constants. The PLL then generates reference three-phase voltages with the desired amplitude and frequency. These voltages are then transformed into two component in synchronous rotating reference frame using Park transform as shown in Fig. 2.13. The *d*-axis voltage V_d equals the peak value of the VSI output voltage while the *q*-axis voltage V_q equals zero.

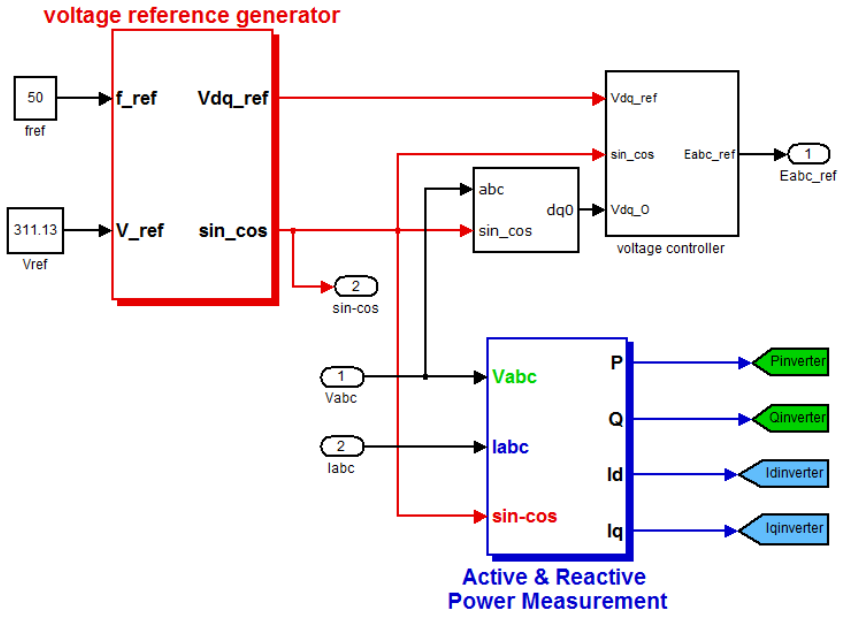

Fig. 2.12: Control System of the three-phase VSI

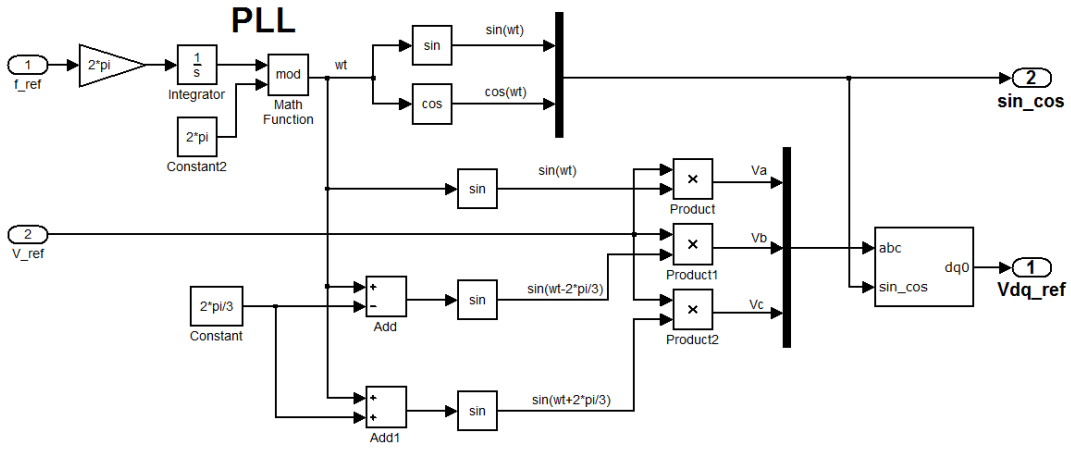

Fig. 2.13: Voltage reference generator block:

The second block inside the control system is the active and reactive power measurement in which the measured output voltage and current of the VSI are input to this block. Here the VSI is feeding a local load directly so this block provides only the

output power and reactive power of the VSI. The third block is the voltage controller in which the reference *d*- and *q*-axis voltages provided by the voltage reference generator block are being compared with the measured values and being controlled through the controller described in (2.16).

Finally, the output of the voltage controller block will be transformed back into *abc* reference frame to be used as three sinusoidal reference signals for the sinusoidal pulse width modulation generator (PWM) block to control the switching state of VSI.

The first test is done under **20 kW** load, the inverter output voltage and current are shown in Fig. 2.14.

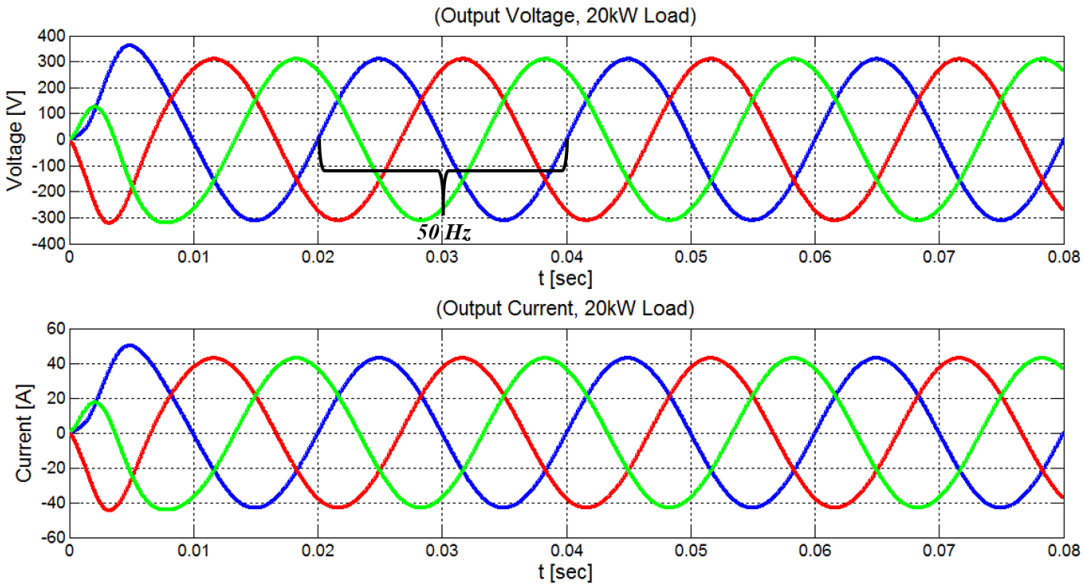

Fig. 2.14 Output voltage and current of the VSI feeding 20 kW load.

It is obvious from the simulation results that the inverter is able to regulate the output voltage and frequency under linear full load condition. The output voltage has a good sinusoidal shape as well as the output current as shown in Fig. 2.14. The output frequency is 50 Hz as required.

The output average power and reactive power are shown in Fig. 2.15.

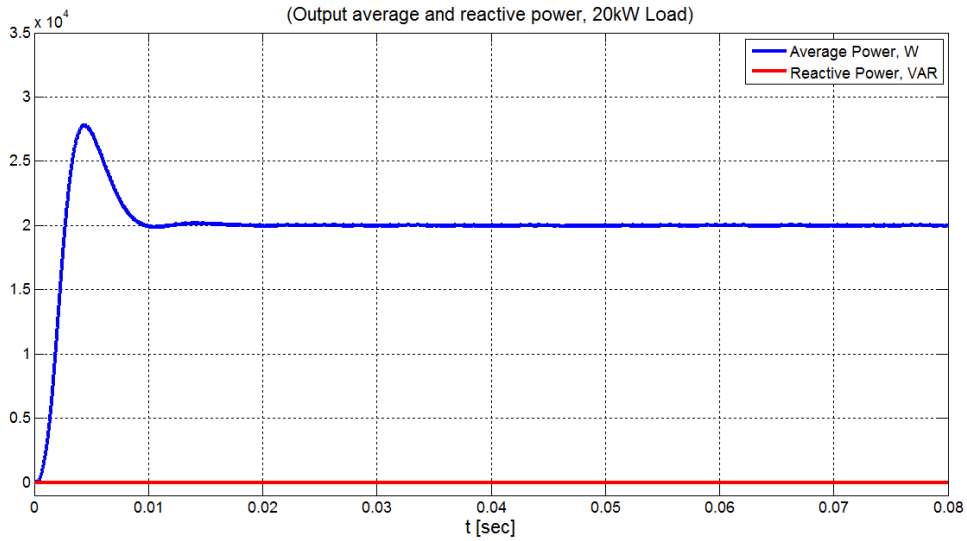

Fig. 2.15 Output average and reactive power of the VSI feeding 20 kW load.

It should be mentioned that inverter has been subjected to a sudden load change, since the load applied to the inverter has been changed from 0% to 100% of the rated power. The output power of the inverter as shown in Fig. 2.15 has a small settling time that does not exceed 0.015 seconds and the percentage overshoot does not exceed 39%. This verifies the perfect functionality of the proposed voltage controller.

Now, taking into account the worst loading condition, a very light load with a value of 10 W has been connected to the inverter with the same voltage controller used in the previous case. The output performance of the inverter are shown in the next figures.

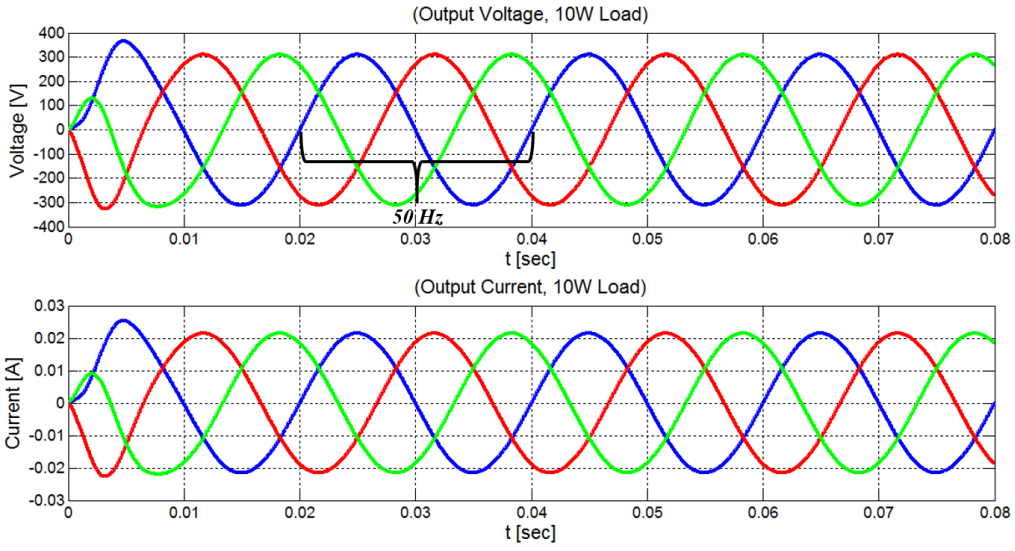

Fig. 2.16 Output voltage and current of the VSI feeding 10 W load.

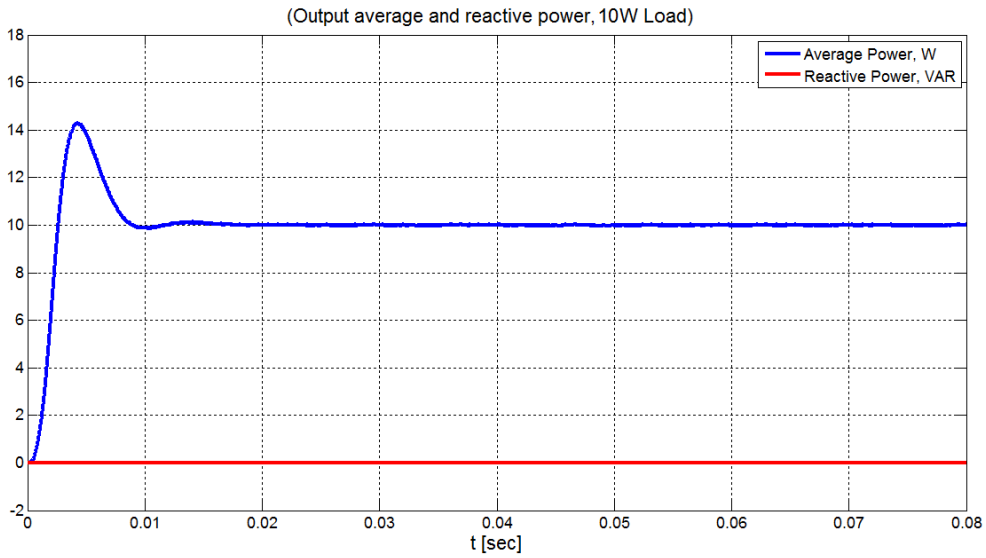

Fig. 2.17 Output average and reactive power of the VSI feeding 10 W load.

It is clear from Fig. 2.16 and Fig. 2.17 that the inverter's performance under light load condition is also presenting a good power quality with a good transient response. In Fig. 2.16, the output voltage and current have a good sinusoidal shape and the output frequency of the inverter is 50 Hz as expected.

The output power of the inverter as shown in Fig. 2.17 has a small settling time the same as in the previous case, it does not exceed 0.015 seconds and the percentage overshoot is approximately 41%. This verifies the perfect functionality of the proposed voltage controller under very light loading condition.

The final test of the VSI will be the operation under different loading conditions. The loading sequence of the system under test is as follow:

1- From 0.0-0.1 sec.: The load is 300 W and 0 kVAR

2- From 0.1-0.2 sec.: The load is 6 kW and 0 kVAR

3- From 0.2-0.35 sec.: The load is 16 kW and 3 kVAR

The output voltage, current, average power and reactive power are shown in the following figures.

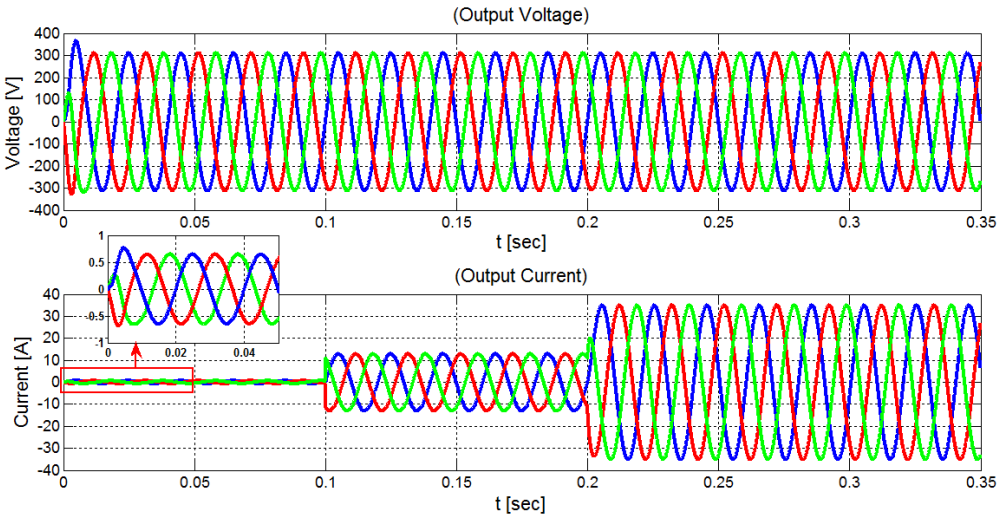

Fig. 2.18: Output voltage and current of the three-phase VSI under different loading conditions.

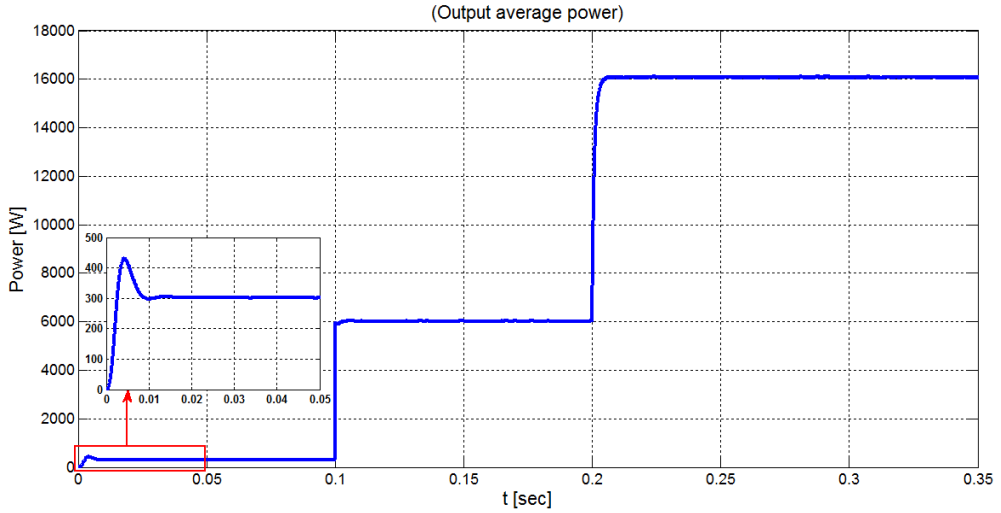

Fig. 2.19: Output average power of the three-phase VSI under different loading conditions.

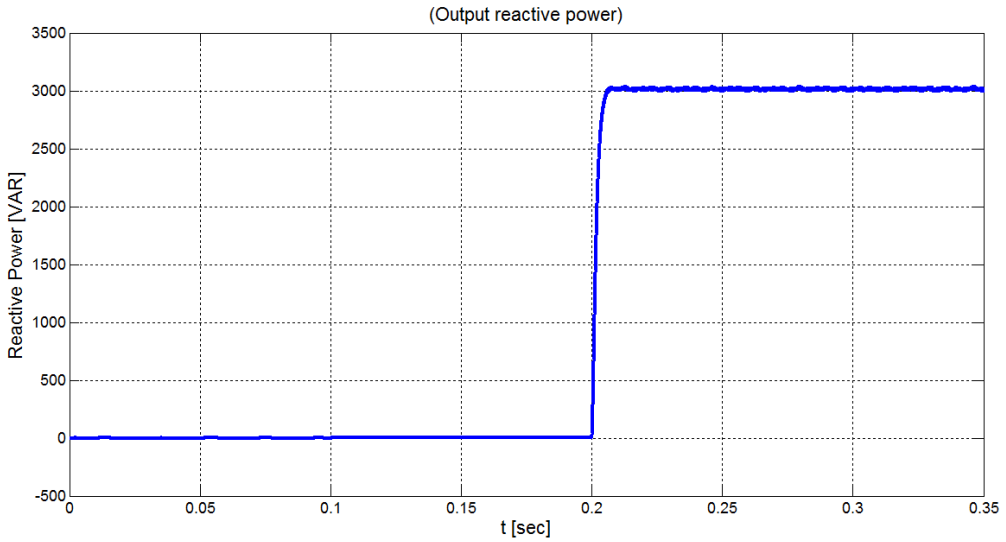

Fig. 2.20: Output reactive power of the three-phase VSI under different loading conditions.

As seen from Fig. 2.18, the output voltage and current were kept in a perfect sinusoidal shape under all the loading conditions the inverter was subjected to. Moreover, the output average power and reactive power shown in Fig. 2.19 and Fig. 2.20 have fast transient response and very low percentage overshoot although the inverter has been subjected to a reactive load after 0.2 seconds.

The next step of the research, the VSI with the voltage controller will be operated under a droop-base active and reactive power loops such that it will be connected to a distribution grid without any communication means.

2.5 Performance of the VSI connected to a stiff grid under linear balanced loads in steady state

Now the operation of a droop controlled inverter connected to a stiff grid through a distribution line has been tested. The distribution line has *R/X* ratio equal to 7.7 since we are working with a low-voltage network or mini-grid [8]. The stiff grid has been considered as a constant voltage source with a constant magnitude (380 V_{L-L}) and frequency (50 Hz).

The schematic of the on-grid operation of droop controlled VSI is shown in Fig. 2.21.

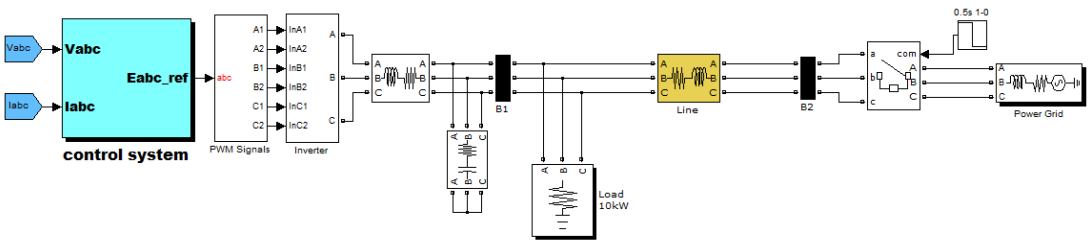

Fig. 2.21: Parallel Operation of the VSI with a stiff grid.

The inverter presents an output LC filter and a local load and connected to the grid through a feeder. The inverter's output voltage and current are measured in order to

calculate the output average and reactive power of the inverter which represents the outer loop. The droop curves will provide the reference voltage and frequency.

The "Voltage Reference Generator" block will converts the voltage and frequency references from droop controllers into a three-phase balanced signal with the required frequency which will be converted into *dq* reference frame again. Then these voltage references in *dq* are compared to the actual *dq* voltages measured across the filter capacitors and they will be regulated by the voltage controller described in (2.16).

Fig. 2.22 shows the schematic of the outer and inner control loops of the VSI. The reference $E_{abc\text{-}ref}$ will be compared with the triangular carrier signal in order to generate the PWM signals for the inverter.

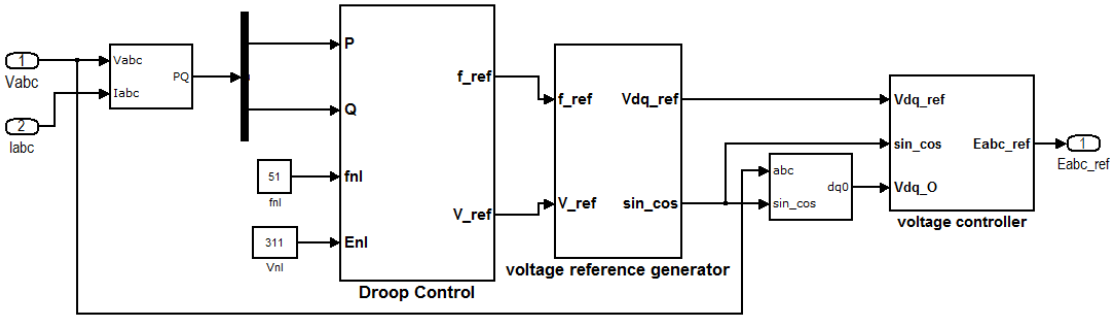

Fig. 2.22: Outer loop (droop control loop) and inner loop (voltage control loop) of the VSI

The droop equations could be written as follows [12], [13], [47], [52], [53], [58], [59];

$$P = \frac{\omega_{nL} - \omega_{ref}}{m_P} \tag{2.17}$$

$$Q = \frac{V_{nL} - V_{ref}}{n_Q} \tag{2.18}$$

where,

- ω_{ref} and V_{ref} are the angular frequency and voltage magnitude references, respectively.
- ω_{nL} and V_{nL} are the no-load angular frequency and voltage, respectively.
- m_P and n_Q are the active and reactive droop slopes, respectively.

- *P* and *Q* are the output active and reactive power, respectively.

Synchronous generators as a distributed generator widely adopt the droop control technique. To ensure a safe parallel operation of multi VSI DGs in the microgrid, and an accurate power sharing among DGs according the power ratings of each DG to cover the power demand, and to ensure that all DGs are working under the same frequency; the *P vs. f* droop loop should be adopted [60].

On the other hand, *Q vs. V* droop loop is important if the distribution line impedance between the DGs and loads was not identical. Different line impedance between DGs and loads will allow a circulation current to flow between the DGs and the function of *Q vs. V* droop loop is minimizing this circulation currents [60].

Fig. 2.23 shows the droop controller of the VSI. Note that the low-pass filter is used in order to filter the instantaneous *P* and *Q* and to slow down their variations. This will make the outer loop slower than the inner loop as required. In this case, the reactive power controller is disabled and the inverter is working under constant output power and voltage during the on-grid operation. The coupling between the active and reactive power in LV microgrid is obvious. The no-load frequency (f_{nl}) is 51 Hz and the no-load voltage (V_{nl}) is 311 V.

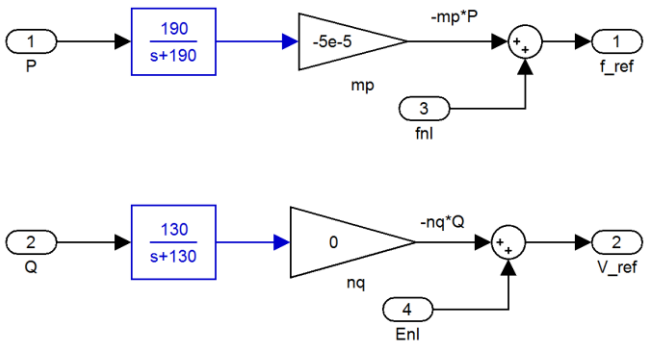

Fig. 2.23: Droop curve, P vs. f and Q vs. V

The simulation of the above mentioned system is carried out. Taking into account that a 10 kW load is being connected directly to the output of the VSI and the system has been

tested under two scenarios. The first scenario, from 0-0.5 sec, the inverter is operating in parallel with the grid (on-grid operation). The second one, from 0.5-1 sec, the grid has been disconnected and the inverter is operating under stand-alone mode (Islanded mode).

Table 2.2 lists the parameters of the system under test.

Table 2.2: system parameters

Parameter	Value
V_{grid}	380 V_{L-L}
f_{grid}	50 Hz
m_P	$-5*10^{-5}$
n_Q	0
f_{nl}	51 Hz
v_{nl}	311 V (Peak value)
R_{Line}	0.3210 Ω
X_{Line}	0.0415 Ω
P_{Load}	10 kW

The following figures show the simulation results of the system.

In Fig. 2.24, and during the first half second, the output power of the inverter is 20 kW, which is the full load capacity of the inverter even though the local load is 10 kW. This is because the inverter is connected to the grid and the output frequency of the inverter should match the grid frequency as the PLL detects the operating frequency of the grid which is 50 Hz. During the design of the droop curve, 50 Hz is corresponding to the rated power of the inverter (20 kW).

After disconnecting the grid (after 0.5 seconds), the output power of the inverter will drop into 10 kW which is the power demanded by the local load. The inverters output reactive power is shown in Fig. 2.25.

It should be noticed that during the transition between the on-grid to islanded mode operation, the output average power presents a high overshoot value as seen in Fig. 2.24. A solution can be found by modifying the inner control loop and it can be achieved by adding a current control loop after the voltage controller. This will have the advantage of having a smooth transition between the on-grid and Islanded modes and overcomes the

problem of having high overshoot in the output power of the inverter. Because the thesis focuses on Islanded microgrids, a simple voltage controller has been adopted as an inner control loop of the VSIs.

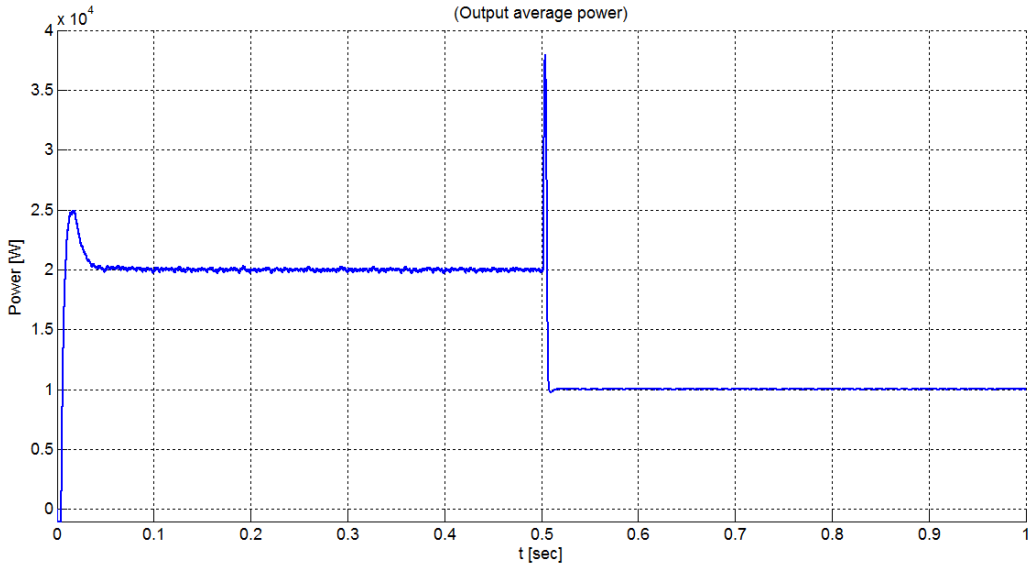

Fig. 2.24: Inverter output active power (W)

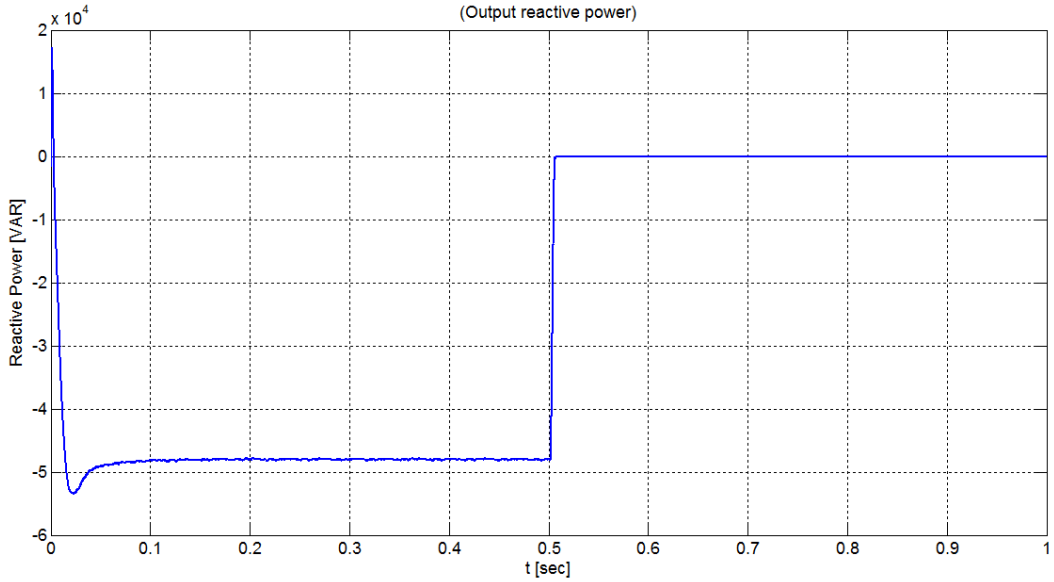

Fig. 2.25: Inverter output reactive power (VAR)

The output *d*- and *q*-axis current of the inverter is shown in Fig. 2.26. It is very clear from this figure that the high overshoot value in the output power of the inverter is mainly contributed by overshoot in the *d*-axis current and adopting the current control loop will solve this issue.

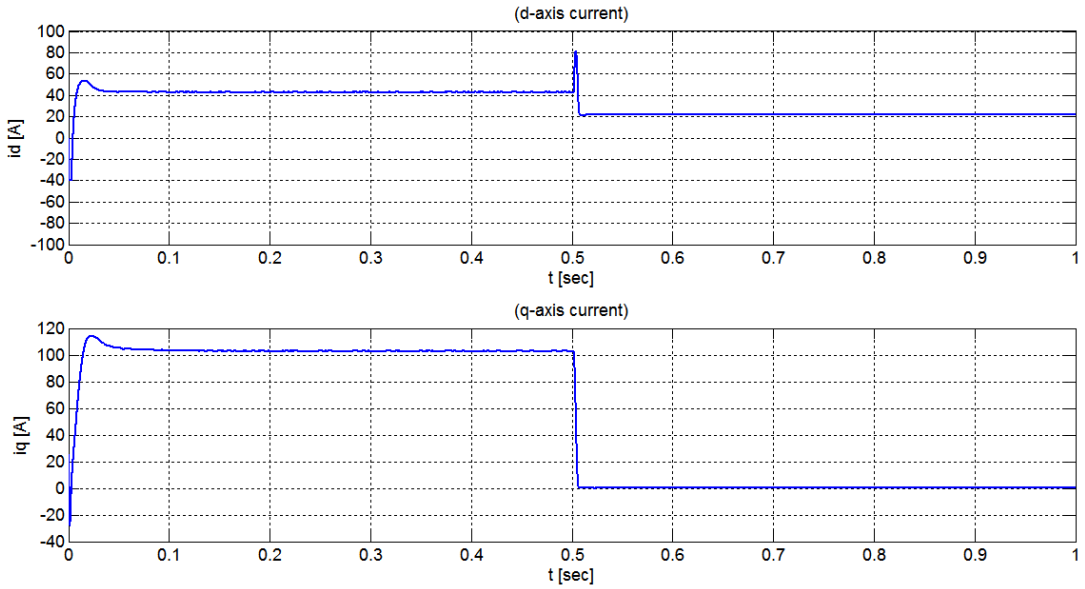

Fig. 2.26: Inverter output *d*- and *q*-axis currents (A)

The output frequency of the inverter under this configuration is shown in Fig. 2.27. As mentioned before, when the inverter was operating under on-grid mode, the inverter output frequency was 50 Hz (the grid frequency) and after disconnecting the grid, the output frequency of the inverter has been increased to 50.5 Hz. This is the basic operation of the *P vs. f* droop curve. Increasing the load leads to decrease the output frequency and vice versa.

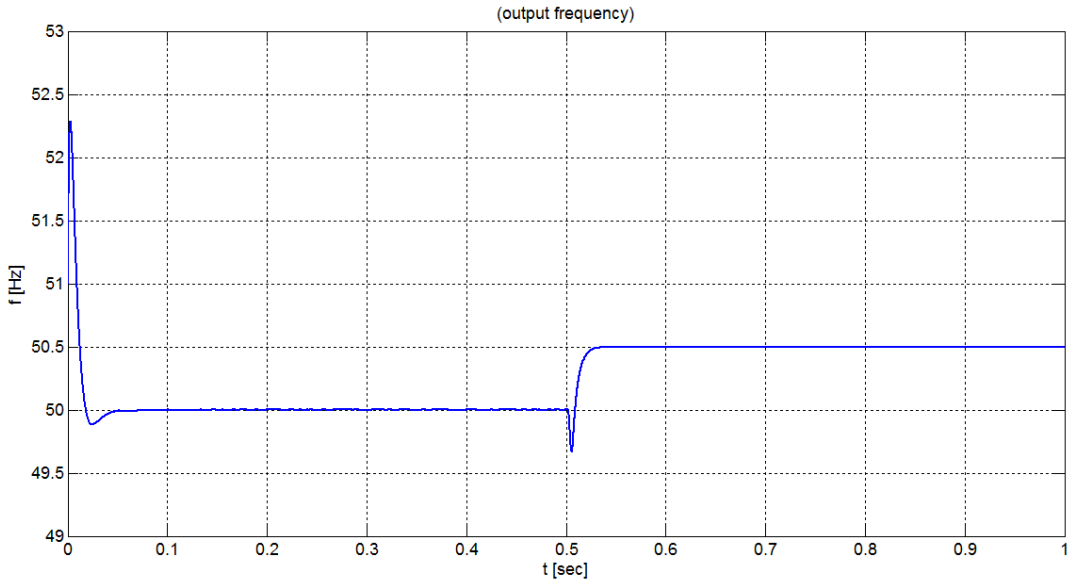

Fig. 2.27: Inverter output frequency (Hz)

It is quite interesting to mention that when the inverter was operating under on-grid mode, the output power of the inverter was 20 kW (the nominal power) while the local load is 10 kW. In this case, the VSI is transporting power to the grid.

If there were two or more VSI DGs with different power ratings operating on the same microgrid under the proposed configuration, and under the on-grid operation mode, the output power of each DG will be the nominal power of the individual VSI DG. The droop controller of each DG should be designed according to the power ratings of each inverter.

Chapter 3 Electrostatic Synchronous Machines concept

In this chapter, a modified method of modeling the three-phase VSI using the concept of three-phase electrostatic synchronous generator (ESG) is developed. The construction and operation of the three-phase ESG is described in detail. The dq equivalent model is derived. The concept of mutual capacitance between the stator and the rotor is explained in order to understand how to implement this mutual capacitance during the modeling. The electrostatic generator's phase coordinate model, or the phase-variable model with self and mutual time-varying capacitances that depends on the rotor position is explained. Then, the dq model has been derived in order to get rid of the time-varying capacitance which make the modeling and analysis easier. The assumptions used for simplifying the modeling of three-phase ESG are explained.

3.1 Construction and operation of Three-Phase Electrostatic Synchronous Generators

As conventional three-phase Synchronous Generators, the three-phase ESGs are composed of a rotor and a stator, and each of them has two parallel plates facing each other and thus forming a capacitor and working under high vacuum. In conventional synchronous machines, electromagnetism plays the main rule of their operation while electrostatic is used to describe the operation of electrostatic machines with capacitors.

As shown in Fig. 3.1, the field plates are located on the outside virtual shaft of the rotor. The field plates are fed with a direct voltage source, namely the field voltage V_f. This direct voltage source will produce an electric field. The left plate of the field in Fig. 3.1 always holds a positive charge as it is connected to the positive terminal of V_f while the right plate holds a negative charge (connected to the negative terminal of V_f).

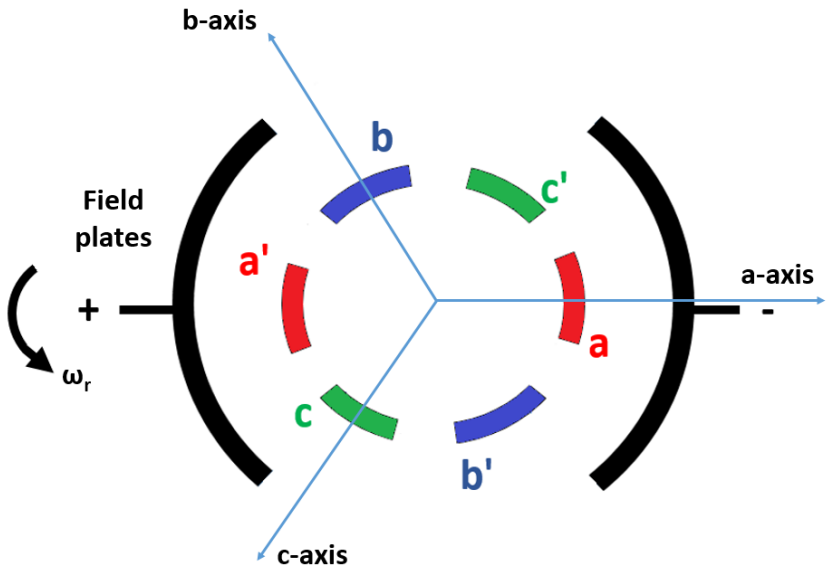

Fig. 3.1: Construction of three-phase ESG.

The stator plates (inner plates) *a-a'*, *b-b'* and *c-c'* shown in Fig. 3.1 are distributed in the space and shifted by 120° from each other and thus forming three-phase capacitors. The field plates are rotating at synchronous speed ω_r and thus creating a rotating electric field. As the rotor rotates at synchronous speed, the rotating electric field will induce alternating charges on the stator plates. These inner plates will hold an electric charge (Q).

3.2 The Phase-Variable model of Three-Phase Electrostatic Generators

The phase-variable model of the ESG is formed by a set of three stator circuits, which are coupled with the rotor circuit through the rotation of the rotor. The rotor electric field is always aligned with the *d*-axis as shown in Fig. 3.2. The stator and the rotor are electrically coupled with each other.

For the sake of simplicity, the following assumptions have been considered:

1- Both the rotor and stator plates were considered as parallel plane plates. This is shown in Fig. 3.3.

2- Both the rotor and stator plates have the same cross sectional area A.

3- The displacement between plates are as shown in Fig. 3.3.

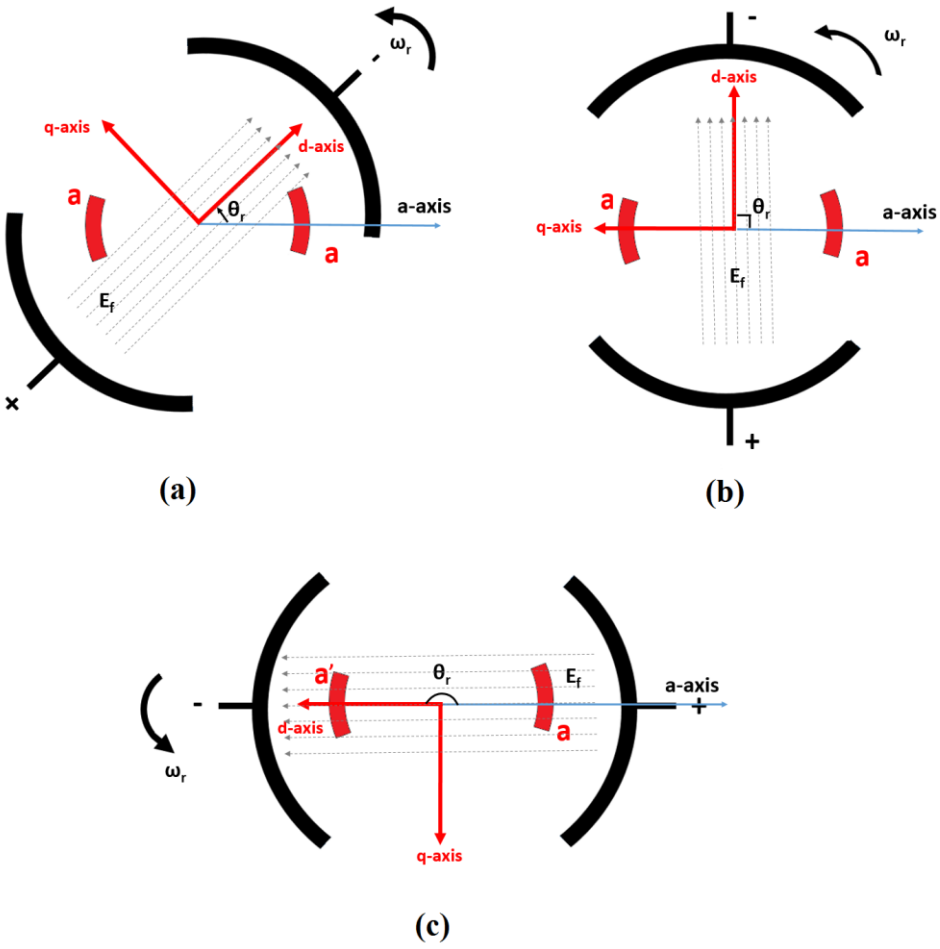

Fig. 3.2: Field plates with the a-phase of ESG. (a) alignment of the rotor field with the *d*-axis. (b) $\theta_r=\pi/2$. (c)$\theta_r=\pi$.

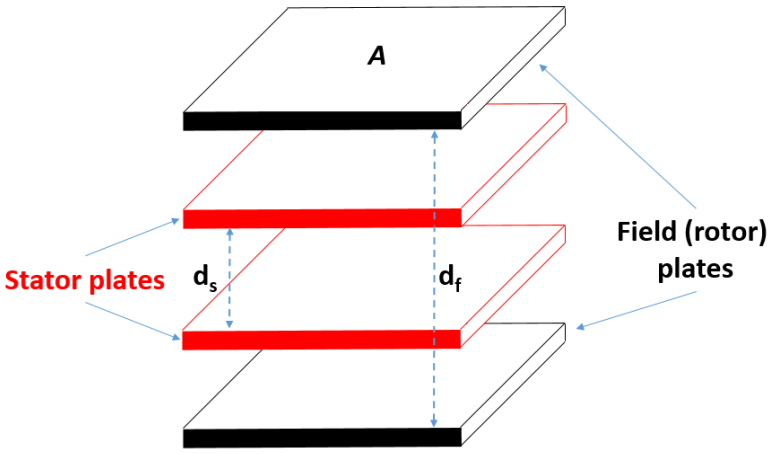

Fig. 3.3: Geometry of the rotor and stator capacitor.

When the outer plates (rotor plates) are connected to a DC voltage source, then each plate will hold a charge according to the polarity of the terminal it is connected to, this

will establish an electric field traveling from the positive to the negative terminal. As the stator plates are subjected to this electric field, by induction, they will hold an electric charge with the order as described in Fig. 3.4.

It is clear from Fig. 3.4 that there is a mutual capacitance between the rotor and the stator (inner and outer plates). This mutual capacitance is in series with the stator self-capacitance [76]–[82]. As the rotor rotates, for example, as shown in in Fig. 3.2 (a), self and mutual capacitance will change according to the rotor position θ_r. This is because the effective cross sectional area will decrease with respect to the d- and q-axis (A_d and A_q, respectively). This concept is helpful in deriving the equivalent model of the ESG. When the rotor rotates by 90^o (Fig. 3.2 (b)), the rotor electric field does not pass through the stator plates and thus both the self and mutual capacitance will be zero. The last case is Fig. 3.2 (c), when the rotor rotates by 180^o, then the self and mutual stator capacitors will hold a negative charge as an effect of reversing the direction of the rotor electric field.

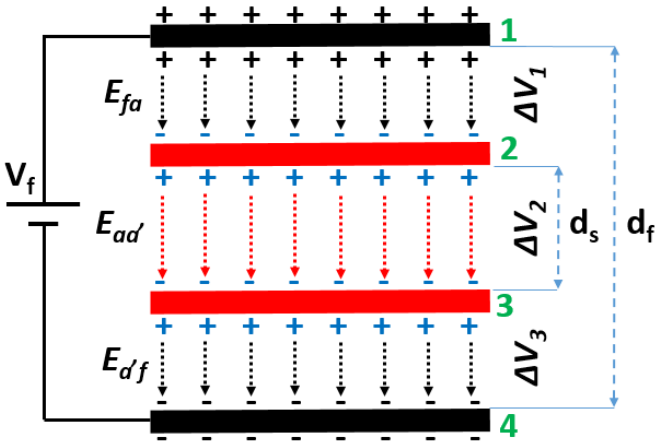

Fig. 3.4: Electric field distribution in ESG

Fig. 3.5 shows the phase-variable model of the three-phase ESG. After the basic operation of the ESG has been explained, the self and mutual capacitance can be derived in the following subsections.

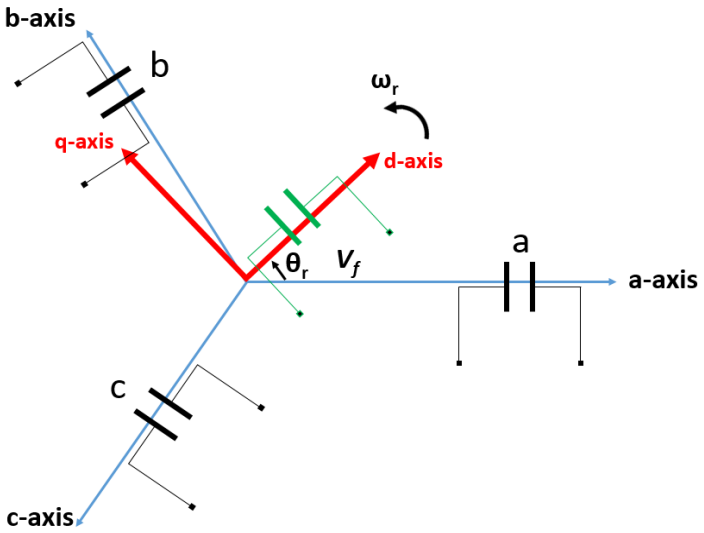

Fig. 3.5: Phase-Variable model of the ESG.

3.2.1 Self-Capacitance of stator plates

In order to calculate the self-capacitance of each phase of the ESG, we will consider the electrostatic effect of just the *a*-phase voltage established in the stator. As mentioned before, the *d*-axis is aligned with the rotor electric field E_f, and thus, the electric field components of phase *a* along the *d*- and *q*-axis with the help of Fig. 3.6 are:

$$E_a = E_{ad}\, cos\, \theta_r - E_{aq}\, sin\, \theta_r \tag{3.1}$$

and taking into consideration that

$$\Delta V = dE \tag{3.2}$$

$$Q = \epsilon_o A\, E \tag{3.3}$$

where ΔV is the voltage difference across the capacitor (V), d is the distance between the plates (m), E is the Electric field. (V/m), Q is the electric charge (C - coulomb), ε_o is the permittivity of free space, which is equal to $8.854*10^{-12}$ F/m and A is the cross sectional area of the plates (m^2).

Another assumption has been made which is neglecting the fringing effect and assuming a uniform electric field. All the electric field will travel from the +ve plate to the –ve one without any losses.

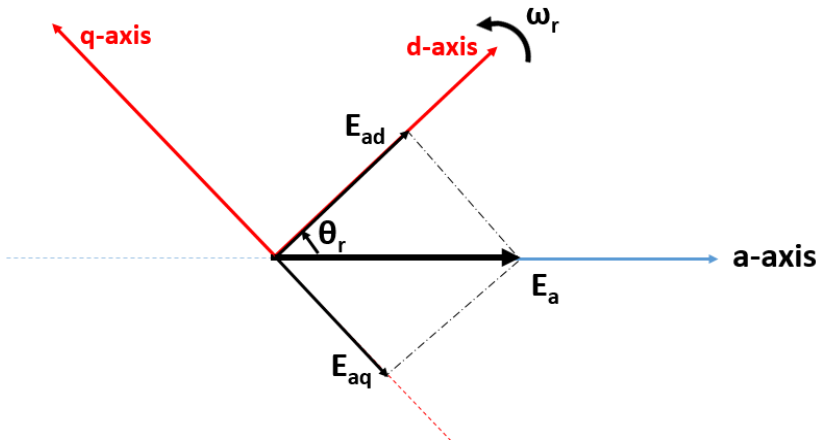

Fig. 3.6: Electric field components of the a-phase along the *dq* axis.

The electric charge on *a*-phase is:

$$
\begin{aligned}
Q_{aa} &= \epsilon_o A\, E_a \\
&= \epsilon_o \left(A_d\, E_{ad} \cos\theta_r - A_q E_{aq} \sin\theta_r\right) \\
&= \frac{\epsilon_o}{d_s}\left(A_d\, V_{ad} \cos\theta_r - A_q V_{aq} \sin\theta_r\right) \\
&= \frac{\epsilon_o}{d_s} V_a \left(A_d \cos^2\theta_r + A_q \sin^2\theta_r\right) \\
&= \frac{\epsilon_o}{d_s} V_a \left(\frac{A_d}{2}[1+\cos(2\theta_r)] - \frac{A_q}{2}[1-\cos(2\theta_r)]\right)
\end{aligned}
$$

where A_d and A_q are the effective plate area under *d*- and *q*-axis, respectively. Now Q_{aa} is as follow:

$$Q_{aa} = \left[\frac{1}{2}\frac{\epsilon_o(A_d + A_q)}{d_s} + \frac{1}{2}\frac{\epsilon_o(A_d - A_q)}{d_s}\cos(2\theta_r)\right] V_a \tag{3.4}$$

which means that the self-capacitance C_{aa} of phase *a* is:

$$C_{aa} = \left[\frac{1}{2}\frac{\epsilon_o(A_d + A_q)}{d_s} + \frac{1}{2}\frac{\epsilon_o(A_d - A_q)}{d_s}\cos(2\theta_r)\right] \tag{3.5}$$

or;

$$C_{aa} = \left[\frac{C_{max} + C_{min}}{2} + \frac{C_{max} - C_{min}}{2}\cos(2\theta_r)\right] \tag{3.6}$$

where $C_{max} = \frac{\epsilon_o A_d}{d_s}$ and $C_{min} = \frac{\epsilon_o A_q}{d_s}$.

Writing the self-capacitance in a simpler form:

$$C_{aa} = C_o + C_1 \cos 2\theta_r \tag{3.7}$$

where $C_o=(C_{max}+C_{min})/2$ and $C_1=(C_{max}-C_{min})/2$. The *b*- and *c*-phase self-capacitance C_{bb} and C_{cc} are similar that of C_{aa} but with θ_r is replaced by (θ_r - 2π/3) and (θ_r + 2π/3), respectively.

$$C_{bb} = C_o + C_1 \cos 2\left(\theta_r - \frac{2\pi}{3}\right) \tag{3.8}$$

$$C_{cc} = C_o + C_1 \cos 2\left(\theta_r - \frac{2\pi}{3}\right) \tag{3.9}$$

It is clear from (3.7), (3.8) and (3.9) that the stator self-capacitance is time-varying, or in other words, depends on the rotor position. The leakage capacitance will be excluded in the modeling for the sake of simplicity and the virtual ESG is assumed to be ideal.

3.2.2 Mutual Capacitance between stator phases

Now the charges from the *a*-phase due to the electric fields E_{ad} and E_{aq} transferred to *b*-phase plates that is 2π/3 ahead is:

$$Q_{ba} = Q_{ab} = \frac{\epsilon_o}{d_s} V_a\left(A_d \cos\theta_r \cos\left(\theta_r - {}^{2\pi}/_{3}\right) - A_q \sin\theta_r \sin\left(\theta_r - {}^{2\pi}/_{3}\right)\right) \tag{3.10}$$

Simplifying (3.10) yields to:

$$Q_{ba} = \left[-\frac{\epsilon_o\left(A_d + A_q\right)}{4d_s} + \frac{\epsilon_o\left(A_d - A_q\right)}{2d_s}\cos\left(2\theta_r - {}^{2\pi}/_{3}\right)\right] \tag{3.11}$$

which means that the mutual capacitance between the *a*- and *b*-phase is:

$$C_{ba} = C_{ab} = -\frac{C_o}{2} + C_1 \cos 2\left(\theta_r - {}^{\pi}/_{3}\right) \tag{3.12}$$

and those of *a*-*c* and *b*-*c* are:

$$C_{ac} = C_{ca} = -\frac{C_o}{2} + C_1 \cos 2\left(\theta_r + {}^{\pi}/_{3}\right) \tag{3.13}$$

$$C_{bc} = C_{cb} = -\frac{C_o}{2} + C_1 \cos 2\theta_r \tag{3.14}$$

3.2.3 Mutual Capacitance between the stator and the rotor plates

With the help of Fig. 3.4 and Fig. 3.7, the *q*-axis component of the rotor electric field (E_{fq}) is always zero because the *d*-axis is aligned with the rotor electric field. The voltage difference between the outer plates (rotor plates) is the field voltage V_f. Then it is clear

that the mutual capacitance between the rotor and the stator is modeled in series between them, and because of the symmetry of the plate displacements it is easy to find this mutual capacitance.

Starting from the potential difference:

$$\Delta V_{tot} = V_f = \Delta V_1 + \Delta V_2 + \Delta V_3 \tag{3.15}$$

Here ΔV_{tot} equals the field voltage V_f and the potential difference between the rotor and the stator is:

$$\Delta V_{f-a} = \Delta V_1 + \Delta V_3 \tag{3.16}$$

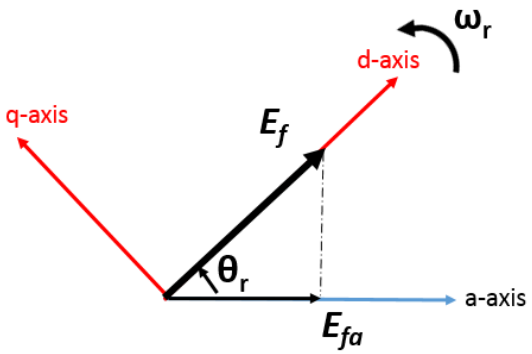

Fig. 3.7: Electric field components of the rotor plates along the *a*-axis

So, we can find the equivalent mutual capacitance between the rotor and the stator according to the following notes:

1- The mutual capacitance is calculated when the field voltage is applied and without loading the ESG.

2- The mutual capacitance on both sides and the self-capacitance of the stator share the same charge as they are in series.

3- Each capacitor will have different potential according to the spacing between the plates. But the mutual capacitance on both sides have the same displacement between the rotor and the stator plates which means that the capacitance values are equal.

According to the third point, the mutual capacitance on both sides will have the same potential difference, so we can start from that point and after redrawing Fig. 3.4 as seen in Fig. 3.8; the mutual capacitance between the rotor and the stator can be calculated as follow:

$$Q_{fa} = C_{M1}\Delta V_1 = C_{aa}\Delta V_2 = C_{M2}\Delta V_3 \tag{3.17}$$

Where C_{M1} is the first mutual capacitance between plates 1 and 2, and C_{M2} is the second mutual capacitance between plates 3 and 4. As seen in (3.17), the mutual capacitance will induce a current in the stator circuit as a response to the voltage change between the rotor and stator; ΔV_1 and ΔV_3, respectively. This is why it has to be modeled in series between the rotor and the stator circuits.

Rewriting (3.17) in terms of the electric field vectors:

$$Q_{fa} = \epsilon_o A\overrightarrow{E_{1\to 2}} \tag{3.18}$$

The last term in (3.23) is half of the total electric field between the rotor and the stator, so (3.23) becomes:

$$Q_{fa} = \epsilon_o A\left(\frac{1}{2}\overrightarrow{E_{fa}}\right) \tag{3.19}$$

Remembering that E_{fq} equals zero, and the relationship between E_{fa} and ΔV_{fa} is:

$$\begin{aligned}\Delta V_{fa} &= \Delta V_1 + \Delta V_3 \\ &= \frac{d_f - d_s}{2}\overrightarrow{E_{1\to 2}} + \frac{d_f - d_s}{2}\overrightarrow{E_{3\to 4}} \\ &= \frac{d_f - d_s}{2}\left(\overrightarrow{E_{1\to 2}} + \overrightarrow{E_{3\to 4}}\right) \\ &= \frac{d_f - d_s}{2}\left(\overrightarrow{E_{fa}}\right)\end{aligned}$$

then:

$$Q_{fa} = \left(\frac{\epsilon_o A_d}{d_f - d_s}\cos\theta_r\right)\Delta V_{fa} \tag{3.20}$$

So, we can conclude that the equivalent mutual capacitance between the rotor and the stator is:

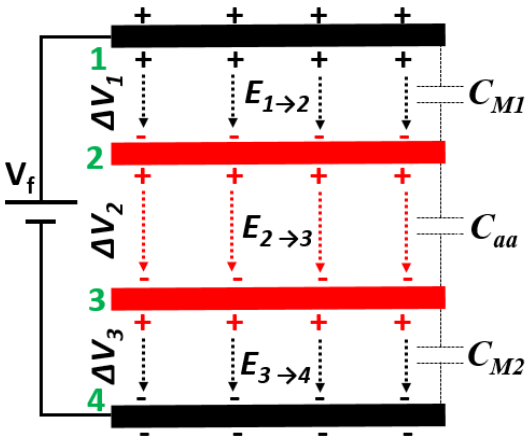

Fig. 3.8: Mutual capacitance between the rotor and stator plates.

$$C_{Mf-a} = \frac{\epsilon_o A_d}{(d_f - d_s)} \cos\theta_r \tag{3.21}$$

In (3.21), $C_{Mf\text{-}a}$ is the equivalent of the series mutual capacitance between the rotor and the stator plates. Since they have the same value and they are in series, then $C_{Mf\text{-}a}$ is half of C_{M1} or C_{M2}. This mutual capacitance varies with the rotor position. The mutual capacitance between the rotor and the *b*- and *c*-phase are similar to that of $C_{Mf\text{-}a}$ but with θ_r is replaced by (θ_r - 2π/3) and (θ_r + 2π/3), respectively. For simplicity, we will define the mutual capacitance as follow:

$$C_{Mf-a} = C_M \cos\theta_r \tag{3.22}$$

$$C_{Mf-b} = C_M \cos(\theta_r - 2\pi/3) \tag{3.23}$$

$$C_{Mf-c} = C_M \cos(\theta_r + 2\pi/3) \tag{3.24}$$

where:

$$C_M = \frac{\epsilon_o A_d}{(d_f - d_s)} \tag{3.25}$$

Finally, the self-capacitance of the rotor plates (which is aligned with the *d*-axis) can be defined as follow:

$$C_{rr} = \frac{\epsilon_o A}{d_f} \tag{3.26}$$

where C_{rr} is always constant and does not depend on the rotor position.

3.3 The *dq* model of Three-Phase Electrostatic Generators

As seen in deriving the mutual and self-capacitance of the three-phase ESG, these capacitances are time-variant and changing with the rotation of the rotor. Transforming the *abc* quantities into *d-q* will cancel the dependence of these capacitances with the rotor position. Moreover, as it will be seen, it will cancel the mutual capacitance between the stator plates. The *d-q* model will transform the equations of the stator and the rotor into *dq* reference frame in which the *d*-axis of the reference frame is aligned with the rotor electric field. This means that *dq* transformation should be applied to the stator phase quantities only.

The transformation used is the conventional Park transformation described in (2.9) and will be rewritten here as follow:

$$[T_{dqo}] = \frac{2}{3}\begin{bmatrix} \cos\theta_r & cos(\theta_r - 2\pi/3) & cos(\theta_r + 2\pi/3) \\ -\sin\theta_r & -\sin(\theta_r - 2\pi/3) & -\sin(\theta_r + 2\pi/3) \\ \frac{1}{2} & \frac{1}{2} & \frac{1}{2} \end{bmatrix} \tag{3.27}$$

and its inverse is:

$$[T^{-1}{}_{dqo}] = \begin{bmatrix} \cos\theta_r & -\sin\theta_r & 1 \\ cos(\theta_r - 2\pi/3) & -\sin(\theta_r - 2\pi/3) & 1 \\ cos(\theta_r + 2\pi/3) & -\sin(\theta_r + 2\pi/3) & 1 \end{bmatrix} \tag{3.28}$$

The derivative of the rotor angle θ_r is the rotor speed ω_r, i.e. $\omega_r = d/dt\ \theta_r$, and it should be noticed that the Park transformation multiplied by the derivative of its inverse equals to:

$$[T_{dqo}]\frac{d}{dt}[T^{-1}{}_{dqo}] = \begin{bmatrix} 0 & -\omega_r & 0 \\ \omega_r & 0 & 0 \\ 0 & 0 & 0 \end{bmatrix} \tag{3.29}$$

also, transforming from *abc* to *dq0* is:

$$\begin{bmatrix} d \\ q \\ 0 \end{bmatrix} = [T_{dqo}]\begin{bmatrix} a \\ b \\ c \end{bmatrix} \tag{3.30}$$

and from *dq0* to *abc* is:

$$\begin{bmatrix} a \\ b \\ c \end{bmatrix} = \left[T^{-1}{}_{dqo}\right] \begin{bmatrix} d \\ q \\ 0 \end{bmatrix} \tag{3.31}$$

Now the self and mutual capacitance derived in the previous section will be rewritten in a matrix form as follow:

$$[C_{ss}(\theta_r)] = \begin{bmatrix} C_{aa} & C_{ab} & C_{ac} \\ C_{ba} & C_{bb} & C_{bc} \\ C_{ca} & C_{cb} & C_{cc} \end{bmatrix} \tag{3.32}$$

$$[C_{sr}(\theta_r)] = \begin{bmatrix} C_{Mf-a} \\ C_{Mf-b} \\ C_{Mf-c} \end{bmatrix} \tag{3.33}$$

Let us consider that the stator resistance are equal such that $r_a = r_b = r_c = r_s$. Now the current equations of the stator can be arranged into the following form:

$$\begin{bmatrix} 1/r_s & 0 & 0 \\ 0 & 1/r_s & 0 \\ 0 & 0 & 1/r_s \end{bmatrix} \begin{bmatrix} v_a \\ v_b \\ v_c \end{bmatrix} + \begin{bmatrix} i_a \\ i_b \\ i_c \end{bmatrix} = \frac{d}{dt} \begin{bmatrix} Q_a \\ Q_b \\ Q_c \end{bmatrix} \tag{3.34}$$

and the equation for the stator charges is:

$$\begin{bmatrix} Q_a \\ Q_b \\ Q_c \end{bmatrix} = -[C_{ss}(\theta_r)] \begin{bmatrix} v_a \\ v_b \\ v_c \end{bmatrix} + \begin{bmatrix} V_f - v_a & 0 & 0 \\ 0 & V_f - v_b & 0 \\ 0 & 0 & V_f - v_c \end{bmatrix} [C_{sr}(\theta_r)] \tag{3.35}$$

Adopting the same methodology, the current equations of the rotor can be arranged into the following form:

$$i_f = \frac{1}{r_f} V_f + \frac{d}{dt} Q_f \tag{3.36}$$

In this type of generators, there is only one field circuit in the *d*-axis, so the rotor charge equation is:

$$Q_f = C_{Mf-a}(V_f - v_a) + C_{Mf-b}(V_f - v_b) + C_{Mf-c}(V_f - v_c) + C_{rr} V_f \tag{3.37}$$

It should be noticed that the available charges on the field plates will be the same charges available in the mutual capacitance between the rotor and stator plates.

The transformation of the stator capacitance matrix is as follow:

$$[T_{dqo}][C_{ss}(\theta_r)][T^{-1}{}_{dqo}] = \begin{bmatrix} \frac{3}{2}(C_o + C_1) & 0 & 0 \\ 0 & \frac{3}{2}(C_o - C_1) & 0 \\ 0 & 0 & 0 \end{bmatrix} \tag{3.38}$$

and the transformation of the mutual capacitance matrix is as follow:

$$[T_{dqo}][C_{sr}(\theta_r)] = \begin{bmatrix} C_M \\ 0 \\ 0 \end{bmatrix} \tag{3.39}$$

and the transformation of the electric charge derivative is as follow:

$$[T_{dqo}]\frac{d}{dt}\begin{bmatrix} Q_a \\ Q_b \\ Q_c \end{bmatrix} = \begin{bmatrix} 0 & -\omega_r & 0 \\ \omega_r & 0 & 0 \\ 0 & 0 & 0 \end{bmatrix}\begin{bmatrix} Q_d \\ Q_q \\ Q_0 \end{bmatrix} + \frac{d}{dt}\begin{bmatrix} Q_d \\ Q_q \\ Q_0 \end{bmatrix} \tag{3.40}$$

where:

$$Q_d = -\frac{3}{2}(C_0 + C_1)V_d + C_M(V_f - V_d) \tag{3.41}$$

$$Q_q = -\frac{3}{2}(C_0 - C_1)V_q \tag{3.42}$$

Now, defining a new capacitance in the *d*- and *q*-axis as follow:

$$C_d = \frac{3}{2}(C_0 + C_1) \tag{3.43}$$

$$C_q = \frac{3}{2}(C_0 - C_1) \tag{3.44}$$

So, (3.41) and (3.42) could be rewritten as follow:

$$Q_d = -C_d V_d + C_M(V_f - V_d) \tag{3.45}$$

$$Q_q = -C_q V_q \tag{3.46}$$

The stator equations are:

$$\begin{bmatrix} 1/r_s & 0 & 0 \\ 0 & 1/r_s & 0 \\ 0 & 0 & 1/r_s \end{bmatrix}\begin{bmatrix} V_d \\ V_q \\ V_0 \end{bmatrix} + \begin{bmatrix} I_d \\ I_q \\ I_0 \end{bmatrix} = \begin{bmatrix} 0 & -\omega_r & 0 \\ \omega_r & 0 & 0 \\ 0 & 0 & 0 \end{bmatrix}\begin{bmatrix} Q_d \\ Q_q \\ Q_0 \end{bmatrix} + \frac{d}{dt}\begin{bmatrix} Q_d \\ Q_q \\ Q_0 \end{bmatrix} \tag{3.47}$$

The *d*-axis stator current is:

$$I_d = -\frac{V_d}{r_s} + \omega_r C_q V_q - C_d \frac{d}{dt}V_d + C_M \frac{d}{dt}(V_f - V_d) \tag{3.48}$$

The *q*-axis stator current is:

$$I_q = -\frac{V_q}{r_s} - \omega_r C_d V_d + \omega_r C_M(V_f - V_d) - C_q \frac{d}{dt}V_q \tag{3.49}$$

The circuit representation of this type of generators is shown in Fig. 3.9.

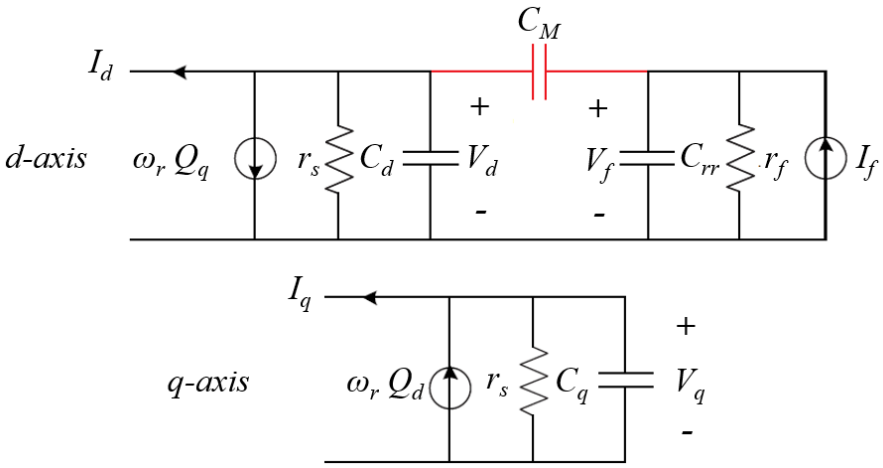

Fig. 3.9: *dq* representation of ESG.

3.4 Three-Phase ESG with double field circuits

In order eliminate the effect of unequal stator effective plate's area in the *d*- and *q*-axis (A_d and A_q) as shown in the previous sections, the ESG can be reconstructed with double field circuits, one is aligned with the *d*-axis and the other is aligned with the *q*-axis. This is explained in Fig. 3.10. In this case, the effective area of the stator plates under *d*- and *q*-axis will be the same, so $A_d = A_q = A_s$. Under this configuration, C_o in (3.7) will become:

$$C_o = \frac{\epsilon_o A_s}{d_s} \tag{3.50}$$

Thus the stator self-capacitance equations can be rewritten as follow:

$$C_{aa} = C_{bb} = C_{cc} = C_o \tag{3.51}$$

and for the stator mutual capacitance equations:

$$C_{ab} = C_{ba} = C_{bc} = C_{cb} = C_{ac} = C_{ca} = -\frac{C_o}{2} \tag{3.52}$$

Under this configuration, it is clear that the self- and mutual capacitances of the stator plates are time-invariant as described in (3.51) and (3.52). The equations of the mutual capacitance between the rotor and the stator plates along the *d*-axis are as follow:

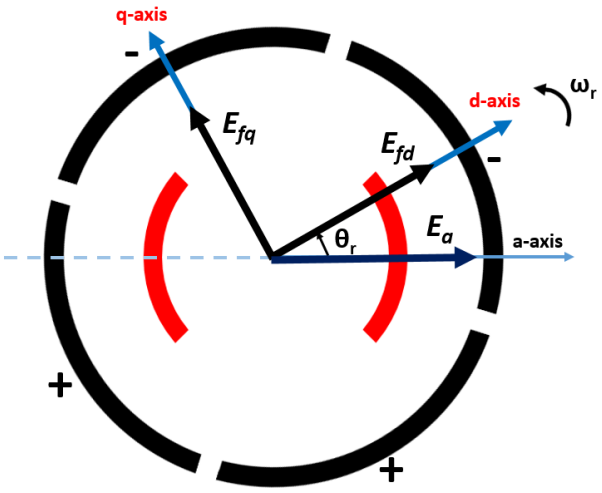

Fig. 3.10: ESG with double field circuit.

$$C_{Mfd-a} = C_{Md}\cos\theta_r \tag{3.53}$$

$$C_{Mfd-b} = C_{Md}\cos(\theta_r - 2\pi/3) \tag{3.54}$$

$$C_{Mfd-c} = C_{Md}\cos(\theta_r + 2\pi/3) \tag{3.55}$$

And for the mutual capacitance between the rotor and the stator plates along the q-axis are as follow:

$$C_{Mfq-a} = -C_{Mq}\sin\theta_r \tag{3.56}$$

$$C_{Mfq-b} = -C_{Mq}\sin(\theta_r - 2\pi/3) \tag{3.57}$$

$$C_{Mfq-c} = -C_{Mq}\sin(\theta_r + 2\pi/3) \tag{3.58}$$

where

$$C_{Md} = \frac{\epsilon_o A_s}{d_{fd} - d_s} \tag{3.59}$$

and

$$C_{Mq} = \frac{\epsilon_o A_s}{d_{fq} - d_s} \tag{3.60}$$

And for the field self-capacitance:

$$C_{fd} = \frac{\epsilon_o A_f}{d_{fd}} \tag{3.61}$$

$$C_{fq} = \frac{\epsilon_o A_f}{d_{fq}} \tag{3.62}$$

The transformation of the capacitance matrices into dq coordinates are as follow:

$$[T_{dqo}][C_{ss}][T^{-1}{}_{dqo}] = \begin{bmatrix} \frac{3}{2}C_o & 0 & 0 \\ 0 & \frac{3}{2}C_o & 0 \\ 0 & 0 & 0 \end{bmatrix} \tag{3.63}$$

$$[T_{dqo}][C_{rs}(\theta_r)] = \begin{bmatrix} C_{Md} & 0 \\ 0 & C_{Mq} \\ 0 & 0 \end{bmatrix} \tag{3.64}$$

As has been done before, defining a new stator capacitance in the *d*- and *q*-axis as follow:

$$C_d = C_q = \frac{3}{2}C_o \tag{3.65}$$

The electric charge in the *d*- and *q*-axis are as follow:

$$Q_d = -C_d V_d + C_{Md}(V_{fd} - V_d) \tag{3.66}$$

$$Q_q = -C_q V_q + C_{Mq}(V_{fq} - V_q) \tag{3.67}$$

Writing the *d*- and *q*-axis stator currents using (3.47) but with the redefined stator charges in (3.66) and (3.67):

$$I_d = -\frac{V_d}{r_s} + \omega_r C_q V_q - \omega_r C_{Mq}(V_{fq} - V_q) - C_d \frac{d}{dt}V_d + C_{Md}\frac{d}{dt}(V_{fd} - V_d) \tag{3.68}$$

$$I_q = -\frac{V_q}{r_s} - \omega_r C_d V_d + \omega_r C_{Md}(V_{fd} - V_d) - C_q \frac{d}{dt}V_q + C_{Mq}\frac{d}{dt}(V_{fq} - V_q) \tag{3.69}$$

The circuit representation of the above mentioned equations are shown in Fig. 3.11.

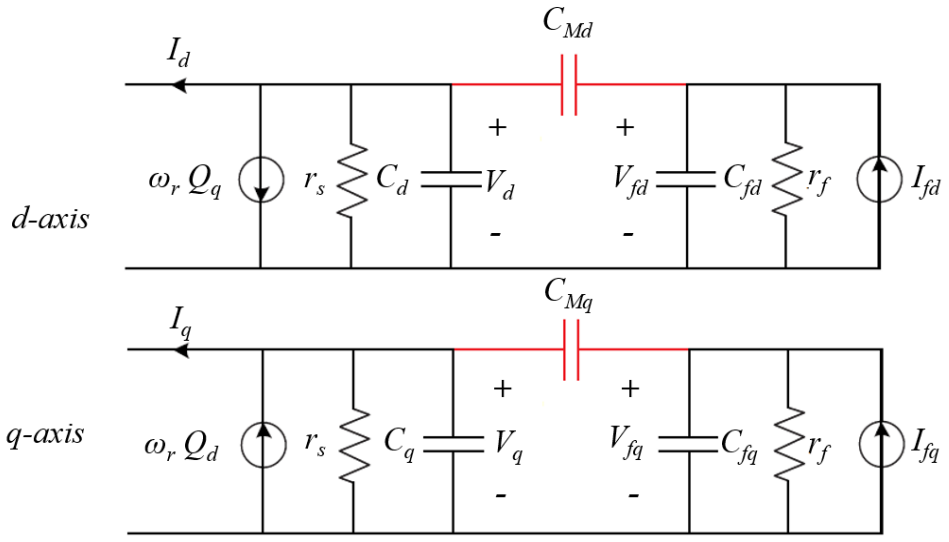

Fig. 3.11: *dq* representation of double field ESG.

Now, the simplification of the *dq* model shown in Fig. 3.11 can be achieved by rearranging (3.68) and (3.69) and taking into consideration that the field voltages in *d*- and *q*-axis are constants and thus their derivatives will be null, the stator current equations become:

$$I_d = -\frac{V_d}{r_s} + \omega_r(C_q + C_{Mq})V_q - \omega_r C_{Mq} V_{fq} - (C_d + C_{Md})\frac{d}{dt}V_d \tag{3.70}$$

$$I_q = -\frac{V_q}{r_s} - \omega_r(C_d + C_{Md})V_d + \omega_r C_{Md} V_{fd} - (C_q + C_{Mq})\frac{d}{dt}V_q \tag{3.71}$$

The circuit representation of (3.70) and (3.71) is shown in Fig. 3.12.

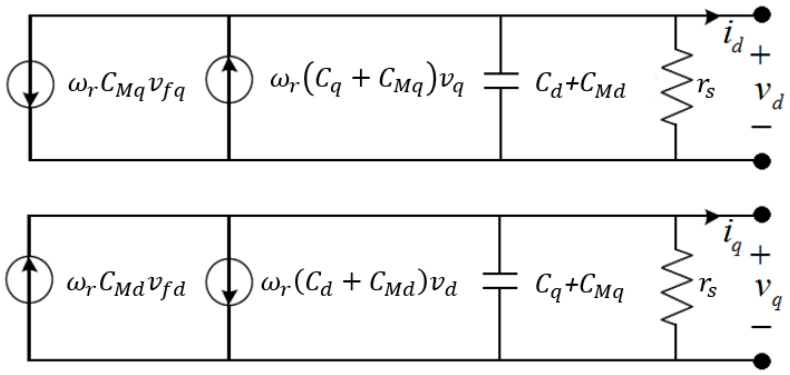

Fig. 3.12: Simplified *dq* circuit representation of ESG with double field circuits.

3.5 Equivalence between the inverter small-signal model and the ESG *dq* circuit

This work aims to promote a novel modeling approach of power inverters based on the electrostatic synchronous machine concept. If an equivalent machine model is implemented, large and small signal stability of single machine connected to infinite bus and multi-machine modeling approach can be easily implemented to analyze the stability of any microgrid with inverter-based distributed generators [83].

An intrinsic duality is founded between the ESG and the VSI with its inductive filter shown in Fig. 3.13. In ESG, the power transfer is due to charge transfer and, consequently,

a capacitive structure in a parallel configuration is expected. The control feedback network acts on the field voltage magnitude to control the output voltages. On the other side, in the power inverter the power transfer is achieved by the power switches. The duty cycle of switches is properly adjusted to control the output power. The rotor speed of the virtual ESG is the operating frequency of the power inverter. An inductive AC side circuit is expected [83].

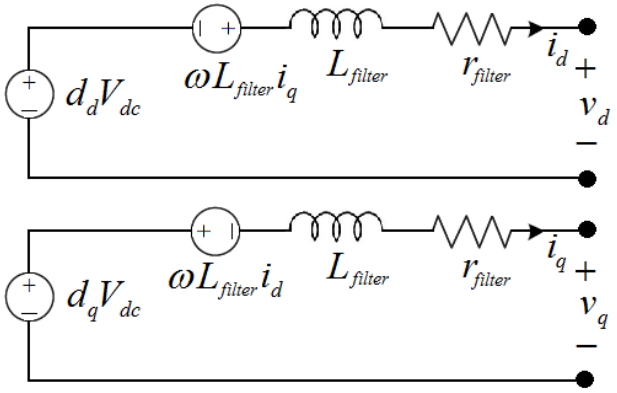

Fig. 3.13: Small-signal model of the power inverter with L-filter in the *dq* reference frame [83].

The duality is kept in the modeling approach. The machine stator circuit is expected to be the dual of the power inverter model. The modeling approach reinforces the intrinsic duality. The inverter based DG can be modelled by a dual circuit representing a virtual electrostatic synchronous generator. Because of the duality, the output power perfectly match and therefore the swing equation can be exploited in parallel with the steady state equivalent model derived in [82] to analyze the stability of microgrids with inverter-based DGs [46].

As long as the duality is concerned, the homogeneity of the network should be carefully addressed. The proposed modeling approach can be successfully applied in homogeneous microgrids. If several inverter-based DGs are interconnected, each DG can be replaced by its dual equivalent machine small signal model and thus the analysis of the whole network can be carried out.

Since a duality concept is applied, voltage signals of the machine model match the current signals of the power inverter and vice versa. Consequently, according to the conventional principle of duality, the duality equations should be considered in terms of numerical values and not measurement units. Duality equations are given by:

$$\begin{aligned} \omega_r &= \omega \\ v_{fq} &= -\frac{d_d V_{dc}}{\omega_r C_M} \\ v_{fd} &= \frac{d_q V_{dc}}{\omega_r C_M} \\ C + C_M &= L_{filter} \\ r_s &= \frac{1}{r_{filter}} \end{aligned} \tag{3.72}$$

According to the previous discussion, the electrical power and torque can be simply derived based on (3.47) such that:

$$P_t = \frac{3}{2}\left(V_d I_d + V_q I_q\right) + \frac{1}{3} V_0 I_0 \tag{3.73}$$

where the *0*-channel is null in (3.73). The *d*- and *q*-axis currents can be obtained from (3.47) and they can be rewritten in the following form for convenience:

$$\begin{aligned} I_d &= \frac{d}{dt} Q_d - Q_q \omega_r - \frac{V_d}{r_s} \\ I_q &= \frac{d}{dt} Q_q + Q_d \omega_r - \frac{V_q}{r_s} \end{aligned} \tag{3.74}$$

where Q_d and Q_q are the stator charges for the double-field ESG. The expression of the power transferred from the rotor to the stator of the ESG is then:

$$P_t = \frac{3}{2}\left[\left(V_d \frac{d}{dt} Q_d + V_q \frac{d}{dt} Q_q\right) + \left(V_q Q_d - V_d Q_q\right)\omega_r - \left(\frac{V_d^2}{r_s} + \frac{V_q^2}{r_s}\right)\right] \tag{3.75}$$

The first term in (3.75) represents the rate of change of the stator electric energy (transformer action), the second term represents the power transferred from the rotor to the stator P_e (motion action). Finally, the last term represents the power losses in the ESG. Now the virtual air-gap torque T_e can be simply obtained from the second term of (3.75) after dividing P_e by the rotor speed ω_r as follow:

$$T_e = \frac{3}{2}\left[V_q Q_d - V_d Q_q\right] \tag{3.76}$$

The swing equation of traditional SGs can be exploited for ESGs. After transforming all the model parameters into pu system, the equivalence between the kinetic energy of conventional SGs and the stored energy in the mutual capacitance of ESG can be founded. The droop control filter is used to determine the inertial and the damping of ESG [46].

3.6 Performance comparison between the VSI *dq* equivalent circuit and the ESG model

In the simulation setup, the small signal model of the power inverter shown in Fig. 3.13 and the *dq* equivalent model of the ESG shown in Fig. 3.12 are implemented. *abc* to *dq0* transformation is applied to the duty cycle signals d_a, d_b and d_c generated by the PWM comparator and thus generating d_d and d_q signals. Duty cycle signals in the *dq* reference frame feeds the *dq* equivalent models of both the inverter and the ESG. Voltage signals of the ESG (V_d and V_q) are compared to current signals I_d and I_q of the small-signal power inverter model. As shown by simulation results, matching between ESG voltage signals and inverter current signals is achieved and thus validating the proposed modeling approach. It should be mentioned that a negative reactive power is expected for the ESG model. During the simulation; the ESG output reactive power has been inverted to illustrate the equivalence between both models.

The configuration of the microgrid system used in this test has two buses as shown in Fig. 3.14. The system and the inverter parameters are the same one used in chapter 2 and listed in Table 2.2. The 20 kVA three-phase VSI is feeding a constant local load (Load 1) of 5 kW. Load 2 is variable and it is connected to the inverter through a distribution line.

The simulation are carried out with two different cases as described below:

- The first case: from **0-0.2** seconds

The inverter in operating under stand-alone mode with Load 1 = 5 kW and Load 2 = 5 kW.

- The second case: from **0.35-0.7** seconds

  The inverter in operating under stand-alone mode with Load 1 = 5 kW and Load 2 = 15 kW.

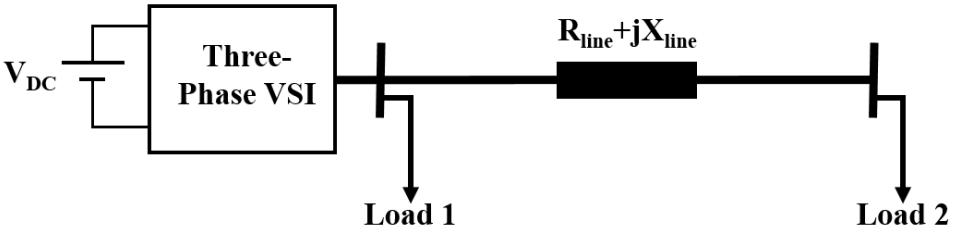

Fig. 3.14: LV Islanded microgrid test system.

Fig. 3.15 shows the output average power of the small signal model of the power inverter and the *dq* equivalent model of the ESG. The output reactive power of the small signal model of the inverter and the *dq* equivalent model of the ESG is shown in Fig. 3.16.

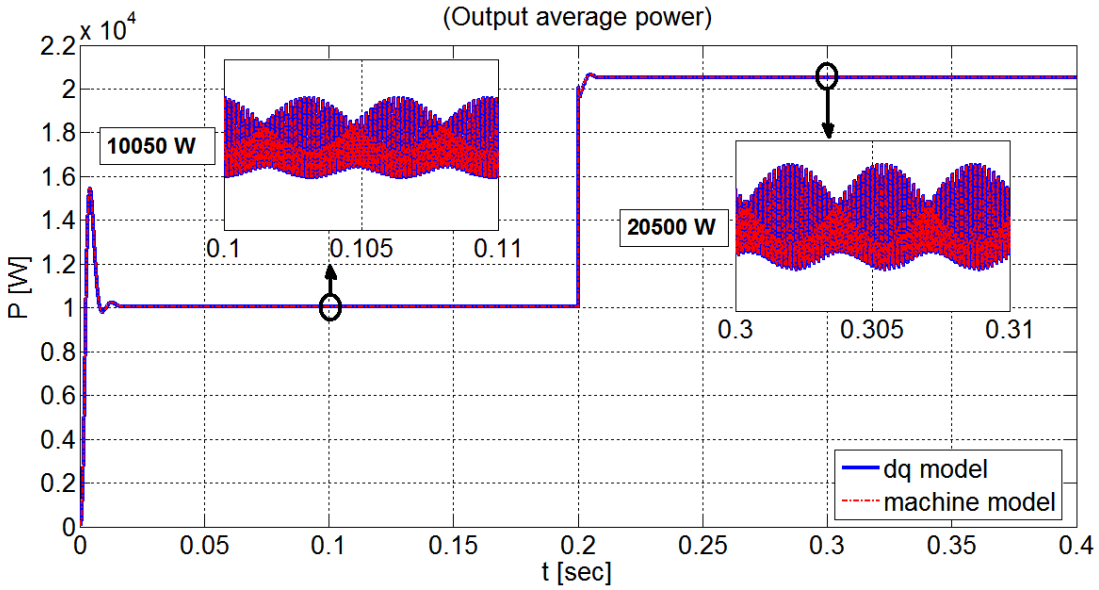

Fig. 3.15: Output average power of the small signal model of the inverter and the *dq* equivalent circuit of the ESG.

From 0 to 0.2 second in Fig. 3.15, the inverter and the ESG are feeding a constant local load of 5 kW and another load of 5 kW connected to the inverter through a

distribution line. The net load power demand in this case is 10 kW. The overshoot and settling time of the output power of the inverter are acceptable.

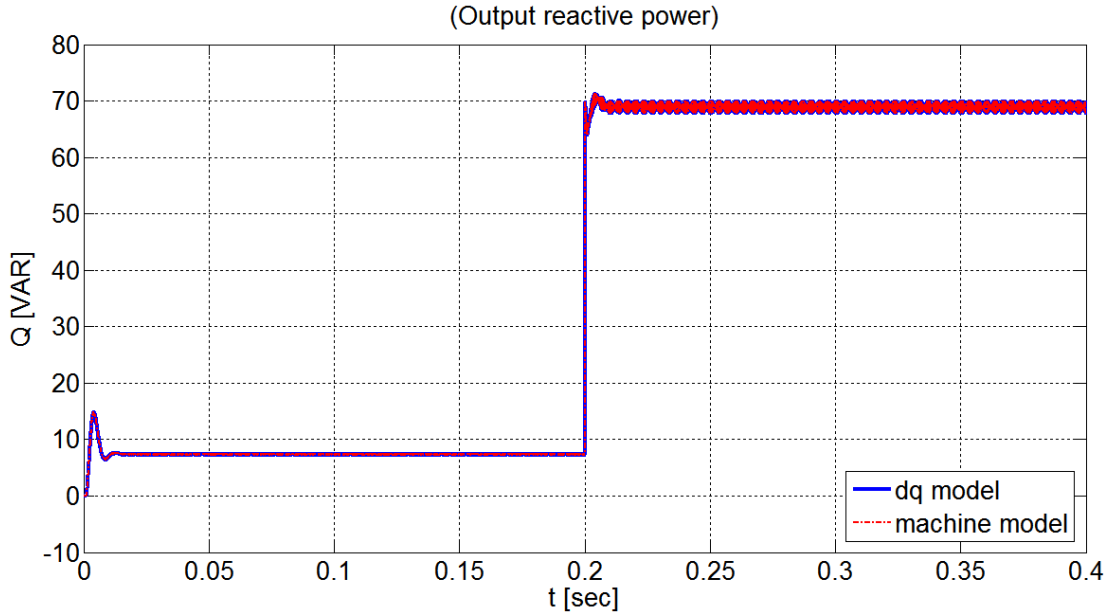

Fig. 3.16: Output reactive power of the small signal model of the inverter and the *dq* equivalent circuit of the ESG.

After increasing load 2 to 15 kW (from 0.2-0.4 seconds), the output power of the inverter has been increased as the total demanded power by the loads in this case is equal to 20 kW. In both cases, the VSI output power is slightly greater than the demanded power because of the power losses in the distribution line. Before 0.2 seconds, the power losses in the distribution line is around 50 W and after that, the power losses has been increased to 500 W. the output power of the VSI is 2.5% greater than its nominal power (20 kVA). This should be taken into account when choosing the power ratings of the IGBTs of the power inverter. A perfect matching between the output average and reactive power of both models is achieved.

It should be mentioned that the output reactive power shown in Fig. 3.16 is very small compared with the average power since both loads are resistive loads and all the reactive power is being consumed by the distribution line reactance X_{Line}.

Fig. 3.17 shows a comparison between the ESG *d*-axis voltage signal V_d and the inverter small signal *d*-axis current signal I_d. The comparison between the ESG *q*-axis voltage signal V_q and the inverter small signal *q*-axis current signal I_q is shown in Fig. 3.18. Simulated waveforms perfectly overlap thus validating the proposed modeling approach which based on the duality concept.

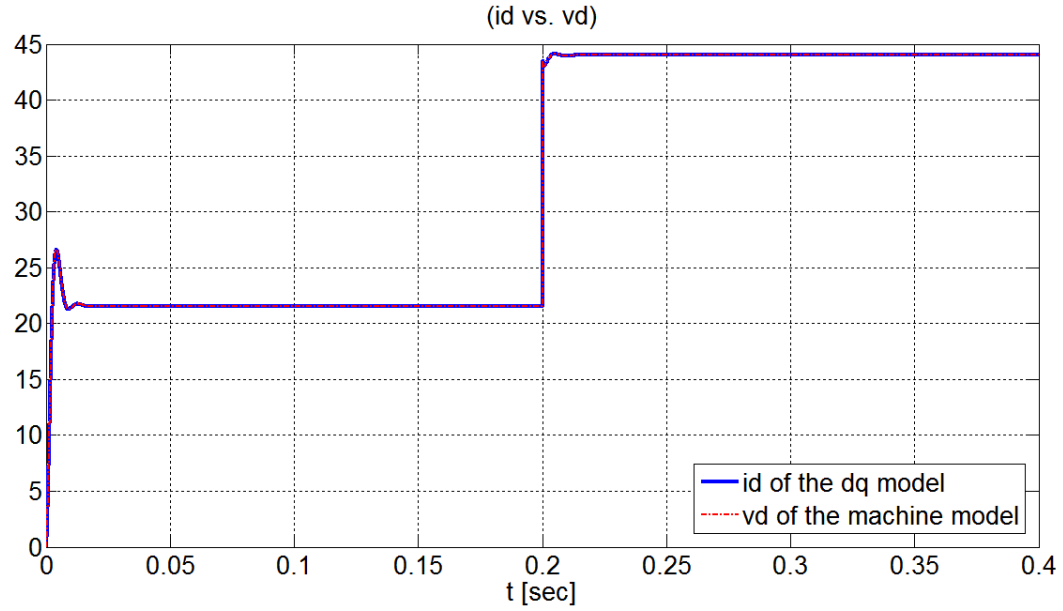

Fig. 3.17: A comparison of simulated waveforms of *d*-axis components of the small signal model of both the ESG and the power inverter.

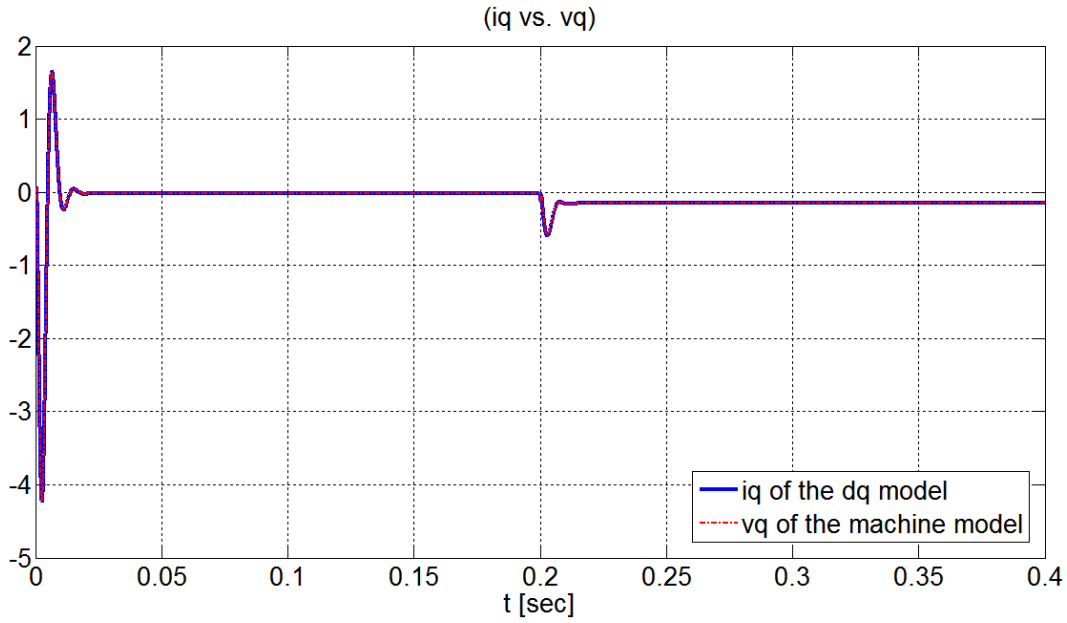

Fig. 3.18: A comparison of simulated waveforms of *q*-axis components of the small signal model of both the ESG and the power inverter.

Finally, the output frequency of the small signal model of the inverter and the *dq* equivalent model of the ESG is shown in Fig. 3.19.

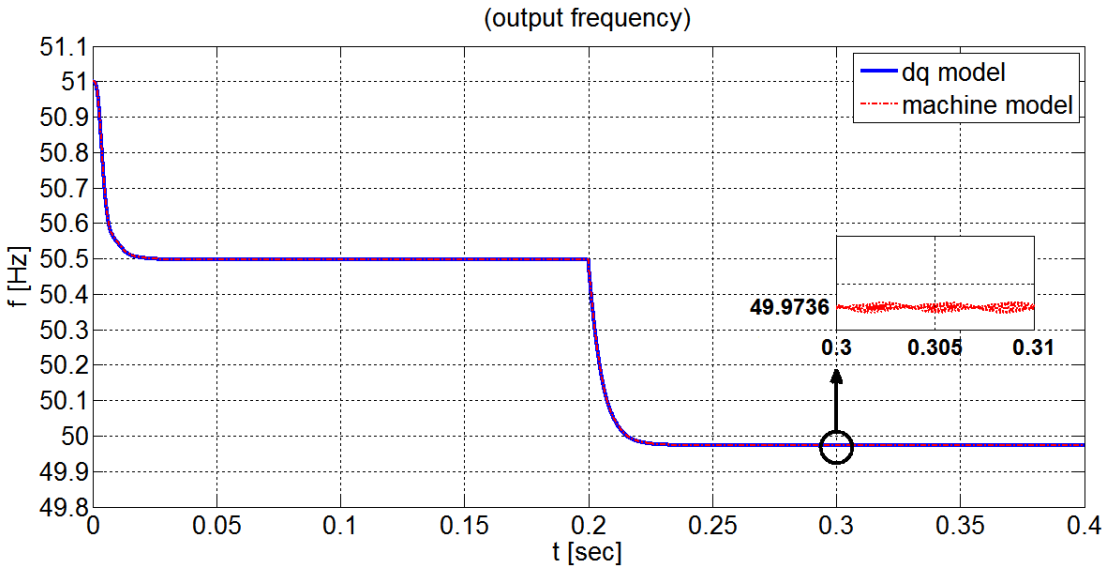

Fig. 3.19: Output frequency of ESG and the power inverter models.

As seen from Fig. 3.19, the no-load frequency of the inverter and the ESG is 51 Hz, which is the initial frequency the inverter will start from. From 0 to 0.2 seconds, the inverter and the ESG are feeding two loads with total demanded power of 10 kW. According to the *P vs. f* droop controller, this power is corresponding to an output frequency of 50.5 Hz which match thee actual output frequency of the inverter and the ESG.

The *P vs. f* droop controller has been designed to deliver the nominal power (20 kW) at rated frequency (50 Hz). As seen from Fig. 3.19, and after 0.2 seconds, and as Load 2 has been increased to 15 kW, total demanded power by the loads increased to 20 kW. This power is corresponding to an output frequency of 50 Hz. the output frequency of the inverter has been decreased to 49.973 Hz as expected from the droop controller.

The reason why the output power of the inverter is not accurately 50 Hz is because of the power losses in the distribution line which has been considered as load to the power inverter. An offset power can be added to the droop controller in order to compensate for

the power losses in the distribution line but this requires to know accurately the parameters of the distribution line which is practically difficult.

3.7 Steady-state equivalent circuit of ESG

The steady-state model of the ESG can be obtained by eliminating all the time derivative terms from (3.70) and (3.71), where all the stator and the rotor quantities are constants. Assuming balanced steady-state conditions, the stator current equations become:

$$I_d = -\frac{V_d}{r_s} + \omega_r(C_q + C_{Mq})V_q - \omega_r C_{Mq} V_{fq} \tag{3.77}$$

$$I_q = -\frac{V_q}{r_s} - \omega_r(C_d + C_{Md})V_d + \omega_r C_{Md} V_{fd} \tag{3.78}$$

The field voltage ($\boldsymbol{V_f}$), the stator voltage ($\boldsymbol{V_t}$) and the stator current ($\boldsymbol{I_t}$) can be written in phasor form as follow:

$$\begin{aligned} \boldsymbol{V_f} &= V_{fd} + jV_{fq} \\ \boldsymbol{V_t} &= V_d + jV_q \\ \boldsymbol{I_t} &= I_d + jI_q \end{aligned} \tag{3.79}$$

Assume C_d=C_q=C_s and C_{Md}=C_{Mq}=C_M, starting from the stator current $\boldsymbol{I_t}$ by combining (3.77) and (3.78) and replacing each term $1/(\omega_r C)$ by its corresponding reactance X_C, then:

$$\boldsymbol{I_t} = \frac{\boldsymbol{V_f}}{-jX_{CM}} - \frac{\boldsymbol{V_t}}{-j(X_{Cs} + X_{CM})} - \frac{\boldsymbol{V_t}}{r_s} \tag{3.80}$$

The steady-state equivalent circuit is shown in Fig. 3.20.

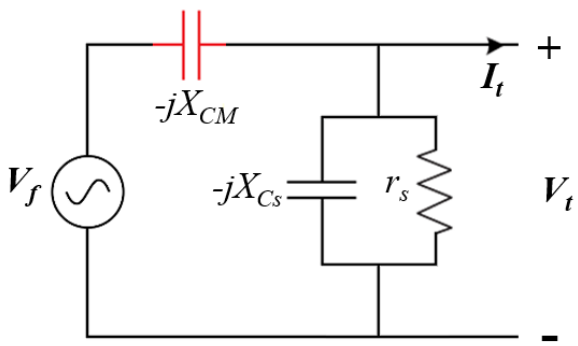

Fig. 3.20: Steady-State Equivalent circuit of ESG.

According to (3.72), the field voltage can be written as follow:

$$\boldsymbol{V_f} = \frac{V_{dc}}{\omega_r C_M}\left(d_q - jd_d\right) \tag{3.81}$$

The system configuration for analyzing the performance of the steady-state model of ESG is the same one shown in Fig. 3.14. The inverter in operating under stand-alone mode with Load 1 = 5 kW and Load 2 = 5 kW. Table 3.1 lists the simulation parameters used for the test.

Table 3.1: Simulation parameters of the steady-state model of the ESG.

Parameter	Value
V_{dc}	900 V
ω_r	317.3 rad/sec
r_s	2 Ω
C_M	$0.8*10^{-3}$ F
C_s	$0.8*10^{-3}$ F
d_d	0.095
d_q	0.28
P_{Load1}	5 kW
P_{Load2}	5 kW

It should be mentioned that the steady-state model of the ESG doesn't take into account the voltage controller dynamics. The *d* and *q* components of the modulation index, d_d and d_q, have been considered constant in this case, and their steady-state values (listed in Table 3.1) were obtained from the first simulation case in the previous section.

The following figures show the performance comparison of the steady-state model of the ESG and the small-signal model of the VSI (shown in Fig. 3.13).

As shown in Fig. 3.21 and Fig. 3.22, during the steady-state, the output average and reactive power perfectly match and the small signal model of the inverter (as well as the *dq* model of the ESG) covers the dynamics of the VSI during the transients while the steady-state model of the ESG doesn't.

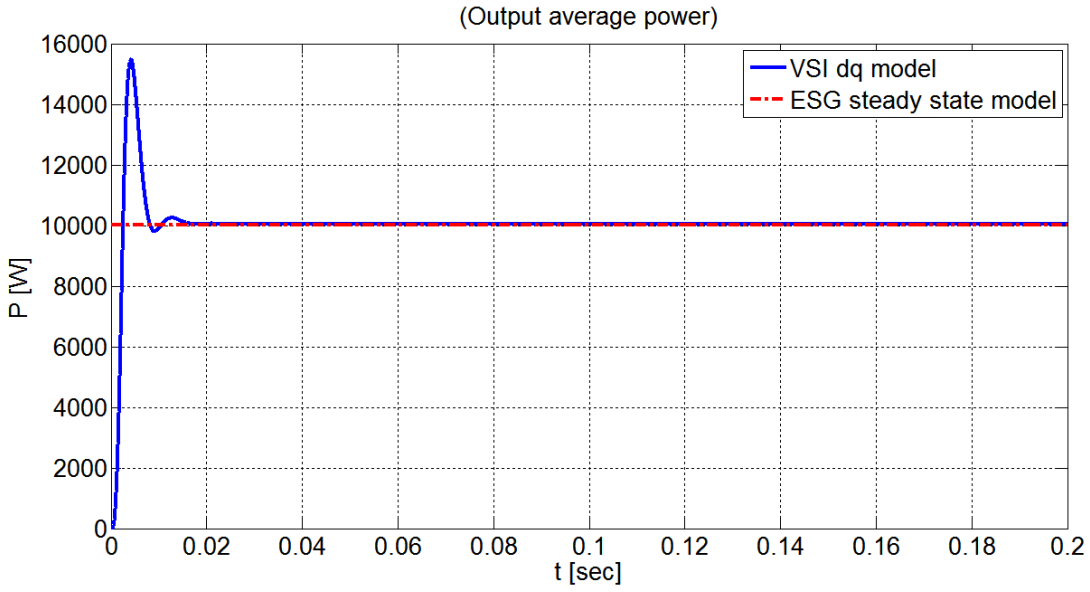

Fig. 3.21: Output average power of the small signal model of the inverter and the steady-state model of the ESG.

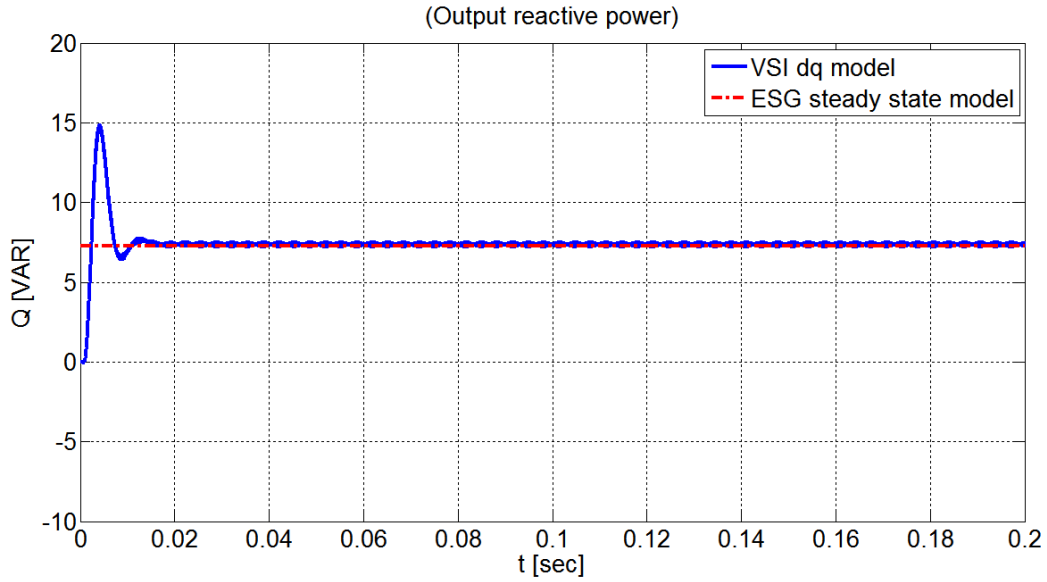

Fig. 3.22: Output reactive power of the small signal model of the inverter and the steady-state model of the ESG.

Fig. 3.23 shows a comparison between the ESG steady-state model *d*-axis voltage signal V_d and the inverter small signal *d*-axis current signal I_d. The comparison between the ESG steady-state model *q*-axis voltage signal V_q and the inverter small signal *q*-axis current signal I_q is shown in Fig. 3.24.

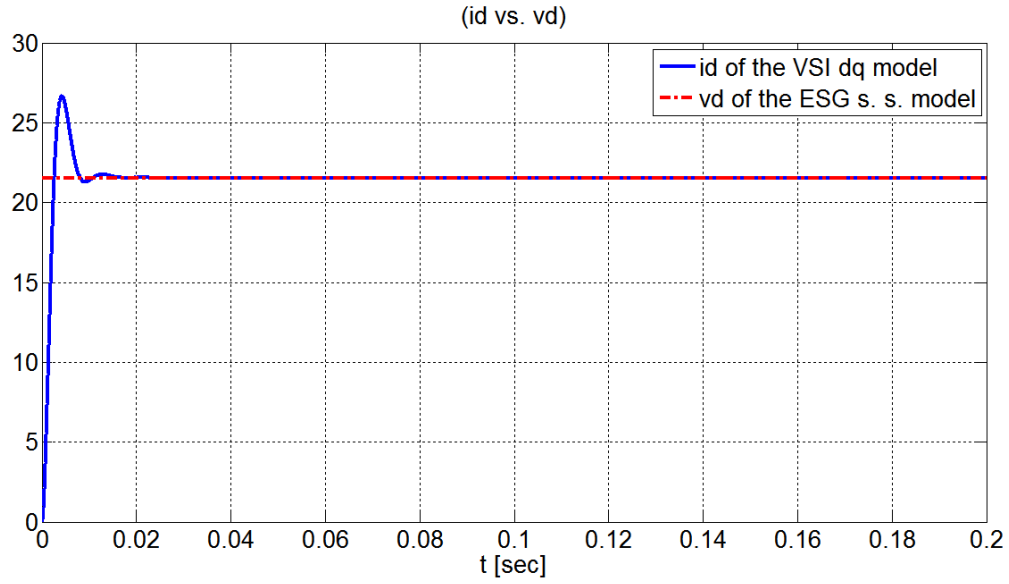

Fig. 3.23: A comparison of simulated waveforms of *d*-axis components of the small signal model of the inverter and the steady-state model of the ESG.

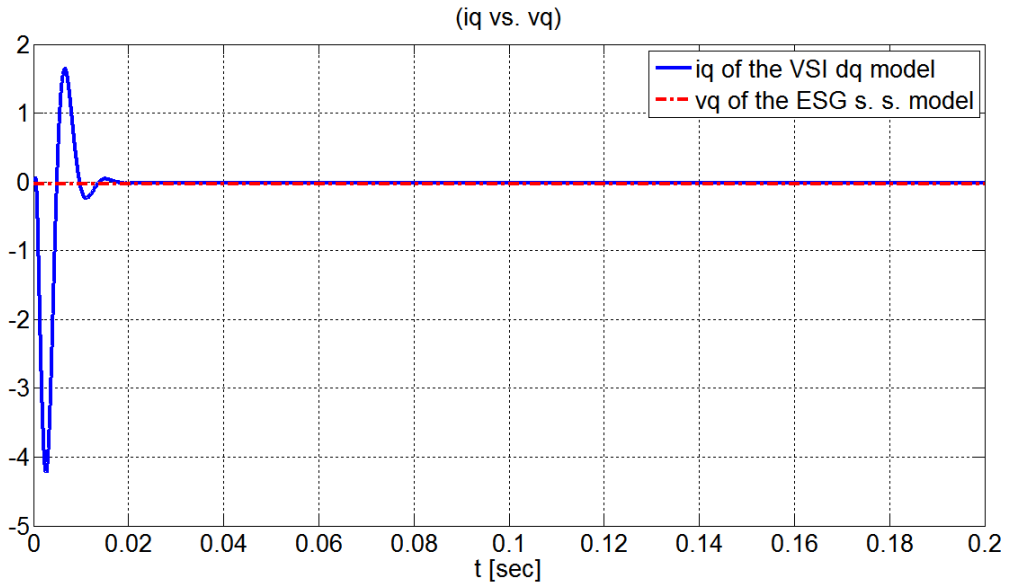

Fig. 3.24: A comparison of simulated waveforms of *q*-axis components of the small signal model of the inverter and the steady-state model of the ESG.

It is clear from Fig. 3.23 and Fig. 3.24 that the simulated waveforms in steady-state perfectly overlap thus validating the proposed modeling approach.

In this chapter, a modeling approach of an inverter-based distributed generator based on the concept of electrostatic synchronous machine has been presented. In multiple Inverter-Based DGs microgrid, each DG can be replaced by its dual equivalent machine

thus the analysis of the whole network can be carried out. Parameters of the equivalent machine model have been derived on the basis of duality equations. Consequently, power matching is achieved allowing the analysis of the microgrid stability by exploiting the swing equation of the virtual ESG.

By applying an outer power control loop to the Inverter-Based generator, the model parameters which describe the inertial and damping values of the DG can be easily determined. As shown by simulation results, matching has been achieved, thus validating the modeling approach.

Chapter 4 Nonlinear droop Control of VSI DGs in LV Islanded Microgrids

This chapter focuses on the parallel operation of VSI DGs in LV islanded microgrids. An improved primary regulation method with a new implementation technique is proposed for Inverter-Based distributed generators. A droop control method with changing slope under frequency constrained operation, is proposed as a new primary regulation driven by minimum losses Optimal Power Flow (OPF) for microgrids. It is well known that power flow can provide infinite solutions if the generators have not fixed output. Optimal power flow solves this problem providing a unique solution for each loading condition. Such unique solution, when loads and lines are modelled as frequency dependent components also comprises the operating frequency. With the new implementation technique, an off-line minimum losses OPF has been utilized to extract a lookup table for the composition of the droop curves with plug-and-play functionality. The following sections show different case studies with the implementation of the proposed technique.

4.1 Configuration of the Low-Voltage Islanded Microgrid under test

In order to analyze the effect of the new primary regulation method on the power sharing and the operating frequency of the distributed generators, a LV islanded microgrid test system has been developed, consisting of four buses with two Inverter-Based DGs feeding two loads located at different buses as shown in Fig. 4.1. The system has three symmetrical distribution lines with *R/X* ratio equals to 7.7 as listed in Table 4.1.

The first VSI (DG_1) has a maximum power capacity of 30 kVA, while the second VSI (DG_2) has a maximum power capacity of 20 kVA and both DGs has a minimum power factor of 0.8.

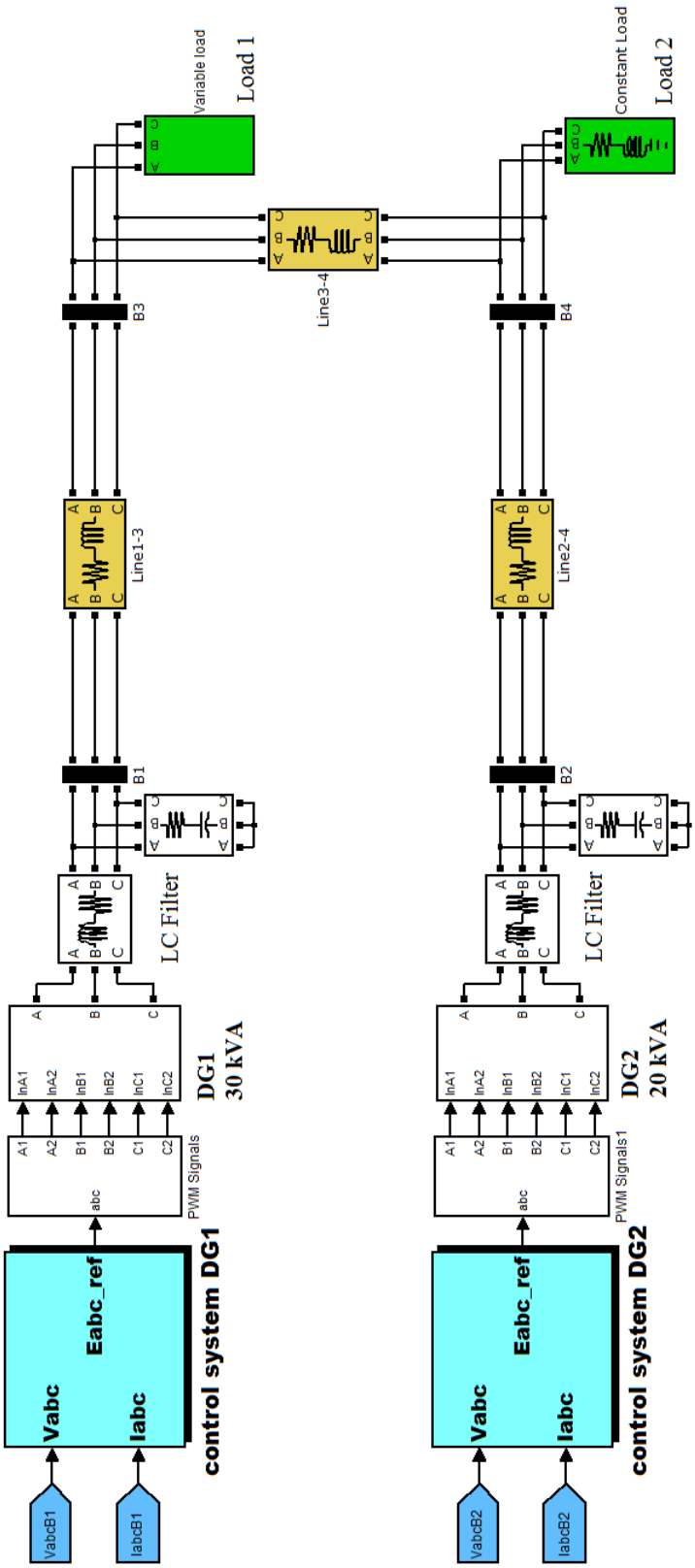

Fig. 4.1: LV microgrid test system.

Table 4.1: Electric features of 4-Bus system

Branch	R (pu)	X (pu)	R/X	I_{max} (pu)
1-3	0.22229917	0.02873961	7.7	0.5396
2-4	0.22229917	0.02873961	7.7	0.5396
3-4	0.22229917	0.02873961	7.7	0.5396

VA_{Base}=100 kVA; $V_{L\text{-}L\ Base}$=380 V, Z_{Base}=1.444 Ω, f_{Base}=50 Hz.

The next section explain the construction of the *P vs. f* and *Q vs. V* droop control of the three-phase VSI DGs which are working in parallel on the same microgrid.

4.2 Construction of the Droop Curves

After the power ratings of each DG have been specified, the slope of the droop curves can be easily designed after setting the frequency and voltage constraints. For this particular islanded microgrid; the frequency must be within ±0.02 pu, or ±1 Hz of 50 Hz and the voltage must be within ±0.04 pu or ±8.776 V_{rms}.

In order to ensure the stability of the system and forcing DG_1 and DG_2 to operate with the same frequency in steady state, both DGs should have the same no-load frequency and voltage, i.e. they should have the same f_{max} and V_{max} as shown in Fig. 4.2. Moreover, the droop controllers should be designed in such a way that the output power does not exceed the ratings of DG_1 and DG_2 and ensuring that each DG is sharing power in the microgrid proportionally to the rated power of each DG unit. This can be accomplished using the following equation [60]:

$$m_{P1}P_{DG1} = m_{P2}P_{DG2} \tag{4.1}$$

where m_{P1} and m_{P2} are the slopes of the *P vs. f* curves of the DG_1 and DG_2, respectively. The same can be applied for *Q vs. V* for both DGs as follow:

$$n_{Q1}Q_{DG1} = n_{Q2}Q_{DG2} \tag{4.2}$$

where n_{Q1} and n_{Q2} are the slopes of the *Q vs. V* curves of the DG_1 and DG_2, respectively.

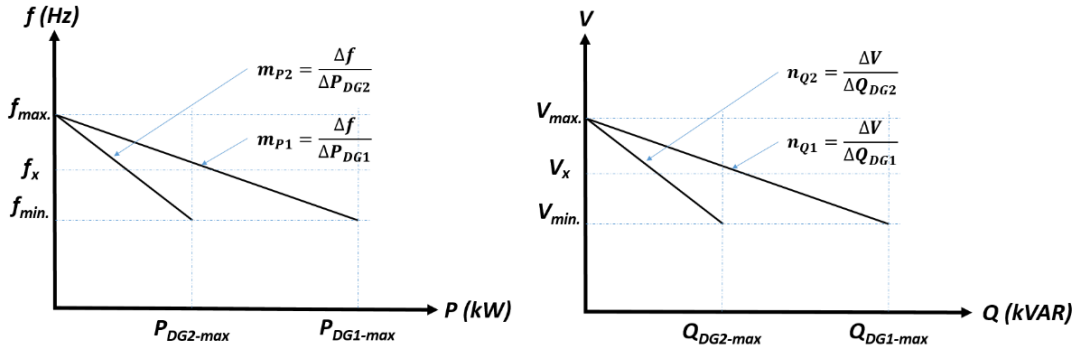

Fig. 4.2: Droop curves of DG_1 and DG_2.

As listed in Table 4.1, the LV microgrid under test has *R/X* ratio equals to 7.7, which means that the distribution line impedance is mainly resistive. Thus *P vs. f* and *Q vs. V* droops can be used for LV microgrids but the coupling between P and Q will be significant [8], [20]. This coupling can be terminated by using Virtual Impedance technique [84]–[87] or adopting *P vs. V* and *Q vs. f* droops [88]. In this thesis, *P vs. f* and *Q vs. V* droops have been used without discussing the coupling issue.

If the maximum output average power of DG_1 and DG_2 has been considered as 30 kW and 20 kW, respectively; then the maximum output reactive power of each DG can be easily calculated by taking into account that the minimum power factor of each DG is 0.8, then:

$$Q_{DG1,max} = \sqrt{\left(S_{1,max}\right)^2 - \left(PF_{min} * P_{DG1,max}\right)^2} \tag{4.3}$$

and for DG_2:

$$Q_{DG2,max} = \sqrt{\left(S_{2,max}\right)^2 - \left(PF_{min} * P_{DG2,max}\right)^2} \tag{4.4}$$

where $S_{1,max}$ and $S_{2,max}$ is the maximum apparent power of DG_1 and DG_2, respectively. PF_{min} is the minimum Power Factor of each inverter. So, $Q_{DG1,max}$ and $Q_{DG2,max}$ are 18 kVAR and 12 kVAR, respectively.

The droop curves slopes m_{P1} and n_{Q1} for the first inverter, DG1, are as follow:

$$m_{P1} = \frac{\Delta f}{\Delta P_{DG1}} = -\frac{2}{30 * 10^3} = -6.7 * 10^{-5}\, Hz/W \quad (4.5)$$

$$n_{Q1} = \frac{\Delta V}{\Delta Q_{DG1}} = -\frac{24.8215}{18 * 10^3} = -1.379 * 10^{-3}\, V/VAR \quad (4.6)$$

and those for the second inverter, DG2, are as follow:

$$m_{P2} = \frac{\Delta f}{\Delta P_{DG2}} = -\frac{2}{20 * 10^3} = -1 * 10^{-4}\, Hz/W \quad (4.7)$$

$$n_{Q2} = \frac{\Delta V}{\Delta Q_{DG2}} = -\frac{24.8215}{12 * 10^3} = -2.068 * 10^{-3}\, V/VAR \quad (4.8)$$

The aforementioned equations of the conventional droop control of Inverter-Based DGs and its performance will be compared with the new regulation method in terms of minimum distribution lines power losses.

4.3 Nonlinear Droop control for minimum power losses

As explained in the previous sections in standard linear droop control method, the active power variation of generators always stays proportional to its rated power. As shown in Fig. 4.2, the variation of load leads to a slight change of the operating frequency f_x and the system regain the stability at the new operating frequency. The conventional linear droop control is very simple and reliable, but conventional droop control cannot provide optimized operating points to minimize the power losses in distribution lines.

A nonlinear droop control is proposed for inverter-based DGs in islanded microgrids, which is an expansion of the linear droop control. DG_1 in Fig. 4.1 will use the nonlinear droop control or modified droop control while DG_2 will be controlled by the conventional droop control. The active power droop slope m_{P1} of DG_1 which is chosen optimally according to the limitations of output power and frequency will run in the range [m_{P1_min}; m_{P1_max}].

The OPF finds for each loading condition a minimum loss operating state, or the optimized m_{P1}. The minimum loss operating state comprising system's frequency and the droop parameters. The constraints of the OPF is as follow [89]–[91]:

$$\begin{gathered} P_{DG1} + P_{DG2} = P_{L1} + P_{L2} + \sum P_{Loss} \\ m_{P1\_min} \le m_{P1} \le m_{P1\_max} \\ P_{DG1\_min} \le P_{DG1} \le P_{DG1\_max} \\ f_{min} \le f \le f_{max} \\ I_{Line} \le I_{Line\_max} \end{gathered} \tag{4.9}$$

where P_{L1} and P_{L2} are the loads at Bus 3 and 4, respectively. P_{Loss} is the power losses in the distribution lines, m_{P1_min} and m_{P1_max} are the minimum and maximum droop coefficient for *P vs. f* of DG_1, respectively. P_{DG1_min} and P_{DG1_max} are the minimum and maximum output power of DG_1, respectively. I_{Line} and I_{Line_max} are the distribution line current and the maximum allowable distribution line current, respectively.

It should be mentioned that the OPF has been solved for frequency dependent loads [89], [90]. The modified droop curve is generated by changing the load at Bus 3 (Load 1) in the microgrid and assessing through the OPF the relevant value of m_{P1}, which is here considered as the only adjustable parameter producing a new power sharing among generators. The droop parameter of DG_2 m_{P2} is constant (Table 4.2) and the load at Bus 4 (Load 2) is constant as listed in appendix A and B. The range of the slope of the droop control *P vs. f* of DG_1 is:

$$-12.5 \times 10^{-5} \le m_{P1} \le -6.7 \times 10^{-5} \tag{4.10}$$

4.4 Case study

To analyze the effect of the controller parameters on the power sharing of generators, the system shown in Fig. 4.1 is considered. DG_1 has power supply capacity ranging from 0 to 30kW, DG_2 has power supply capacity ranging from 0 to 20kW. The performance of

the system under conventional droop control (parameters are listed in Table 4.2) will be compared with the performance of the same system under the modified nonlinear droop control (Optimized) and with the same loading conditions.

For this test microgrid, the load at bus 4 (Load 2) is constant and equal to 10 kW with 0.98 *PF*. The load at Bus 3 (Load 1) is considered to be variable and ranging from 10 kW to 24 kW with different power factors ranging from 0.85 to 0.98. The construction of the tables listed in Appendix A has been done by changing the active power of Load 1 by 2 kW at every step and considering different power factors (0.85, 0.90 and 0.98). The power, reactive power, frequency, voltage, current and power losses for the test system are listed in Appendix A.

Table 4.2: System and control parameters of Conventional Droop control

	DG1	**DG2**
$\mathbf{P_{max}}$ (kW)	30	20
$\mathbf{Q_{max}}$ (kVAR)	18	12
$\mathbf{f_{min}}$ (Hz)	49	49
$\mathbf{f_{max}}$ (Hz)	51	51
$\mathbf{V_{L\text{-}Lmin}}$ (V)	364.8	364.8
$\mathbf{V_{L\text{-}Lmax}}$ (V)	395.2	395.2
$\mathbf{m_P}$ (Hz/W)	$-6.7*10^{-5}$	-10^{-4}
$\mathbf{n_Q}$ (V/VAR)	$-1.379*10^{-3}$	$-2.068*10^{-3}$

The nonlinear droop curve is built by changing Load 1 at bus 3 in the same way of the conventional droop control and assessing through the OPF the relevant value m_{P1}. Here, only *P vs. f* curve of the DG_1 is being optimized while DG_2 is being controlled by the conventional droop control with constant slope ($m_{P2}= -10^{-4}$). The new value of m_{P1} is considered as the only adjustable parameter producing a new power sharing among DG_1 and DG_2. The power, reactive power, frequency, voltage, current and power losses for the proposed nonlinear droop control are listed in the tables found in Appendix B.

As shown from the results obtained from OPF, the power losses in the distribution lines have been reduced and meeting the frequency constraint for all cases. Moreover, the operating frequency of DG_1 and DG_2 are the same under all cases.

Next, time-domain simulation of the microgrid under test with a new implementation technique of the nonlinear droop control (with variable m_{PI}) is done in MATLAB/Simulink environment.

4.4.1 Time-Domain Simulation of the Case Study

By using MATLAB/Simulink environment; the LV microgrid has been built, as shown in Fig. 4.1. The idea of implementing the optimized slope of the *P vs. f* droop curve obtained from tables listed in Appendix B is shown in Fig. 4.3. A lookup table has been used instead of adopting on-line OPF analysis. This has the advantage of speeding up the simulation time and practically enhancing the transient response of the system.

The first column of the lookup table shown in Fig. 4.3 contains the output average power of DG_1 and the second column represent the corresponding output frequency for each loading condition with different power factors. The lookup table uses a linear interpolation method between points. Next subsection shows the simulation results of the proposed technique.

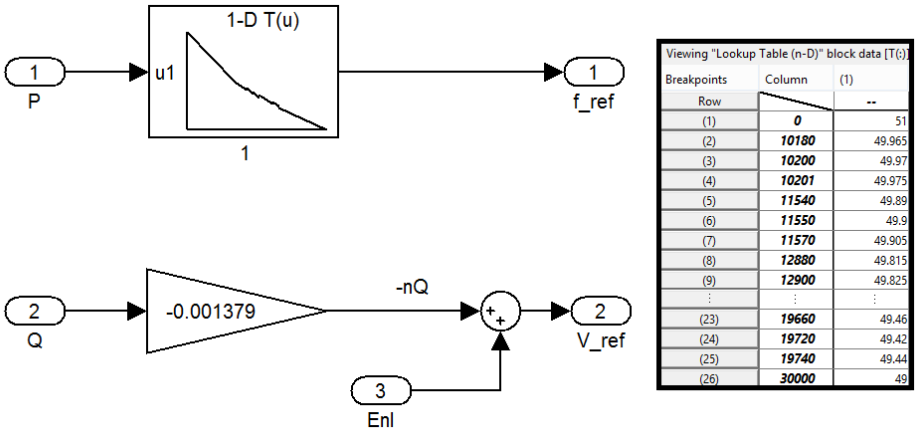

Fig. 4.3: Implementation of the Modified Droop controller of DG_1.

4.4.2 Performance verification under 0.85 *PF* of Load 1

Four different cases of Load 1 were considered for the LV microgrid under study. The first set of outputs has been obtained when Load 1 *PF* is 0.85 and setting the values of Load 1 as 12, 16, 20 and 24 kW consequently every 0.1 seconds.

The output average power at each bus for both the conventional droop control and the modified droop control are shown in Fig. 4.4 and Fig. 4.5, respectively. The output power matches the results listed in appendixes A and B. Moreover, the system presents a good and fast transient response for loads variation.

The first remark on the output power of the conventional and modified droop regulation is that the power at the load buses (Bus 3 and 4) are identical in both cases. The output power of DG_1 (at Bus 1) has been reduced in the case of using the modified droop regulation of DG_1 as a result of the optimization process. On the other hand, the output power of DG_2 (Bus 2) has been increased automatically in order to compensate for the reduction of the DG_1 output power.

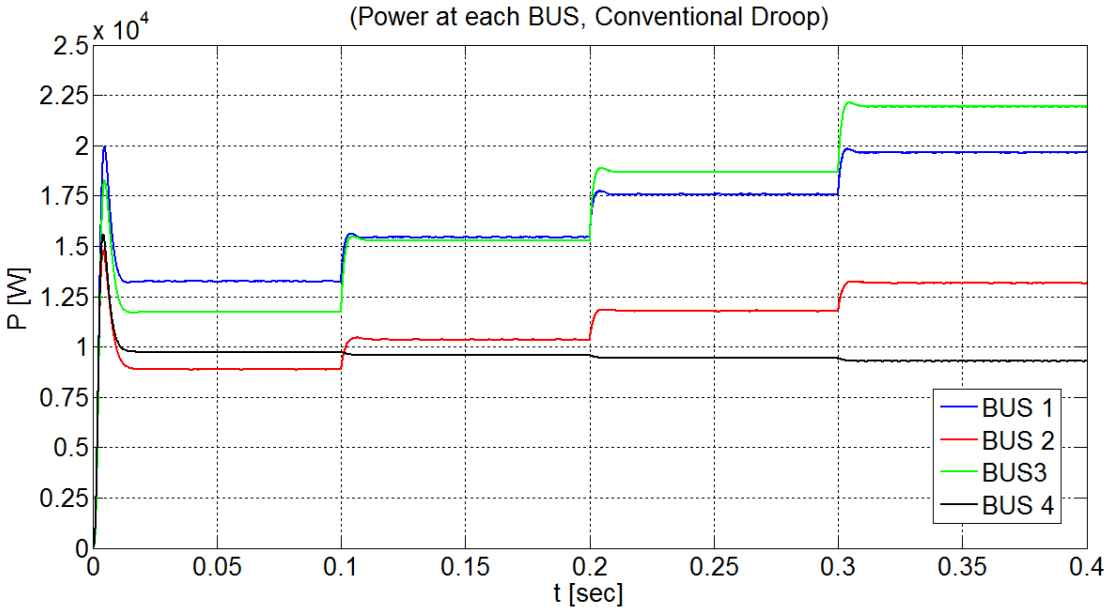

Fig. 4.4: Output average power at each bus of the conventional droop control (Load 1 *PF* = 0.85).

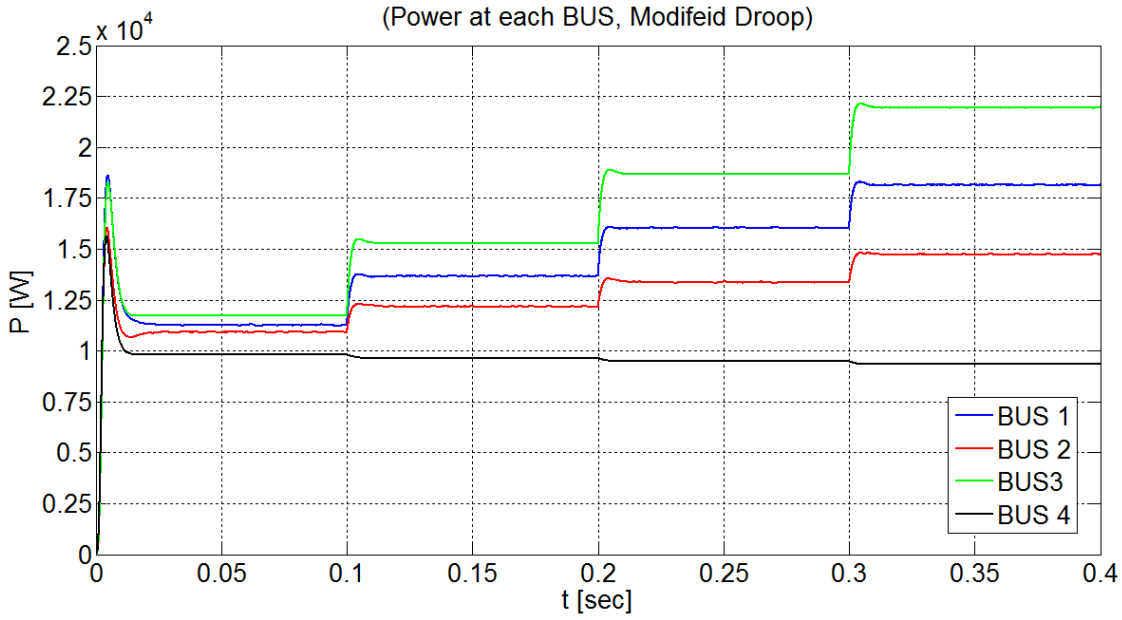

Fig. 4.5: Output average power at each bus of the Modified droop control (Load 1 *PF*=0.85).

Furthermore, it is obvious from Fig. 4.4 and Fig. 4.5 that the overshoot in the output power of DG_1 has been reduced as a result of using the modified droop regulation.

The objective of the work is to minimize the power losses at the distribution lines. Fig. 4.6 shows the power losses for both methods.

As expected, power losses have been reduced when using the modified droop control. It should be mentioned that the power ratings of DGs used in the test microgrid have a maximum power rating of 30 kW. In other microgrids, the power ratings of DGs may reach tens or hundreds of MW [3]–[5], where the distribution losses become significant. This is why the distribution line power losses in this particular test system has a limited benefits.

On the other hand, the OPF process has to find the values of m_{PI} which corresponds to the minimum power losses and taking into account current limitations in distribution lines as listed in Table 4.1. Moreover; the frequency constraint is a sensitive parameter in the optimization process. DGs working on the same microgrid should have the same operating frequency and this frequency should be maintained within the required limits.

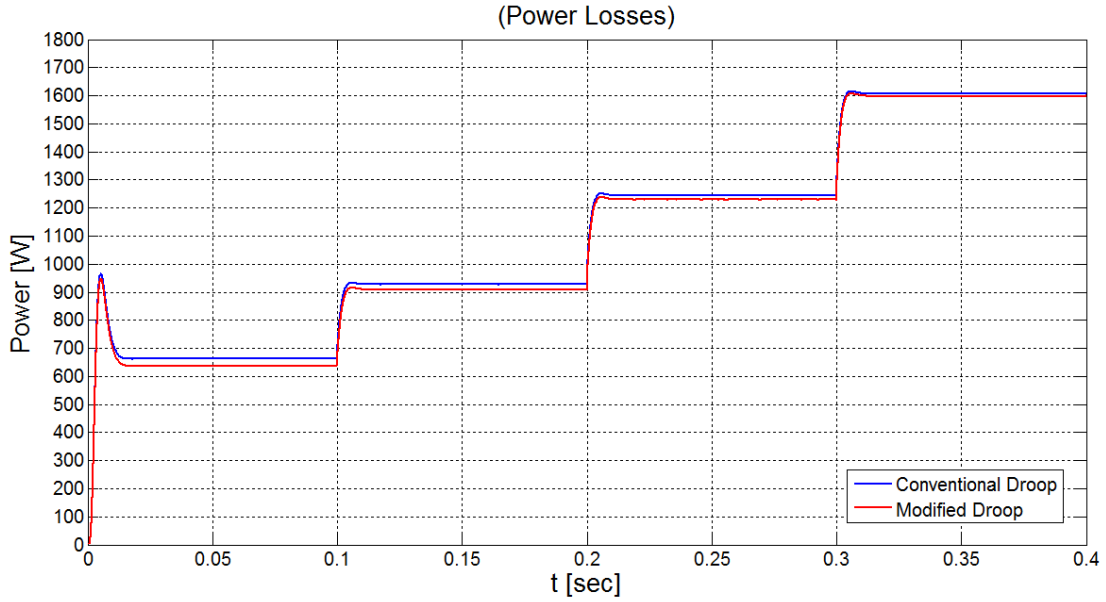

Fig. 4.6: Distribution lines power losses for conventional and modified droop control of DG_1 (Load 1 *PF*=0.85).

Fig. 4.7 shows the output frequency of each inverter under conventional and modified droop control. The output frequency remains within the range [f_{min}; f_{max}] and in both cases, DG_1 and DG_2 are operating with the same frequency, consequently, the stability of the system is ensured. Another remark about the output frequency noticed from Fig. 4.7 is the fast transient response achieved in both cases. This validates the perfect functionality of the designed voltage controller (phase-lead compensator).

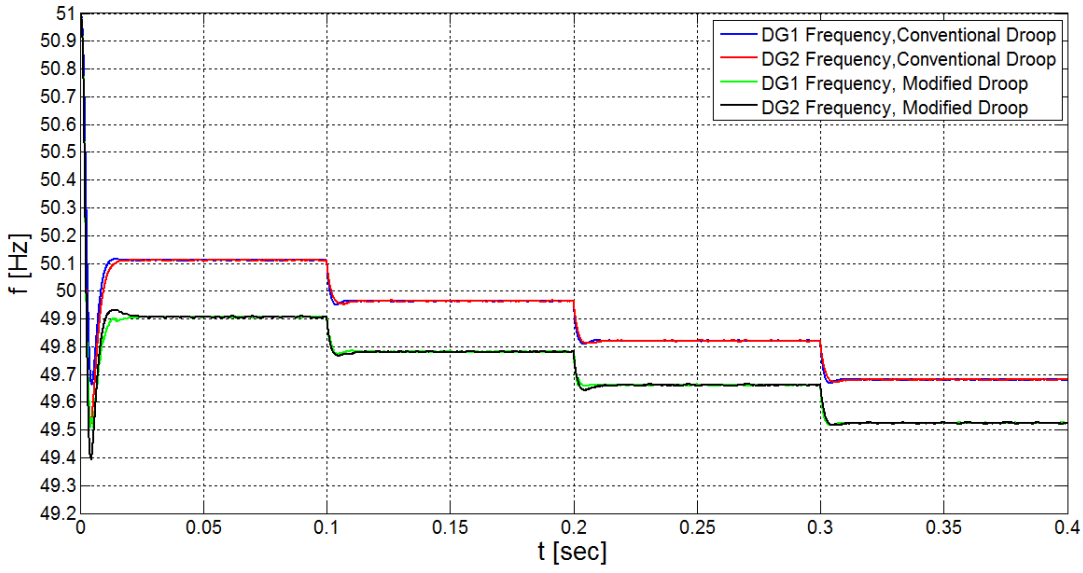

Fig. 4.7: Output frequency of DGs for conventional and modified droop control (Load 1 *PF*=0.85).

It should be mentioned that one of the factors which affect the calculation of the optimized droop slope is the frequency limitation or frequency constraint which has considered during the minimum power losses OPF process. The range of frequency, or Δf is 2 Hz and thus the range of m_{P1} is limited.

Fig. 4.8 to Fig. 4.10 shows Phase-a distribution line current for each line under conventional and modified droop control.

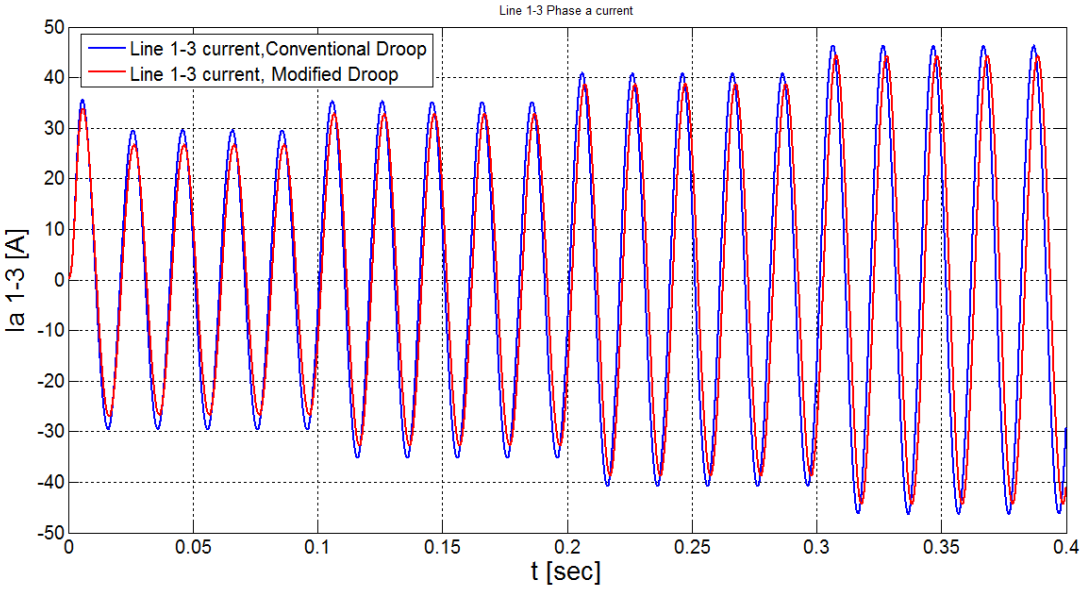

Fig. 4.8: Phase-a Line1-3 current (Load 1 *PF*=0.85).

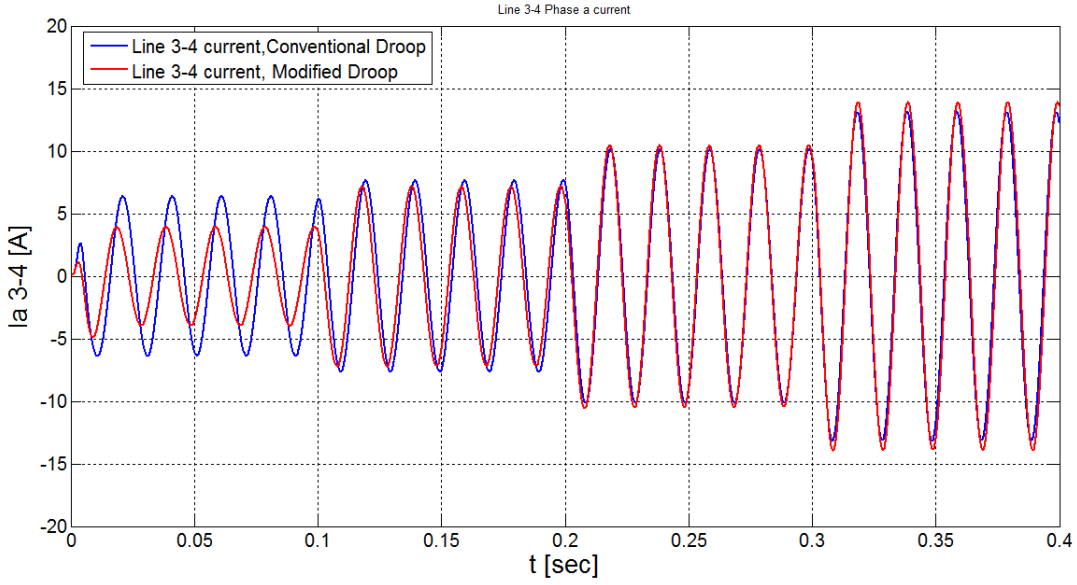

Fig. 4.9: Phase-a Line3-4 current (Load 1 *PF*=0.85).

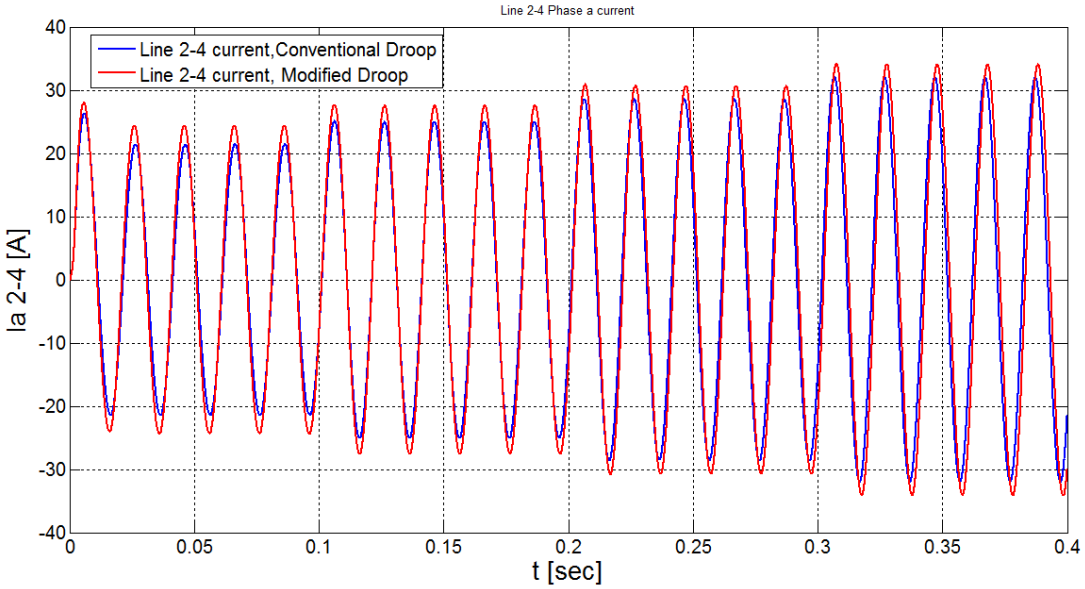

Fig. 4.10: Phase-a Line2-4 current (Load 1 *PF*=0.85).

It is clear from Fig. 4.8 that the distribution line current Line1-3 in the case of modified droop regulation is less than that of the conventional droop. This explains the overshoot reduction in the output power of DG_1 even without constructing a current regulation in the inner control loop of the DG_1.

4.4.3 Performance verification under 0.98 *PF* of Load 1

Adopting the same methodology in the previous subsection, the *PF* of the load at bus 3 is increased to 0.98 and the loads 12, 16, 20 and 24 kW are consecutively applied every 0.1 seconds.

Fig. 4.11 and Fig. 4.12 show the output power at each bus of the conventional and modified droop regulation, respectively. Similarly to the previous case, the output power of the conventional and modified droop regulation at the load buses are identical in both cases and the output power of DG_1 has been reduced in the case of using the modified droop regulation. The output power of DG_2 has been automatically increased to cover the power demanded by the loads. As expected, the overshoot in the output power of DG1 has been reduced in the case of modified droop regulation.

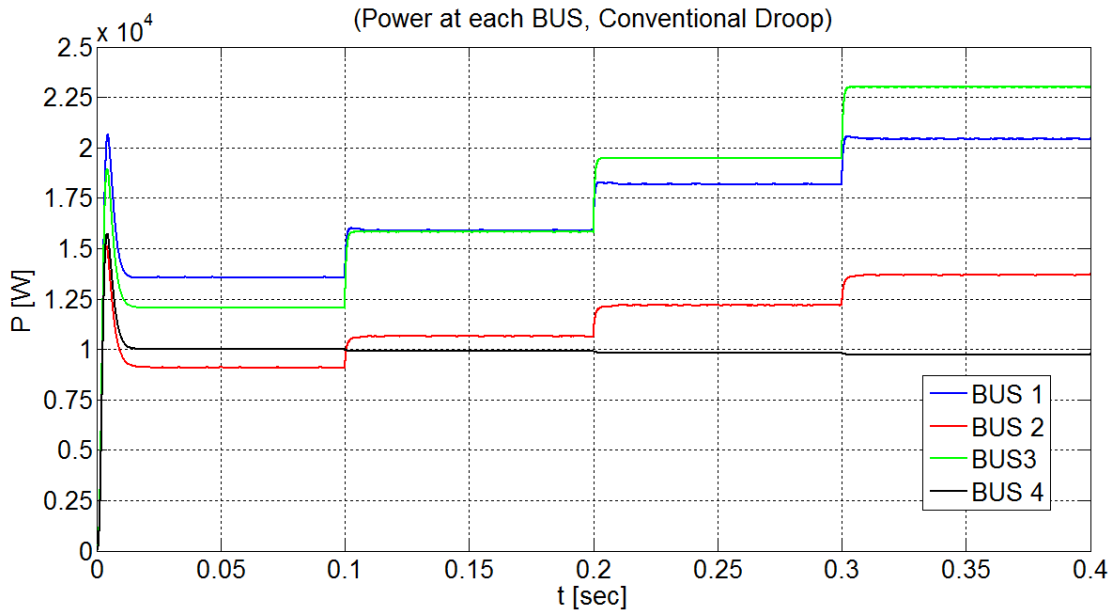

Fig. 4.11: Output average power at each bus of the conventional droop control (Load 1 *PF* = 0.98).

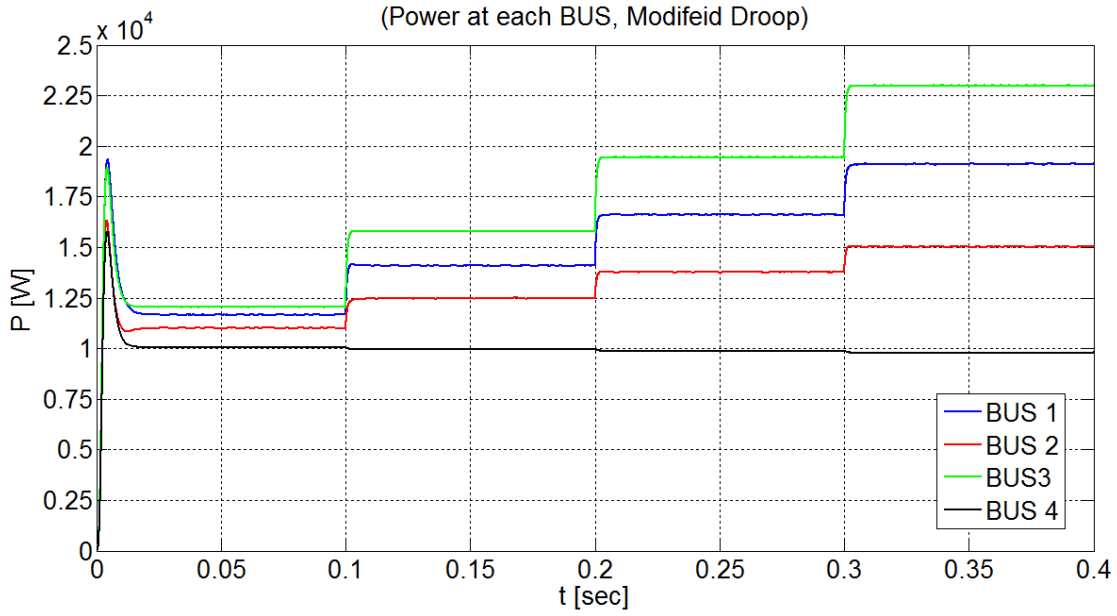

Fig. 4.12: Output average power at each bus of the Modified droop control (Load 1 *PF*=0.98).

Under 0.98 *PF* of Load 1, the proposed modified droop control has minimized the power losses in distribution lines as shown in Fig. 4.13. Additionally, in both cases, the output frequency of each inverter under conventional and modified droop control remains within the preset range [f_{min}; f_{max}] and both of them has identical output frequency as shown in Fig. 4.14.

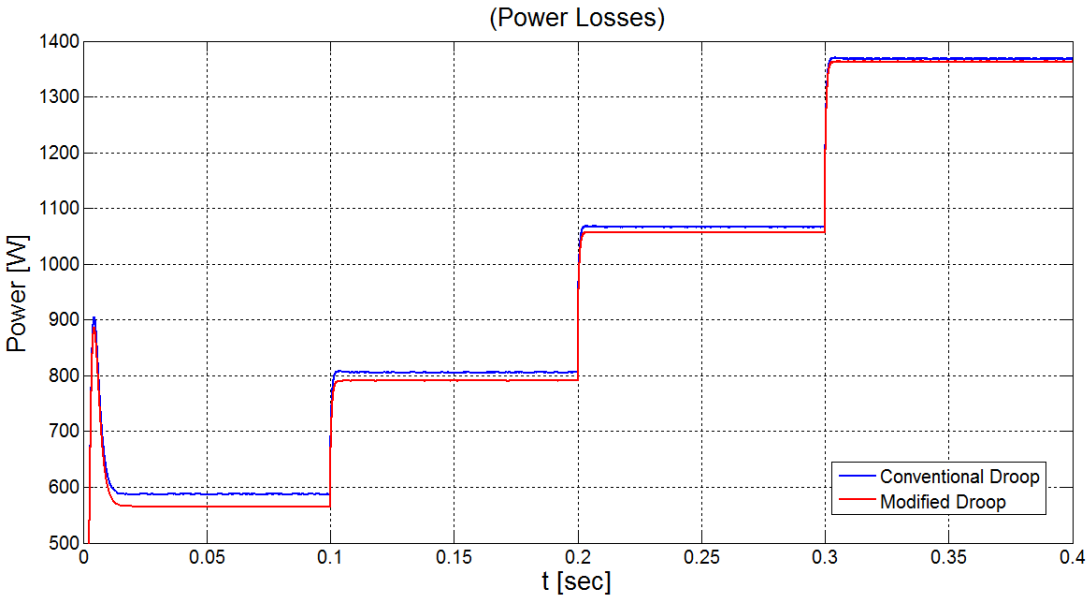

Fig. 4.13: Distribution lines power losses for conventional and modified droop control of DG1 (Load 1 *PF*=0.98).

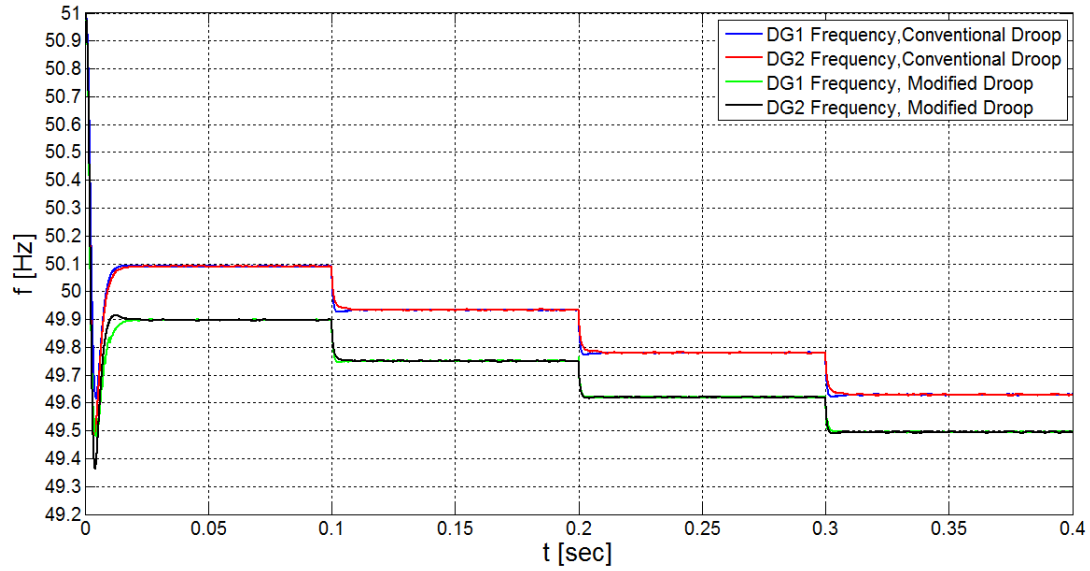

Fig. 4.14: Output frequency of DGs for conventional and modified droop control of DG1 (Load 1 *PF*=0.98).

The phase-a distribution line currents for each line under conventional and modified droop regulation with 0.98 *PF* of Load 1 are shown in Fig. 4.15 to Fig. 4.17. Again, the distribution line current Line1-3 in the case of modified droop regulation is less than that of the conventional droop as shown in Fig. 4.15.

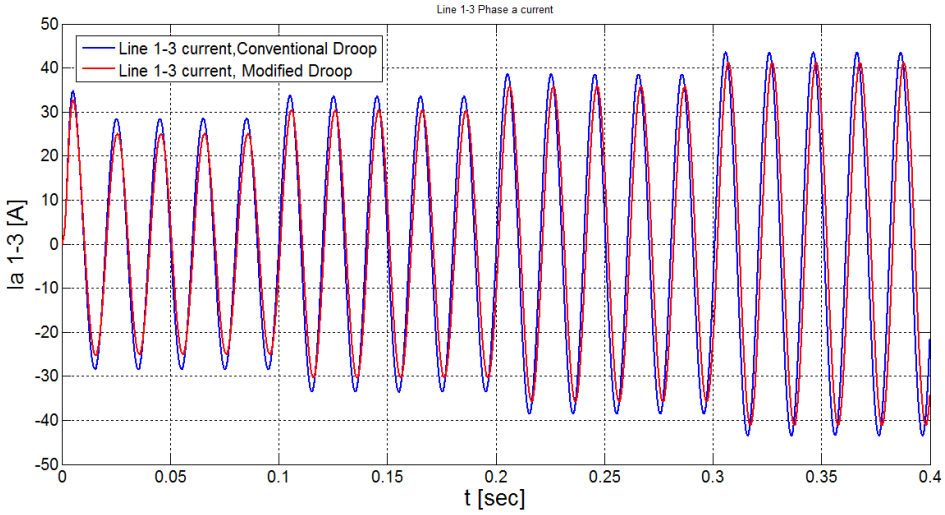

Fig. 4.15: Phase-a Line1-3 current (Load 1 *PF*=0.98).

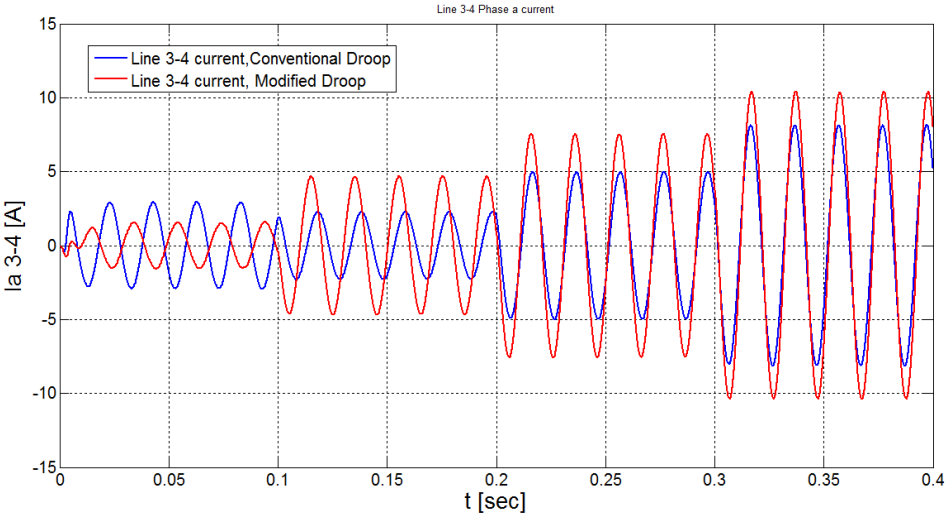

Fig. 4.16: Phase-a Line3-4 current (Load 1 *PF*=0.98).

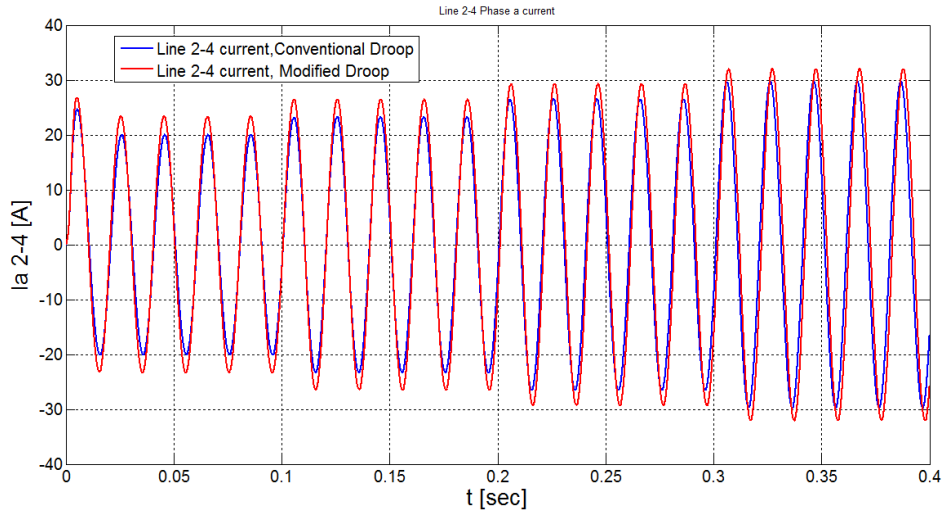

Fig. 4.17: Phase-a Line2-4 current (Load 1 *PF*=0.98).

A Comparison between the power losses for the first case when Load 1 *PF* was 0.85 (Fig. 4.6) and the case of 0.98 *PF* of Load 1(Fig. 4.13) is performed. Improving the power factor is one way of reducing power losses in distribution lines. The comparison of the power losses between conventional and modified droop control under different *PF* of Load 1 is shown in Fig. 4.18 and Fig. 4.19. It is clear that the power losses in distribution lines has been reduced by increasing the *PF* of Load 1.

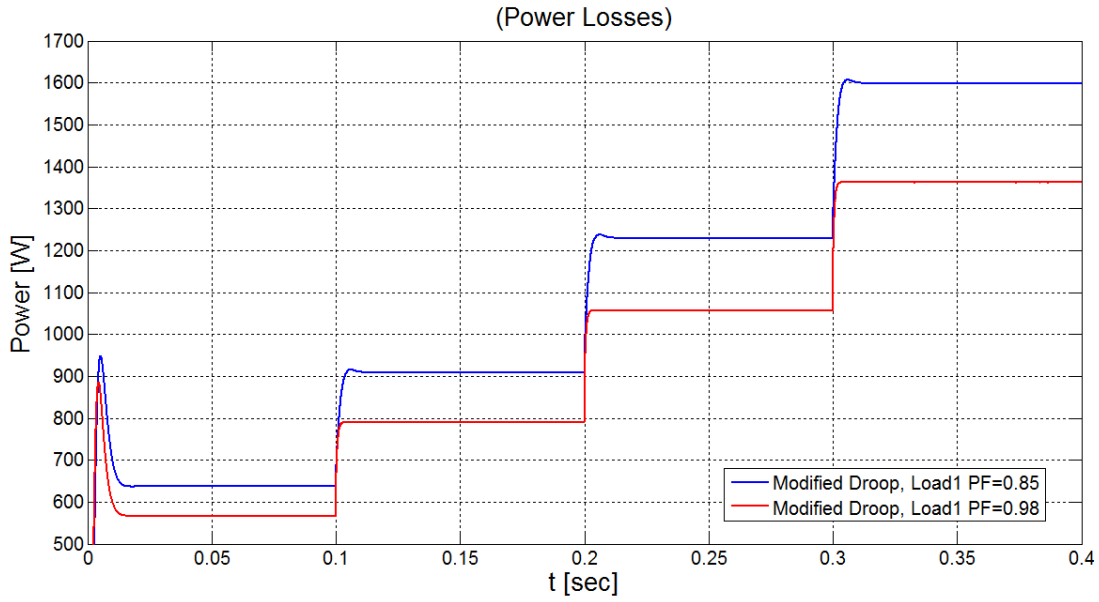

Fig. 4.18: Distribution lines power losses under different *PF* of Load 1 (Modified Droop).

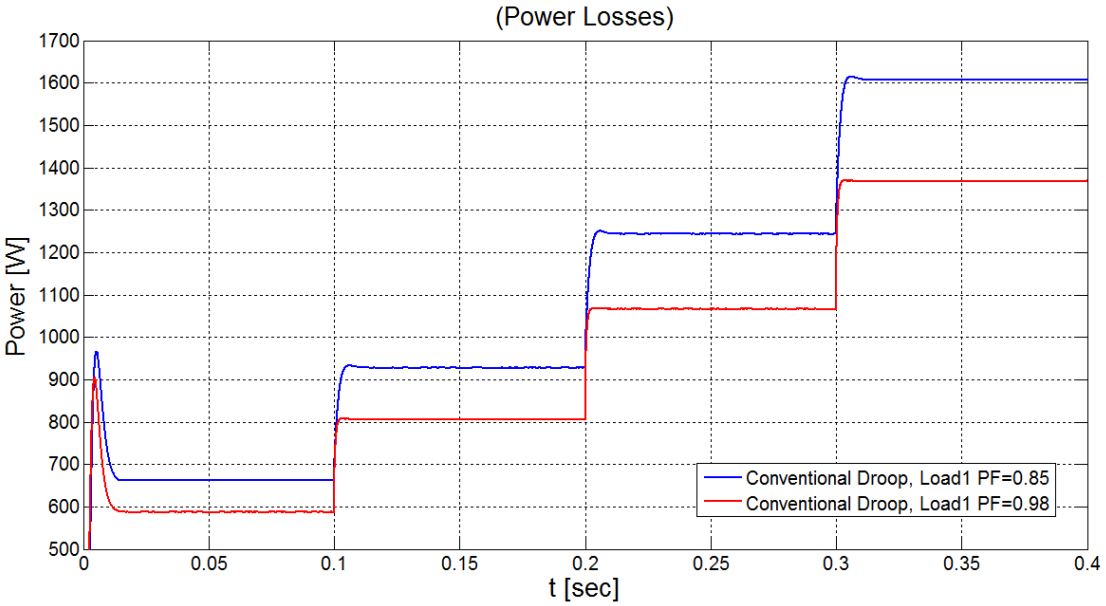

Fig. 4.19: Distribution lines power losses under different *PF* of Load 1 (Conventional Droop).

The next step for testing the proposed nonlinear droop control consists of imposing different values of Load 1 with different *PF* values which have not being considered during the optimization process.

4.4.4 Performance verification under different loading conditions

As a final test of the proposed modified droop control, the load at bus 3 will have some different values than those listed in appendix A and B. Table 4.3 lists four different loading conditions while Load 2 at bus 4 has been kept constant as in the previous sections. The same control parameters which are listed in Table 4.2 have been adopted.

Table 4.3: Loading Parameters of Load 1.

Load 1	**Average Power (W)**	***PF***
0.0 – 0.1 sec	10000	0.98
0.1 – 0.2 sec	11200	0.95
0.2 – 0.3 sec	16000	0.85
0.3 – 0.4 sec	21000	0.80

From Table 4.3, the first loading condition (from 0.0 to 0.1 sec) and the third one (0.2 to 0.3 sec) have the same average power and power factor in which have been considered during the OPF calculation for constructing the droop curves. From 0.1 to 0.2 sec, Load 1 has a new average power (11200 W) with a new power factor (0.95) as well as the last loading condition (21000 W with 0.80 PF). These new loading conditions have not been considered during the construction of the droop curves and they will be imposed on the system in order to validate the functionality of the proposed technique.

Fig. 4.20 and Fig. 4.21 shows the output average power at each bus for conventional and modified droop control. In both cases, the system presets a good transient response for load variation.

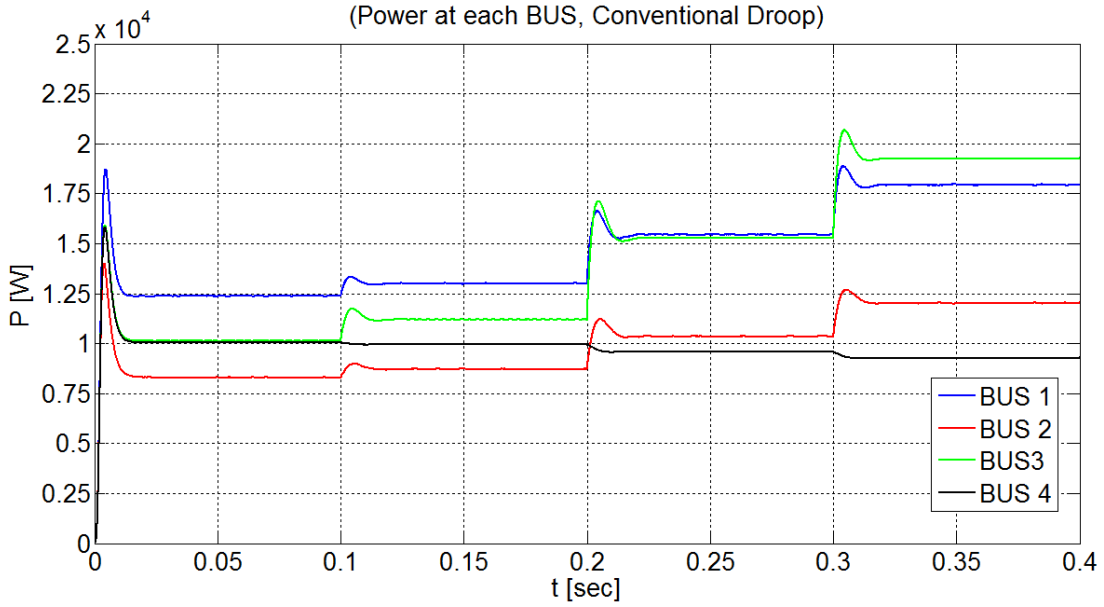

Fig. 4.20: Output average power at each bus of the conventional droop control.

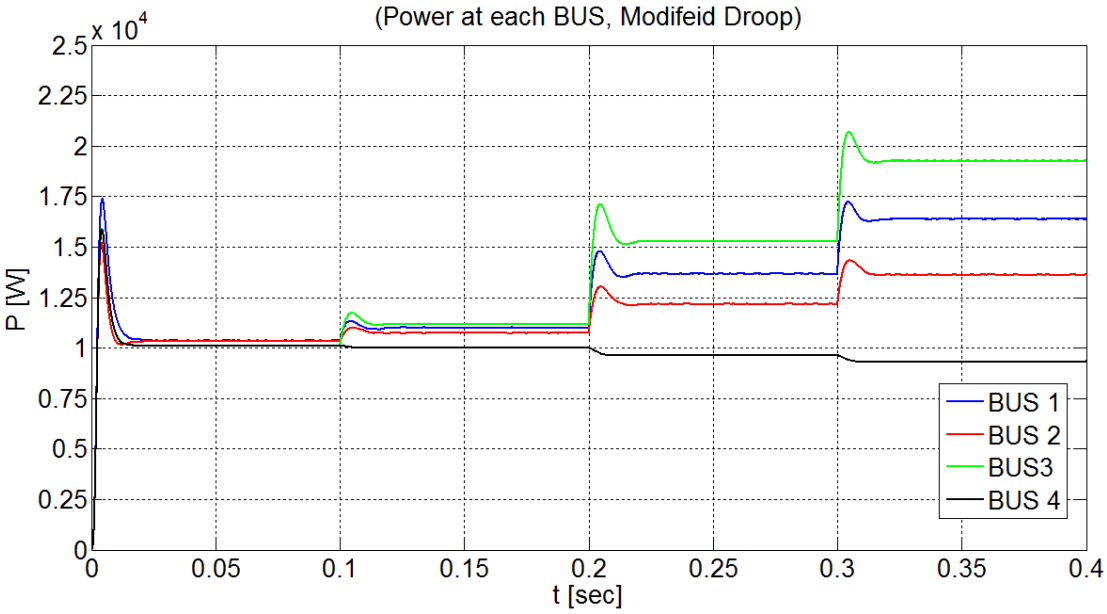

Fig. 4.21: Output average power at each bus of the Modified droop control.

The output frequency of each DGs under conventional and modified droop control is shown in Fig. 4.22. As expected, the output frequency of each inverter under conventional and modified droop control remains within the limits and in both cases, DG_1 and DG_2 are operating with the same frequency and thus, the *P vs. f* droop control is working properly. The transient response of the output frequency including the overshoot is acceptable and this also validates the functionality of the designed inner control loop.

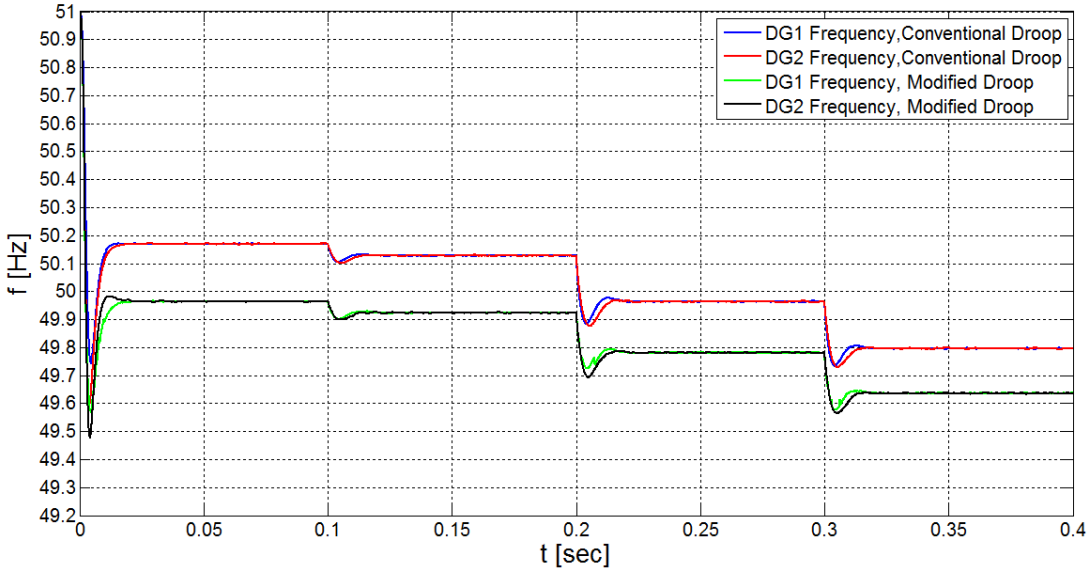

Fig. 4.22: Output frequency of DGs for conventional and modified droop control of DG1.

The objective of the proposed modified droop has been achieved, meaning that the power losses at the distribution lines have been minimized. Fig. 4.23 shows the power losses for both methods, and as expected, the power losses have been enhanced when using the modified droop control and by imposing different loading conditions which have not been considered during the construction of the droop curves. This validates the minimum power losses OPF method.

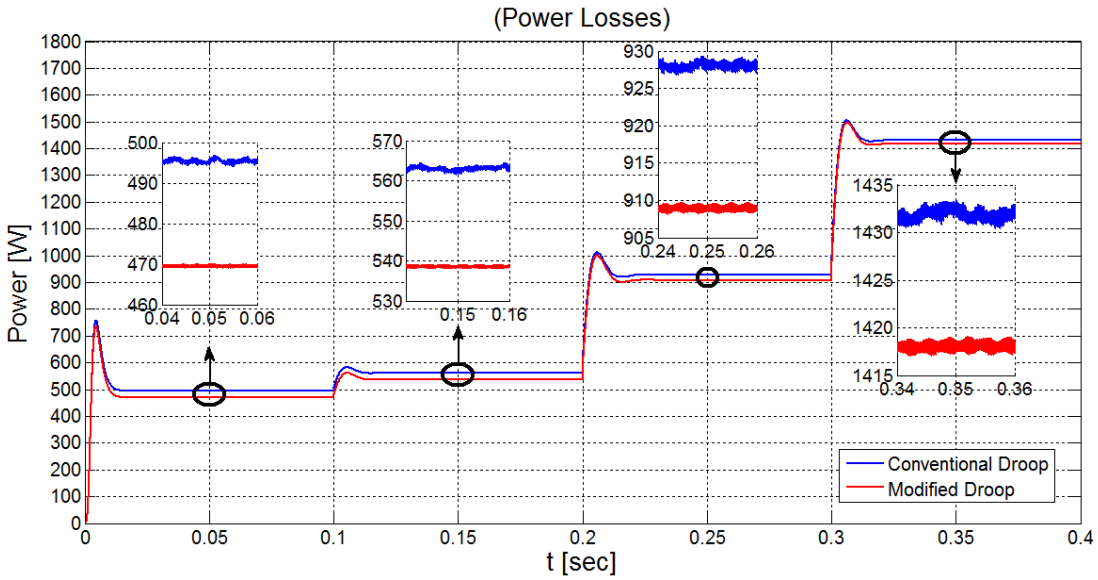

Fig. 4.23: Distribution lines power losses for conventional and modified droop control of DG1.

To summarize the results; the outcomes of time-domain simulations with the new implementation technique are compared with the results obtained from the minimum power losses OPF (listed in the appendixes) to prove the functionality and stability of the new approach. Different loading conditions have been applied in LV Islanded microgrid system. In the longer term, the approach is devoted to eliminate higher level controls and simplify the overall architecture.

Chapter 5 Conclusions and future work

5.1 Conclusion

In this thesis, a simple architecture of the inner control loop for VSI DGs has been designed which based on a simple phase-lead compensator of three stages with high phase margin in order to regulate the output voltage and frequency of the DG units. The voltage controller design process was based on frequency domain analysis with the help of bode diagrams to achieve a zero steady-state error and with acceptable transient response of the controlled variables. Time domain simulation under different loading conditions and different microgrid architecture has been carried out to validate the functionality of the designed controller. The work was more concentrated with islanded mode operation of LV microgrids.

The main objective of this thesis as stated precisely in the first chapter is concerned with the modeling of inverter-based DGs based on electrostatic synchronous machine concept.

A new modeling approach has been proposed for the inverter-based DGs based on the concept of electrostatic synchronous machines. The model has been constructed starting from the basic construction and principle of operation of electrostatic synchronous generators which based on electrostatic theories. A detailed mathematical expressions have been provided to accurately model the inverter-based DGs. The equivalence between the proposed model and the conventional small-signal model of inverter-based DGs, based on the duality concept, has been clearly stated.

According to the proposed model, each inverter can be replaced by its equivalent electrostatic machine model and the analysis of the whole microgrid can be performed in *dq* reference frame. A performance comparison between the proposed model and the

small-signal model of the VSIs has been carried out. Time domain simulation results carried out in MATLAB/Simulink environment presented a perfect matching between the two models thus validating the proposed modeling approach. As a result, the analysis of large and small-signal stability of microgrids with multi inverter-based DG can be performed by exploiting the swing equation of virtual electrostatic synchronous generators as being commonly done with the conventional synchronous generators.

Finally, a modified nonlinear droop control method for three-phase VSI DGs working on islanded LV microgrid has been proposed. The nonlinear droop regulation was based on off-line minimum distribution losses Optimal Power Flow with a new plug-and-play implementation technique, which has been established by constructing a lookup table for the optimized *P vs. f* droop slope of the VSI DG with the highest power capacity.

A comparison between the conventional droop and the proposed nonlinear droop regulation has been carried out in MATLAB/Simulink environment. Time domain simulation results show the superiority of the nonlinear droop regulation method in terms of mitigation the distribution line power losses as well as the transient response of the system variables.

5.2 Future Work

Apart from the advantages of the proposed models and techniques, there is still margin for further developments and investigations. Some of the future research directions are listed below:

- Study of the performance of the inner control loop of VSIs by employing voltage and current control loops and inspection of the possibility of improving the droop controllers used in this thesis to achieve a smooth transition between on-grid and off-grid operation.

- Adoption of Virtual Impedance loop to overcome the problem of average and reactive power coupling that appears in LV microgrid where the distribution line impedance is mainly resistive.
- Investigation of the chance of applying the proposed ESG model of VSIs for heterogeneous microgrids which include different types of DGs. Moreover, study the microgrids stability with the proposed ESG model by exploiting the swing equation.
- Extension of the nonlinear droop control proposed in chapter 3 in larger systems and with higher power ratings of DG units.
- Investigation of the advantages of expanding the nonlinear droop regulation in terms of minimizing the power losses in distribution lines by considering *Q vs. V* optimization in line with the optimization of *P vs. f* droop.

REFERENCES

[1] Q. Fu, A. Hamidi, A. Nasiri, V. Bhavaraju, S. B. Krstic, and P. Theisen, "The Role of Energy Storage in a Microgrid Concept: Examining the opportunities and promise of microgrids.," *IEEE Electrif. Mag.*, vol. 1, no. 2, pp. 21–29, Dec. 2013.

[2] J. Wang and L. M. Costa, "On the design of standard application function blocks for microgrid automation," in *2016 IEEE Innovative Smart Grid Technologies - Asia (ISGT-Asia)*, 2016, pp. 1157–1164.

[3] T. E. Del Carpio Huayllas, D. S. Ramos, and R. L. Vasquez-Arnez, "Microgrid systems: Current status and challenges," in *2010 IEEE/PES Transmission and Distribution Conference and Exposition: Latin America (T&D-LA)*, 2010, pp. 7–12.

[4] P. J. Binduhewa, M. Barnes, and A. Renfrew, "Standard microsource interface for a microgrid," in *CIRED Seminar 2008: SmartGrids for Distribution*, 2008, pp. 26–26.

[5] B. Kroposki, T. Basso, and R. DeBlasio, "Microgrid standards and technologies," in *2008 IEEE Power and Energy Society General Meeting - Conversion and Delivery of Electrical Energy in the 21st Century*, 2008, pp. 1–4.

[6] M. Vaziri, S. Vadhva, T. Oneal, and M. Johnson, "Smart grid, Distributed Generation, and standards," in *2011 IEEE Power and Energy Society General Meeting*, 2011, pp. 1–8.

[7] R. Teodorescu, M. Liserre, and P. Rodríguez, *Grid converters for photovoltaic and wind power systems*. .

[8] H. Laaksonen, P. Saari, and R. Komulainen, "Voltage and frequency control of inverter based weak LV network microgrid," in *2005 International Conference on Future Power Systems*, 2005, p. 6 pp.-pp.6.

[9] H. Zeineldin, E. El-saadany, and M. A. Salama, "Distributed Generation Micro-Grid Operation: Control and Protection," in *2006 Power Systems Conference: Advanced Metering, Protection, Control, Communication, and Distributed Resources*, 2006, pp. 105–111.

[10] H. Nikkhajoei and R. H. Lasseter, "Distributed Generation Interface to the CERTS Microgrid," *IEEE Trans. Power Deliv.*, vol. 24, no. 3, pp. 1598–1608, Jul. 2009.

[11] G. Davis, "Integration of Distributed Energy Resources The CERTS MicroGrid

Concept CALIFORNIA ENERGY COMMISSION," 2003.

[12] J. M. Guerrero, J. C. Vasquez, and R. Teodorescu, "Hierarchical control of droop-controlled DC and AC microgrids — a general approach towards standardization," in *2009 35th Annual Conference of IEEE Industrial Electronics*, 2009, pp. 4305–4310.

[13] J. M. Guerrero, J. C. Vasquez, J. Matas, L. G. de Vicuna, and M. Castilla, "Hierarchical Control of Droop-Controlled AC and DC Microgrids—A General Approach Toward Standardization," *IEEE Trans. Ind. Electron.*, vol. 58, no. 1, pp. 158–172, Jan. 2011.

[14] N. Hatziargyriou, H. Asano, R. Iravani, and C. Marnay, "Microgrids," *IEEE Power Energy Mag.*, vol. 5, no. 4, pp. 78–94, Jul. 2007.

[15] Y. Li, D. M. Vilathgamuwa, and P. C. Loh, "Design, Analysis, and Real-Time Testing of a Controller for Multibus Microgrid System," *IEEE Trans. Power Electron.*, vol. 19, no. 5, pp. 1195–1204, Sep. 2004.

[16] F. Katiraei and M. R. Iravani, "Power Management Strategies for a Microgrid With Multiple Distributed Generation Units," *IEEE Trans. Power Syst.*, vol. 21, no. 4, pp. 1821–1831, Nov. 2006.

[17] R. Majumder, "Some Aspects of Stability in Microgrids," *IEEE Trans. Power Syst.*, vol. 28, no. 3, pp. 3243–3252, Aug. 2013.

[18] L. Y. Wang, M. P. Polis, C. Wang, F. Lin, and G. Yin, "Voltage robust stability in microgrid power management," in *Proceedings of the IEEE Conference on Decision and Control*, 2013, pp. 6928–6933.

[19] X. Tang, W. Deng, and Z. Qi, "Investigation of the dynamic stability of microgrid," *IEEE Trans. Power Syst.*, vol. 29, no. 2, pp. 698–706, Mar. 2014.

[20] Zhao Wang, Meng Xia, and M. Lemmon, "Voltage stability of weak power distribution networks with inverter connected sources," in *2013 American Control Conference*, 2013, pp. 6577–6582.

[21] N. Bottrell, M. Prodanovic, and T. C. Green, "Dynamic Stability of a Microgrid With an Active Load," *IEEE Trans. Power Electron.*, vol. 28, no. 11, pp. 5107–5119, Nov. 2013.

[22] M. Rasheduzzaman, J. A. Mueller, and J. W. Kimball, "An Accurate Small-Signal Model of Inverter- Dominated Islanded Microgrids Using dq Reference Frame," *IEEE J. Emerg. Sel. Top. Power Electron.*, vol. 2, no. 4, pp. 1070–1080, Dec. 2014.

[23] T. Wijnhoven, J. Tant, and G. Deconinck, “Inverter modelling techniques for protection studies,” in *2012 3rd IEEE International Symposium on Power Electronics for Distributed Generation Systems (PEDG)*, 2012, pp. 187–194.

[24] F. Katiraei, M. R. Iravani, and P. W. Lehn, “Small-signal dynamic model of a micro-grid including conventional and electronically interfaced distributed resources,” *IET Gener. Transm. Distrib.*, vol. 1, no. 3, p. 369, 2007.

[25] N. Pogaku, M. Prodanovic, and T. C. Green, “Modeling, Analysis and Testing of Autonomous Operation of an Inverter-Based Microgrid,” *IEEE Trans. Power Electron.*, vol. 22, no. 2, pp. 613–625, Mar. 2007.

[26] S. Tabatabaee, H. R. Karshenas, A. Bakhshai, and P. Jain, “Investigation of droop characteristics and X/R ratio on small-signal stability of autonomous Microgrid,” in *2011 2nd Power Electronics, Drive Systems and Technologies Conference*, 2011, pp. 223–228.

[27] M. A. Hassan and M. A. Abido, “Optimal Design of Microgrids in Autonomous and Grid-Connected Modes Using Particle Swarm Optimization,” *IEEE Trans. Power Electron.*, vol. 26, no. 3, pp. 755–769, Mar. 2011.

[28] Yu Zhang, Zhenhua Jiang, and Xunwei Yu, “Small-signal modeling and analysis of parallel-connected voltage source inverters,” in *2009 IEEE 6th International Power Electronics and Motion Control Conference*, 2009, pp. 377–383.

[29] E. A. A. Coelho, P. C. Cortizo, and P. F. D. Garcia, “Small-signal stability for parallel-connected inverters in stand-alone AC supply systems,” *IEEE Trans. Ind. Appl.*, vol. 38, no. 2, pp. 533–542, 2002.

[30] Q.-C. Zhong and G. Weiss, “Static synchronous generators for distributed generation and renewable energy,” in *2009 IEEE/PES Power Systems Conference and Exposition*, 2009, pp. 1–6.

[31] Q.-C. Zhong and G. Weiss, “Synchronverters: Inverters That Mimic Synchronous Generators,” *IEEE Trans. Ind. Electron.*, vol. 58, no. 4, pp. 1259–1267, Apr. 2011.

[32] V. Natarajan and G. Weiss, “Synchronverters With Better Stability Due to Virtual Inductors, Virtual Capacitors, and Anti-Windup,” *IEEE Trans. Ind. Electron.*, vol. 64, no. 7, pp. 5994–6004, Jul. 2017.

[33] Q.-C. Zhong, G. C. Konstantopoulos, B. Ren, and M. Krstic, “Improved Synchronverters with Bounded Frequency and Voltage for Smart Grid Integration,” *IEEE Trans. Smart Grid*, pp. 1–1, 2016.

[34] G. C. Konstantopoulos, Q.-C. Zhong, B. Ren, and M. Krstic, “Boundedness of Synchronverters,” in *2015 European Control Conference (ECC)*, 2015, pp. 1050–1055.

[35] Qing-Chang Zhong, Phi-Long Nguyen, Zhenyu Ma, and Wanxing Sheng, “Self-Synchronized Synchronverters: Inverters Without a Dedicated Synchronization Unit,” *IEEE Trans. Power Electron.*, vol. 29, no. 2, pp. 617–630, Feb. 2014.

[36] J. Alipoor, Y. Miura, and T. Ise, “Distributed generation grid integration using virtual synchronous generator with adoptive virtual inertia,” in *2013 IEEE Energy Conversion Congress and Exposition*, 2013, pp. 4546–4552.

[37] T. Shintai, Y. Miura, and T. Ise, “Oscillation Damping of a Distributed Generator Using a Virtual Synchronous Generator,” *IEEE Trans. Power Deliv.*, vol. 29, no. 2, pp. 668–676, Apr. 2014.

[38] Y. Chen, R. Hesse, D. Turschner, and H.-P. Beck, “Improving the grid power quality using virtual synchronous machines,” in *2011 International Conference on Power Engineering, Energy and Electrical Drives*, 2011, pp. 1–6.

[39] Ningyi Xu, Yue Wang, Mingxuan Li, Wenti Wang, Hao Wang, and Hailong Zhang, “Analysis and improvement of damping factor based on virtual synchronous generator control,” in *2016 IEEE 8th International Power Electronics and Motion Control Conference (IPEMC-ECCE Asia)*, 2016, pp. 1990–1996.

[40] H. Xu, X. Zhang, F. Liu, F. Mao, R. Shi, and H. Ni, “An improved Virtual Synchronous Generator algorithm for system stability enhancement,” in *2015 IEEE 2nd International Future Energy Electronics Conference, IFEEC 2015*, 2015, pp. 1–6.

[41] J. Liu, Y. Miura, and T. Ise, “Comparison of Dynamic Characteristics Between Virtual Synchronous Generator and Droop Control in Inverter-Based Distributed Generators,” *IEEE Trans. Power Electron.*, vol. 31, no. 5, pp. 3600–3611, May 2016.

[42] Jia Liu, Y. Miura, and T. Ise, “Dynamic characteristics and stability comparisons between virtual synchronous generator and droop control in inverter-based distributed generators,” in *2014 International Power Electronics Conference (IPEC-Hiroshima 2014 - ECCE ASIA)*, 2014, pp. 1536–1543.

[43] C. T. Rim, D. Y. Hu, and G. H. Cho, “Transformers as equivalent circuits for switches: general proofs and D-Q transformation-based analyses,” *IEEE Trans.*

Ind. Appl., vol. 26, no. 4, pp. 777–785, 1990.

[44] F. Andrade, L. Romeral, K. Kampouropoulos, and J. Cusido, "New mathematical model of an inverter-based generator for stability studies of microgrid systems," in *4th International Conference on Power Engineering, Energy and Electrical Drives*, 2013, pp. 944–949.

[45] F. A. Andrade, L. Romeral, J. Cusidó, and J. J. Cárdenas, "New model of a converter-based generator using electrostatic synchronous machine concept," *IEEE Trans. Energy Convers.*, vol. 29, no. 2, pp. 344–353, Jun. 2014.

[46] F. Andrade, K. Kampouropoulos, L. Romeral, J. C. Vasquez, and J. M. Guerrero, "Study of large-signal stability of an inverter-based generator using a Lyapunov function," in *IECON 2014 - 40th Annual Conference of the IEEE Industrial Electronics Society*, 2014, pp. 1840–1846.

[47] E. T. Andrade, P. E. M. J. Ribeiro, J. O. P. Pinto, C.-L. Chen, J.-S. Lai, and N. Kees, "A novel power calculation method for droop-control microgrid systems," in *2012 Twenty-Seventh Annual IEEE Applied Power Electronics Conference and Exposition (APEC)*, 2012, pp. 2254–2258.

[48] A. Klem, M. H. Nehrir, and K. Dehghanpour, "Frequency stabilization of an islanded microgrid using droop control and demand response," in *2016 North American Power Symposium (NAPS)*, 2016, pp. 1–6.

[49] A. Elrayyah, F. Cingoz, and Y. Sozer, "Construction of Nonlinear Droop Relations to Optimize Islanded Microgrid Operation," *IEEE Trans. Ind. Appl.*, vol. 51, no. 4, pp. 3404–3413, Jul. 2015.

[50] M. C. Chandorkar, D. M. Divan, and R. Adapa, "Control of parallel connected inverters in standalone AC supply systems," *IEEE Trans. Ind. Appl.*, vol. 29, no. 1, pp. 136–143, 1993.

[51] M. Ramezani and S. Li, "Voltage and frequency control of islanded microgrid based on combined direct current vector control and droop control," in *2016 IEEE Power and Energy Society General Meeting (PESGM)*, 2016, pp. 1–5.

[52] M. I. Azim, M. A. Hossain, M. J. Hossain, and H. R. Pota, "Droop Control for islanded microgrids with compensating approach," in *2015 Australasian Universities Power Engineering Conference (AUPEC)*, 2015, pp. 1–6.

[53] K. De Brabandere, B. Bolsens, J. Van den Keybus, A. Woyte, J. Driesen, and R. Belmans, "A Voltage and Frequency Droop Control Method for Parallel Inverters,"

IEEE Trans. Power Electron., vol. 22, no. 4, pp. 1107–1115, Jul. 2007.

[54] Y. Guan, J. M. Guerrero, X. Zhao, and J. C. Vasquez, "Comparison of a synchronous reference frame virtual impedance-based autonomous current sharing control with conventional droop control for parallel-connected inverters," in *2016 IEEE 8th International Power Electronics and Motion Control Conference (IPEMC-ECCE Asia)*, 2016, pp. 3419–3426.

[55] X. Yang, Y. Du, J. Su, L. Chang, Y. Shi, and J. Lai, "An Optimal Secondary Voltage Control Strategy for an Islanded Multibus Microgrid," *IEEE J. Emerg. Sel. Top. Power Electron.*, vol. 4, no. 4, pp. 1236–1246, Dec. 2016.

[56] C. Yuen, A. Oudalov, and A. Timbus, "The Provision of Frequency Control Reserves From Multiple Microgrids," *IEEE Trans. Ind. Electron.*, vol. 58, no. 1, pp. 173–183, Jan. 2011.

[57] C. K. Sao and P. W. Lehn, "Control and Power Management of Converter Fed Microgrids," *IEEE Trans. Power Syst.*, vol. 23, no. 3, pp. 1088–1098, Aug. 2008.

[58] A. Villa, F. Belloni, R. Chiumeo, and C. Gandolfi, "Conventional and reverse droop control in islanded microgrid: Simulation and experimental test," in *2016 International Symposium on Power Electronics, Electrical Drives, Automation and Motion (SPEEDAM)*, 2016, pp. 288–294.

[59] Z. Ahmad and S. N. Singh, "DROOP Control Strategies of Conventional Power System Versus Microgrid Based Power Systems - A Review," in *2015 International Conference on Computational Intelligence and Communication Networks (CICN)*, 2015, pp. 1499–1504.

[60] M. M. A. Abdelaziz, H. E. Farag, E. F. El-Saadany, and Y. A.-R. I. Mohamed, "A Novel and Generalized Three-Phase Power Flow Algorithm for Islanded Microgrids Using a Newton Trust Region Method," *IEEE Trans. Power Syst.*, vol. 28, no. 1, pp. 190–201, Feb. 2013.

[61] F. Cingoz, A. Elrayyah, and Y. Sozer, "Plug and play nonlinear droop construction scheme to optimize microgrid operations," in *2014 IEEE Energy Conversion Congress and Exposition (ECCE)*, 2014, pp. 76–83.

[62] F. Cingoz, A. Elrayyah, and Y. Sozer, "Plug-and-Play Nonlinear Droop Construction Scheme to Optimize Islanded Microgrid Operations," *IEEE Trans. Power Electron.*, vol. 32, no. 4, pp. 2743–2756, Apr. 2017.

[63] M. Sinha, S. Dhople, B. Johnson, N. Ainsworth, and F. Dorfler, "Nonlinear

supersets to droop control," in *2015 IEEE 16th Workshop on Control and Modeling for Power Electronics (COMPEL)*, 2015, pp. 1–6.

[64] V. Mariani, F. Vasca, and J. M. Guerrero, "Dynamic-phasor-based nonlinear modelling of AC islanded microgrids under droop control," in *2014 IEEE 11th International Multi-Conference on Systems, Signals & Devices (SSD14)*, 2014, pp. 1–6.

[65] S. M. Ashabani and Y. A.-R. I. Mohamed, "General Interface for Power Management of Micro-Grids Using Nonlinear Cooperative Droop Control," *IEEE Trans. Power Syst.*, vol. 28, no. 3, pp. 2929–2941, Aug. 2013.

[66] Y. Sun, W. Huang, G. Wang, Wenjun Wang, D. Wang, and Li Zhang, "Study of control strategy of DG based on nonlinear droop characteristic," in *2012 China International Conference on Electricity Distribution*, 2012, pp. 1–4.

[67] K.-K. Jen, G.-H. You, and H.-C. Chiang, "Improved droop control method with precise current sharing and voltage regulation," *IET Power Electron.*, vol. 9, no. 4, pp. 789–800, Mar. 2016.

[68] E. Tegling, D. F. Gayme, and H. Sandberg, "Performance metrics for droop-controlled microgrids with variable voltage dynamics," in *2015 54th IEEE Conference on Decision and Control (CDC)*, 2015, pp. 7502–7509.

[69] C. A. Hernandez-Aramburo, T. C. Green, and N. Mugniot, "Fuel Consumption Minimization of a Microgrid," *IEEE Trans. Ind. Appl.*, vol. 41, no. 3, pp. 673–681, May 2005.

[70] L. A. Carniato, R. B. Godoy, J. O. P. Pinto, C. A. Canesin, and P. E. M. J. Ribeiro, "Dynamic adaptation of droop control curves for microgrid connected inverters with variable input power," in *2013 Brazilian Power Electronics Conference*, 2013, pp. 1022–1028.

[71] M. H. (Muhammad H. Rashid, *Power electronics : circuits, devices, and applications*, 3rd ed. Pearson/Prentice Hall, 2004.

[72] M. Prodanovic and T. C. Green, "Control and filter design of three-phase inverters for high power quality grid connection," *IEEE Trans. Power Electron.*, vol. 18, no. 1, pp. 373–380, Jan. 2003.

[73] G. Lo Calzo, A. Lidozzi, L. Solero, and F. Crescimbini, "LC Filter Design for On-Grid and Off-Grid Distributed Generating Units," *IEEE Trans. Ind. Appl.*, vol. 51, no. 2, pp. 1639–1650, Mar. 2015.

[74] M. Liserre, F. Blaabjerg, and S. Hansen, “Design and control of an LCL-filter based three-phase active rectifier,” in *Conference Record of the 2001 IEEE Industry Applications Conference. 36th IAS Annual Meeting (Cat. No.01CH37248)*, vol. 1, pp. 299–307.

[75] K. H. Ahmed, S. J. Finney, and B. W. Williams, “Passive Filter Design for Three-Phase Inverter Interfacing in Distributed Generation,” in *2007 Compatibility in Power Electronics*, 2007, pp. 1–9.

[76] M. W. Layland, “Generalised electrostatic-machine theory,” *Proc. Inst. Electr. Eng.*, vol. 116, no. 3, p. 403, 1969.

[77] S. Tapuchi and D. Baimel, “Novel multilayer differential linear electrostatic motor,” in *2014 International Symposium on Power Electronics, Electrical Drives, Automation and Motion*, 2014, pp. 1368–1372.

[78] F. J. Santana, J. M. Monzon, S. Garcia-Alonso, and J. A. Montiel-Nelson, “Lumped parametric model for an electrostatic induction micromotor using GA,” in *2009 35th Annual Conference of IEEE Industrial Electronics*, 2009, pp. 4029–4033.

[79] F. J. Santana Martin, S. Garcia-Alonso Montoya, J. M. Monzon Verona, and J. A. Montiel-Nelson, “Analysis and modeling of an electrostatic induction micromotor,” in *2008 18th International Conference on Electrical Machines*, 2008, pp. 1–5.

[80] A. Yamamoto, H. Yasui, N. Shimizu, and T. Higuchi, “Development of electrostatic levitation motor for vacuum condition,” in *2003 IEEE International Symposium on Industrial Electronics (Cat. No.03TH8692)*, vol. 2, pp. 934–939.

[81] N. Yamashita, A. Yamamoto, M. Gondo, and T. Higuchi, “Evaluation of an Electrostatic Film Motor Driven by Two-Four-Phase AC Voltage and Electrostatic Induction,” in *Proceedings 2007 IEEE International Conference on Robotics and Automation*, 2007, pp. 1572–1577.

[82] H. Shehadeh, S. Favuzza, and E. R. Sanseverino, “Electrostatic synchronous generator model of an Inverter-Based Distributed Generators,” in *2015 International Conference on Renewable Energy Research and Applications (ICRERA)*, 2015, pp. 885–889.

[83] H. Shehadeh, V. Boscaino, S. Favuzza, and E. R. Sanseverino, “Mathematical modelling of an inverter-based distributed generator,” in *2016 IEEE 16th International Conference on Environment and Electrical Engineering (EEEIC)*,

2016, pp. 1–6.

[84] C. Li, S. K. Chaudhary, M. Savaghebi, J. C. Vasquez, and J. M. Guerrero, “Power Flow Analysis for Low-Voltage AC and DC Microgrids Considering Droop Control and Virtual Impedance,” *IEEE Trans. Smart Grid*, vol. 8, no. 6, pp. 2754–2764, Nov. 2017.

[85] C. A. Macana and H. R. Pota, “Adaptive synchronous reference frame virtual impedance controller for accurate power sharing in islanded ac-microgrids: A faster alternative to the conventional droop control,” in *2017 IEEE Energy Conversion Congress and Exposition (ECCE)*, 2017, pp. 3728–3735.

[86] H. Zhang, S. Kim, Q. Sun, and J. Zhou, “Distributed Adaptive Virtual Impedance Control for Accurate Reactive Power Sharing Based on Consensus Control in Microgrids,” *IEEE Trans. Smart Grid*, vol. 8, no. 4, pp. 1749–1761, Jul. 2017.

[87] A. Micallef, M. Apap, C. Spiteri-Staines, and J. M. Guerrero, “Performance comparison for virtual impedance techniques used in droop controlled islanded microgrids,” in *2016 International Symposium on Power Electronics, Electrical Drives, Automation and Motion (SPEEDAM)*, 2016, pp. 695–700.

[88] T. L. Vandoorn, J. D. M. De Kooning, B. Meersman, J. M. Guerrero, and L. Vandevelde, “Automatic Power-Sharing Modification of P/V Droop Controllers in Low-Voltage Resistive Microgrids,” *IEEE Trans. Power Deliv.*, vol. 27, no. 4, pp. 2318–2325, Oct. 2012.

[89] E. R. Sanseverino, N. Q. Nguyen, M. L. Di Silvestre, G. Zizzo, F. de Bosio, and Q. T. T. Tran, “Frequency constrained optimal power flow based on glow-worm swarm optimization in islanded microgrids,” in *2015 AEIT International Annual Conference (AEIT)*, 2015, pp. 1–6.

[90] E. R. Sanseverino *et al.*, “Optimizing droop coefficients for minimum cost operation of islanded micro-grids,” in *2017 IEEE International Conference on Environment and Electrical Engineering and 2017 IEEE Industrial and Commercial Power Systems Europe (EEEIC / I&CPS Europe)*, 2017, pp. 1–6.

[91] Q. T. T. Tran, H. Shehadeh, E. R. Sanseverino, S. Favuzza, and M. L. Di Silvestre, “Nonlinear droop control for minimum power losses operation in islanded microgrids,” in *2017 IEEE International Conference on Environment and Electrical Engineering and 2017 IEEE Industrial and Commercial Power Systems Europe (EEEIC / I&CPS Europe)*, 2017, pp. 1–5.

APPENDIX A

A1: Results by conventional droop control method at 0.85 PF of Load 1.

	P0load (pu)		Q0load (pu)				
	L1(pu)	L2(pu)	L1(pu)	L2(pu)	PF-load1	PF-load2	Plosses
1	0.1000	0.1000	0.0620	0.0203	0.85	0.98	0.0057
2	0.1200	0.1000	0.0744	0.0203	0.85	0.98	0.007
3	0.1400	0.1000	0.0868	0.0203	0.85	0.98	0.0085
4	0.1600	0.1000	0.0992	0.0203	0.85	0.98	0.0102
5	0.1800	0.1000	0.1116	0.0203	0.85	0.98	0.0121
6	0.2000	0.1000	0.1239	0.0203	0.85	0.98	0.0143
7	0.2200	0.1000	0.1363	0.0203	0.85	0.98	0.0167
8	0.2400	0.1000	0.1487	0.0203	0.85	0.98	0.0193

	DG1			DG2		
	PG1/pu	QG1/pu	f1/pu	PG2/pu	QG2/pu	f2/pu
1	0.1238	0.0385	1.0035	0.0826	0.0442	1.0035
2	0.1364	0.0469	1.0018	0.091	0.0485	1.0018
3	0.1491	0.0554	1.0001	0.0994	0.0528	1.0001
4	0.1619	0.0639	0.9984	0.1079	0.0571	0.9984
5	0.1747	0.0724	0.9967	0.1165	0.0615	0.9967
6	0.1877	0.081	0.995	0.1251	0.0658	0.995
7	0.2007	0.0896	0.9932	0.1338	0.0702	0.9932
8	0.2139	0.0983	0.9915	0.1426	0.0746	0.9915

	LOAD BUS 3&4			
	PL1/pu	PL2/pu	QL1/pu	QL2/pu
1	0.1003	0.1003	0.0618	0.0202
2	0.1202	0.1002	0.0742	0.0203
3	0.14	0.1	0.0868	0.0203
4	0.1597	0.0998	0.0993	0.0203
5	0.1794	0.0997	0.1119	0.0204
6	0.199	0.0995	0.1246	0.0204
7	0.2185	0.0993	0.1373	0.0204
8	0.238	0.0991	0.15	0.0205

	V1/pu	V2/pu	V3/pu	V4/pu	I13	I24	I34
1	1.0229	1.0105	0.9949	0.9911	0.1268	0.0927	0.0311
2	1.0191	1.0077	0.9881	0.9863	0.1416	0.1023	0.0306
3	1.0154	1.0048	0.9812	0.9814	0.1566	0.112	0.0329
4	1.0116	1.0019	0.9743	0.9764	0.172	0.1219	0.0375
5	1.0078	0.999	0.9673	0.9714	0.1877	0.1318	0.0438
6	1.004	0.9961	0.9602	0.9664	0.2036	0.1419	0.0513
7	1.0002	0.9932	0.9531	0.9613	0.2198	0.1521	0.0595
8	0.9963	0.9902	0.9459	0.9561	0.2362	0.1625	0.0683

A2: Results by conventional droop control method at 0.9 PF of Load 1.

	P0load (pu)		Q0load (pu)				
	L1(pu)	L2(pu)	L1(pu)	L2(pu)	PF-load1	PF-load2	Plosses
1	0.1	0.1	0.048432	0.020306	0.9	0.98	0.0054
2	0.12	0.1	0.058119	0.020306	0.9	0.98	0.0065
3	0.14	0.1	0.067805	0.020306	0.9	0.98	0.0079
4	0.16	0.1	0.077492	0.020306	0.9	0.98	0.0094
5	0.18	0.1	0.087178	0.020306	0.9	0.98	0.0111
6	0.2	0.1	0.096864	0.020306	0.9	0.98	0.013
7	0.22	0.1	0.106551	0.020306	0.9	0.98	0.0151
8	0.24	0.1	0.116237	0.020306	0.9	0.98	0.0173

	DG1			DG2		
	PG1/pu	QG1/pu	f1/pu	PG2/pu	QG2/pu	f2/pu
1	0.1236	0.0304	1.0035	0.0824	0.0388	1.0035
2	0.1362	0.0371	1.0018	0.0908	0.042	1.0018
3	0.1487	0.0439	1.0002	0.0992	0.0452	1.0002
4	0.1614	0.0507	0.9985	0.1076	0.0484	0.9985
5	0.1741	0.0576	0.9968	0.1161	0.0517	0.9968
6	0.1869	0.0645	0.9951	0.1246	0.0549	0.9951
7	0.1998	0.0714	0.9934	0.1332	0.0582	0.9934
8	0.2127	0.0784	0.9916	0.1418	0.0615	0.9916

	LOAD BUS 3&4			
	PL1/pu	**PL2/pu**	**QL1/pu**	**QL2/pu**
1	0.1004	0.1004	0.0483	0.0202
2	0.1202	0.1002	0.058	0.0203
3	0.14	0.1	0.0678	0.0203
4	0.1598	0.0998	0.0776	0.0203
5	0.1794	0.0997	0.0875	0.0204
6	0.199	0.0995	0.0973	0.0204
7	0.2185	0.0993	0.1073	0.0204
8	0.238	0.0992	0.1172	0.0205

	V1/pu	**V2/pu**	**V3/pu**	**V4/pu**	**I13**	**I24**	**I34**
1	1.0265	1.0141	0.9989	0.995	0.124	0.0898	0.0271
2	1.0235	1.012	0.9929	0.9909	0.1379	0.0988	0.0246
3	1.0205	1.0099	0.9869	0.9868	0.152	0.1079	0.0251
4	1.0175	1.0077	0.9808	0.9826	0.1663	0.1171	0.0286
5	1.0144	1.0056	0.9747	0.9785	0.1808	0.1263	0.0341
6	1.0113	1.0034	0.9685	0.9742	0.1955	0.1357	0.041
7	1.0083	1.0012	0.9622	0.97	0.2104	0.1452	0.0487
8	1.0052	0.999	0.9559	0.9657	0.2255	0.1547	0.0569

A3: Results by conventional droop control method at 0.98 PF of Load 1.

	P0load (pu)		**Q0load (pu)**				
	L1(pu)	**L2(pu)**	**L1(pu)**	**L2(pu)**	**PF-load1**	**PF-load2**	**Plosses**
1	0.1	0.1	0.020306	0.020306	0.98	0.98	0.0049
2	0.12	0.1	0.024367	0.020306	0.98	0.98	0.0059
3	0.14	0.1	0.028428	0.020306	0.98	0.98	0.007
4	0.16	0.1	0.032489	0.020306	0.98	0.98	0.0082
5	0.18	0.1	0.036551	0.020306	0.98	0.98	0.0096
6	0.2	0.1	0.040612	0.020306	0.98	0.98	0.0111
7	0.22	0.1	0.044673	0.020306	0.98	0.98	0.0128
8	0.24	0.1	0.048734	0.020306	0.98	0.98	0.0146

	DG1			DG2		
	PG1/pu	**QG1/pu**	**f1/pu**	**PG2/pu**	**QG2/pu**	**f2/pu**
1	0.1234	0.0135	1.0036	0.0822	0.0276	1.0036
2	0.1358	0.0168	1.0019	0.0905	0.0285	1.0019
3	0.1482	0.0202	1.0002	0.0988	0.0295	1.0002
4	0.1607	0.0235	0.9986	0.1071	0.0304	0.9986
5	0.1732	0.0269	0.9969	0.1155	0.0314	0.9969
6	0.1858	0.0303	0.9952	0.1239	0.0324	0.9952
7	0.1984	0.0337	0.9935	0.1323	0.0334	0.9935
8	0.2111	0.0371	0.9919	0.1407	0.0344	0.9919

	LOAD BUS 3&4			
	PL1/pu	**PL2/pu**	**QL1/pu**	**QL2/pu**
1	0.1004	0.1004	0.0202	0.0202
2	0.1202	0.1002	0.0243	0.0203
3	0.14	0.1	0.0284	0.0203
4	0.1598	0.0999	0.0325	0.0203
5	0.1794	0.0997	0.0367	0.0204
6	0.199	0.0995	0.0408	0.0204
7	0.2186	0.0994	0.045	0.0204
8	0.238	0.0992	0.0491	0.0205

	V1/pu	**V2/pu**	**V3/pu**	**V4/pu**	**I13**	**I24**	**I34**
1	1.034	1.0216	1.0071	1.0029	0.12	0.0849	0.0209
2	1.0325	1.021	1.0028	1.0005	0.1325	0.093	0.0141
3	1.031	1.0204	0.9985	0.998	0.1451	0.1011	0.0096
4	1.0296	1.0197	0.9942	0.9955	0.1578	0.1092	0.0108
5	1.0281	1.0191	0.9898	0.993	0.1705	0.1174	0.0167
6	1.0265	1.0184	0.9855	0.9905	0.1834	0.1257	0.024
7	1.025	1.0178	0.9811	0.9879	0.1964	0.1341	0.0319
8	1.0235	1.0171	0.9766	0.9854	0.2094	0.1424	0.04

APPENDIX B

B1: Results by nonlinear droop control method at 0.85 PF of Load 1.

	P0load (pu)		Q0load (pu)				
	L1(pu)	L2(pu)	L1(pu)	L2(pu)	PF-load1	PF-load2	Plosses
1	0.100000	0.100000	0.061974	0.020306	0.85	0.98	0.0053
2	0.120000	0.100000	0.074369	0.020306	0.85	0.98	0.0066
3	0.140000	0.100000	0.086764	0.020306	0.85	0.98	0.0082
4	0.160000	0.100000	0.099159	0.020306	0.85	0.98	0.0099
5	0.180000	0.100000	0.111554	0.020306	0.85	0.98	0.0118
6	0.200000	0.100000	0.123949	0.020306	0.85	0.98	0.014
7	0.220000	0.100000	0.136344	0.020306	0.85	0.98	0.0164
8	0.240000	0.100000	0.148739	0.020306	0.85	0.98	0.0191

	DG1			DG2		
	PG1/pu	QG1/pu	f1/pu	PG2/pu	QG2/pu	f2/pu
1	0.1018	0.0502	0.9993	0.1034	0.0328	0.9993
2	0.1154	0.0581	0.9978	0.1108	0.0376	0.9978
3	0.1288	0.0662	0.9963	0.1185	0.0424	0.9963
4	0.1425	0.0742	0.9948	0.1261	0.0472	0.9948
5	0.1561	0.0823	0.9932	0.1338	0.052	0.9932
6	0.1703	0.0902	0.9918	0.1412	0.057	0.9918
7	0.1837	0.0987	0.9901	0.1496	0.0616	0.9901
8	0.1972	0.1072	0.9884	0.1579	0.0662	0.9884

	LOAD BUS 3&4			
	PL1/pu	PL2/pu	QL1/pu	QL2/pu
1	0.0999	0.0999	0.062	0.0203
2	0.1197	0.0998	0.0745	0.0203
3	0.1395	0.0996	0.0871	0.0204
4	0.1592	0.0995	0.0997	0.0204
5	0.1788	0.0993	0.1123	0.0204
6	0.1984	0.0992	0.125	0.0205
7	0.2178	0.099	0.1377	0.0205
8	0.2372	0.0988	0.1505	0.0205

	V1/pu	V2/pu	V3/pu	V4/pu	I13	I24	I34
1	1.0177	1.0181	0.9941	0.9946	0.1115	0.1066	0.0123
2	1.0142	1.0149	0.9873	0.9896	0.1274	0.1153	0.0189
3	1.0106	1.0118	0.9804	0.9845	0.1433	0.1244	0.0269
4	1.007	1.0085	0.9735	0.9794	0.1595	0.1335	0.0354
5	1.0034	1.0054	0.9666	0.9743	0.1759	0.1428	0.0442
6	0.9999	1.002	0.9596	0.9691	0.1928	0.152	0.0531
7	0.9961	0.9989	0.9524	0.9639	0.2094	0.1619	0.0625
8	0.9923	0.9958	0.9452	0.9587	0.2262	0.172	0.0721

B2: Results by nonlinear droop control method at 0.9 PF of Load 1.

	P0load (pu)		Q0load (pu)				
	L1(pu)	L2(pu)	L1(pu)	L2(pu)	PF-load1	PF-load2	Plosses
1	0.1000000	0.1000000	0.0484322	0.0203059	0.9	0.98	0.005
2	0.1200000	0.1000000	0.0581187	0.0203059	0.9	0.98	0.0062
3	0.1400000	0.1000000	0.0678051	0.0203059	0.9	0.98	0.0076
4	0.1600000	0.1000000	0.0774915	0.0203059	0.9	0.98	0.0091
5	0.1800000	0.1000000	0.0871780	0.0203059	0.9	0.98	0.0108
6	0.2000000	0.1000000	0.0968644	0.0203059	0.9	0.98	0.0127
7	0.2200000	0.1000000	0.1065509	0.0203059	0.9	0.98	0.0148
8	0.2400000	0.1000000	0.1162373	0.0203059	0.9	0.98	0.0172

	DG1			DG2		
	PG1/pu	QG1/pu	f1/pu	PG2/pu	QG2/pu	f2/pu
1	0.102	0.0418	0.9994	0.1029	0.0276	0.9994
2	0.1155	0.048	0.998	0.1102	0.0314	0.998
3	0.129	0.0543	0.9965	0.1177	0.0351	0.9965
4	0.1427	0.0606	0.995	0.1251	0.0389	0.995
5	0.1561	0.0671	0.9934	0.1329	0.0425	0.9934
6	0.1699	0.0734	0.9919	0.1405	0.0463	0.9919
7	0.1835	0.08	0.9903	0.1483	0.05	0.9903
8	0.1974	0.0864	0.9888	0.1559	0.0539	0.9888

	LOAD BUS 3&4			
	PL1/pu	PL2/pu	QL1/pu	QL2/pu
1	0.0999	0.0999	0.0485	0.0203
2	0.1198	0.0998	0.0582	0.0203
3	0.1395	0.0996	0.068	0.0204
4	0.1592	0.0995	0.0779	0.0204
5	0.1788	0.0993	0.0878	0.0204
6	0.1984	0.0992	0.0976	0.0205
7	0.2179	0.099	0.1076	0.0205
8	0.2373	0.0989	0.1175	0.0205

	V1/pu	V2/pu	V3/pu	V4/pu	I13	I24	I34
1	1.0214	1.0216	0.9981	0.9984	0.1079	0.1043	0.007
2	1.0187	1.0191	0.9921	0.9941	0.1228	0.1125	0.0132
3	1.0159	1.0166	0.9861	0.9899	0.1378	0.1209	0.0208
4	1.0131	1.0141	0.9801	0.9856	0.153	0.1292	0.0288
5	1.0102	1.0116	0.974	0.9813	0.1682	0.1379	0.0371
6	1.0074	1.0091	0.9678	0.9769	0.1837	0.1466	0.0454
7	1.0045	1.0066	0.9616	0.9725	0.1993	0.1554	0.054
8	1.0016	1.0041	0.9554	0.9681	0.2152	0.1643	0.0625

B3: Results by nonlinear droop control method at 0.98 PF of Load 1.

	P0load (pu)		Q0load (pu)				
	L1(pu)	L2(pu)	L1(pu)	L2(pu)	PF-load1	PF-load2	Plosses
1	0.100000	0.100000	0.020306	0.020306	0.98	0.98	0.0046
2	0.120000	0.100000	0.024367	0.020306	0.98	0.98	0.0056
3	0.140000	0.100000	0.028428	0.020306	0.98	0.98	0.0067
4	0.160000	0.100000	0.032489	0.020306	0.98	0.98	0.008
5	0.180000	0.100000	0.036551	0.020306	0.98	0.98	0.0094
6	0.200000	0.100000	0.040612	0.020306	0.98	0.98	0.0109
7	0.220000	0.100000	0.044673	0.020306	0.98	0.98	0.0126
8	0.240000	0.100000	0.048734	0.020306	0.98	0.98	0.0145

	DG1			DG2		
	PG1/pu	QG1/pu	f1/pu	PG2/pu	QG2/pu	f2/pu
1	0.102	0.0246	0.9995	0.1025	0.0166	0.9995
2	0.1157	0.0272	0.9981	0.1094	0.0183	0.9981
3	0.1296	0.0298	0.9967	0.1163	0.02	0.9967
4	0.1431	0.0325	0.9953	0.1236	0.0215	0.9953
5	0.1566	0.0354	0.9938	0.1311	0.023	0.9938
6	0.17	0.0384	0.9923	0.1387	0.0244	0.9923
7	0.184	0.041	0.9909	0.1457	0.0262	0.9909
8	0.1966	0.0445	0.9892	0.1542	0.0271	0.9892

	LOAD BUS 3&4			
	PL1/pu	PL2/pu	QL1/pu	QL2/pu
1	0.0999	0.0999	0.0203	0.0203
2	0.1198	0.0998	0.0244	0.0203
3	0.1395	0.0997	0.0285	0.0204
4	0.1592	0.0995	0.0326	0.0204
5	0.1789	0.0994	0.0368	0.0204
6	0.1985	0.0992	0.0409	0.0205
7	0.218	0.0991	0.0451	0.0205
8	0.2374	0.0989	0.0493	0.0205

	V1/pu	V2/pu	V3/pu	V4/pu	I13	I24	I34
1	1.0291	1.0289	1.0064	1.0063	0.1019	0.1009	0.004
2	1.0279	1.0278	1.0021	1.0036	0.1156	0.108	0.0074
3	1.0268	1.0267	0.9979	1.0009	0.1295	0.115	0.0137
4	1.0255	1.0256	0.9936	0.9983	0.1431	0.1224	0.0208
5	1.0243	1.0247	0.9893	0.9956	0.1567	0.1299	0.0282
6	1.0229	1.0237	0.9849	0.9929	0.1703	0.1375	0.0356
7	1.0218	1.0226	0.9806	0.9901	0.1845	0.1448	0.0427
8	1.0202	1.0219	0.9761	0.9876	0.1975	0.1532	0.0511